

Electrochemical model of solid oxide fuel cell for simulation at the stack scale. Part I: Calibration procedure on experimental data

Arata Nakajo^{*1}, Zacharie Wullemin¹, Patrick Metzger², Stefan Diethelm¹, Günter Schiller³, Jan Van herle¹, and Daniel Favrat¹

¹Laboratoire d'Energétique Industrielle (LENI), Institut de Génie Mécanique, Ecole Polytechnique Fédérale de Lausanne, 1015 Lausanne, Switzerland

²Würth Solar PV power plants division, D-74523, Schwäbisch-Hall, Germany

³German Aerospace Center (DLR), Institute of Technical Thermodynamics, D-70569, Stuttgart, Germany

*corresponding author: arata.nakajo@epfl.ch, tel: +41 21 693 35 05

Abstract

The simulation of the behaviour of a solid oxide fuel cell (SOFC) device requires a reliable electrochemical model that supports the implementation of degradation phenomena for lifetime predictions.

This study comprises two parts. This Part I describes the calibration of an electrochemical model based on physical principles for simulation at the stack scale. Part II presents the further implementation of degradation models. A distinction is made between the two most common cathode materials, lanthanum strontium manganite and lanthanum strontium cobalt ferrite. The experimental data used for the parameter estimations was gathered by two segmented setups.

The calibrations enabled to reproduce adequately the measurements over a wide range of operating conditions. The optimal values of the physical parameters were inside the ranges reported in literature. Unambiguous discrimination between variations (i) in the choice of rate-determining steps, (ii) data on the properties of the materials found in literature and (iii) empirical relations for the steam-methane reforming reaction could not be achieved. However, these model variations do not affect significantly the predicted magnitudes and distributions of the field variables assumed to govern the degradation processes at the SRU scale, compared with the uncertainties on the degradation phenomena to be implemented in Part II.

Keywords: Solid Oxide Fuel Cell, Electrochemical model, Parameter estimation, Segmented setup

1 Introduction

The core of any solid oxide fuel cell (SOFC) device is the membrane electrode assembly (MEA). Most of the modelling effort is focused on the description and understanding of the electrochemical processes taking place in the MEA. The level of accuracy and refinement depends on the issue to be solved. The affordable computing time on the modelling of the MEA is for instance not identical for the optimisation [1, 2] or simulations of the dynamic behaviour [3–5] of a whole SOFC system, calculation of the temperature profile in the single repeating units (SRU) to mitigate structural failures [6–8] or identification of the relation between electrode performance and microstructure [9, 10]. Therefore, different phenomena, such as heat transfer or fluid dynamics, can be selectively neglected, depending on the emphasis in the study. However, all modelling studies on SOFC devices commonly contain an electrochemical model of suitable complexity.

The variations in scales and aims obviously have an impact on the choice of a modelling approach. It can range from neural networks, e.g. [11], to the discrete element method (DEM) [10]. Neural networks combine a very fast estimation of the cell behaviour to an efficient calibration on experimental data, but do not necessarily enforce physically-consistent predictions. In contrast, DEM is devoted to the electrode scale, due to computation time reasons and implementation complexity.

A major drawback of SOFC devices is the degradation rate of their performance, even during steady-state operation, which is currently above the specifications for large-scale commercialisation. Identifying the causes of degradation is a subject of extensive ongoing research, which has already shed light on some phenomena, related to alterations of the materials and interfaces. Coarsening of the electrode microstructure results in a reduction of the effective triple-phase boundary length (TPBL), where the electrochemical processes take place [12–15]. Formation of insulating phases, such as lanthanum (LZO) or strontium zirconates (SZO) in cathodes based on lanthanum strontium manganites (LSM) [16–18] have been observed. They hinder, or in the best case alter the electrochemical processes. Similarly, impurities in the raw materials used for the manufacturing of anodes made of nickel and yttria-stabilised zirconia (Ni-YSZ) are believed to promote the formation of glassy phases at the interfaces between the constituents [19]. Phase transformation is one possible explanation for the well-known decrease in ionic conductivity of YSZ during aging [20, 21]. This affects not only the widespread YSZ electrolyte, but also the electrodes, i.e. in composite structures, such as LSM-YSZ or Ni-YSZ, the number of electrochemically active sites, hence electrode performance, is drastically increased. The so-called contamination of the electrodes is not necessarily observed in button-cell tests in alumina test rigs, but can dominate in SOFC systems, where different materials and fuels are used for cost and engineering reasons. The deposition of chromium on the active sites in the cathode from volatile

chromium species, evaporated from the metallic components of the stack or system is a well-known cause of degradation [22–27].

A mitigation strategy of the degradation involves different research fields. It starts with the selection of materials, in light of their absolute performance but also long-term stability. High electrochemical activity and stability are usually contradictory aims. The numerous long-term experiments on button-cells and short stacks highlight a very strong dependence of the degradation rate on the operating conditions. Indeed, all the aforementioned phenomena depend on temperature, local overpotential and gas composition, among others, which are unevenly distributed in a SOFC stack. This results in different but interrelated local degradation rates [28–30]. A proper control strategy [3,31] and stack and system design [32] are therefore vital to extend the lifetime of SOFC devices.

The accuracy of the electrochemical model plays a central role in providing guidance in control strategy and SRU design for the mitigation of the degradation, as it constitutes the core of all SRU/stack models, which basically consist in an electrochemical model coupled to field equations for mass and heat transfer. Electrochemical models for the simulation of the behaviour of SOFC SRUs and stacks have made for a long time a wide use of semi-empirical models [33–39]. While their ability to match experimental current-voltage (IV) characteristics within the typical range of operating conditions of SOFC stacks is well established, this class of model intrinsically fails when it comes to the calculation of local quantities within the electrodes or consistent handling of multi-component gas mixtures. Typical examples are respectively local overpotential or operation with partially reformed methane. This classical approach, despite its advantage in terms of ease of implementation and computation time, is therefore not suited for degradation-oriented investigations. In contrast, the research on the elementary processes of the oxygen reduction reaction (ORR) or hydrogen oxidation (HO) have resulted in detailed modelling at the micro-scale [40–44]. Such approaches have then been used in designing electrodes and current collection [9, 45] with the support of percolation theories to provide the correct effective conductivities and TPBL in the composite structure [46,47]. The current trend consists in using DEM to handle changes in composition or microstructure at the particle size, or in using a combination of imaging techniques to record the actual geometry of an electrode or interface, and modelling techniques such as the lattice Boltzmann method [48, 49]. Despite the availability of an analytical solution in some cases [40,50], the link between micro- and SRU/stack modelling in general has remained loose for a long time.

A recent change coincides with the introduction of elementary heterogeneous chemical kinetics in the SOFC field [51–56]. At the same time, standards in levels of detail have been set for a satisfactory description

of some phenomena. In the case of anode-supported SOFCs, the need of the dusty-gas model (DGM) has been recognised for the modelling of diffusion processes in the anode [57,58]. The studies with this framework usually consider a representative channel along the flow path [59–61]. The variations at the SRU scale of the quantities along the axis perpendicular to the gas flow are neglected. This kind of model is not compatible with neither the cross-flow configuration nor structural analysis which needs the whole temperature profile. Advanced modelling frameworks are still seldomly found in design-oriented SRU models [62, 63].

Even the most refined modelling approaches embed fitting parameters with however a physical meaning to reproduce not only qualitatively but also quantitatively the response of a SOFC. The first requirement for an electrochemical model for SRU/stack simulations is the reliable prediction of the performance of the cells, within a large range of operating conditions. This partially ensures a correct calculation of the local physical quantities at the SRU scale. Parameter estimation and design of experiment (DOE) tools [64,65] are of great value for the calibration of such models, as a direct measurement of each parameter is unthinkable and even the most comprehensive model cannot fully reflect reality. Such procedures as well as dynamic simulations require fairly fast models. Therefore, a second constraint is placed on computation time. Finally, empirical electrochemical models are discarded, as the most important capability of the electrochemical model in the present context is its compatibility with a consistent integration of degradation phenomena.

Once the electrochemical model is calibrated, thermo-electrochemical and structural SRU models can allow a quick, reliable and inexpensive evaluation of different technological solutions, such as the type of cell, particularly electrode, or the sealing or gas diffusion layer (GDL) system, in regard of the target application. Next, the risks of failure ensued from typical situations a SOFC stack may face during service, can be evaluated, and the procedures adjusted. Finally, the insertion of degradation phenomena in the electrochemical model allows preliminary predictions of the lifetime, and hence the needed safety margin for a given specification.

A major difficulty in the setting of such tools is to efficiently gather experimental data. Automated segmented-cell setups [66] have several benefits for this task. One can take advantage of their ability to provide insights into local quantities for different but linked purposes [67, 68]. Investigations can focus either on the dependence of the cell behaviour on the operating conditions or on the spatial distribution and interaction of the phenomena. A large amount of information can be effectively gathered by a few experimental runs, as the composition of the gases and the temperature vary along the flow path, depending on the rate of the chemical and electrochemical reactions. This ability helps to mitigate imprecision due to degradation, when a large amount of experiments have to be performed one after the other. DOE tools can

optimise the arrangement of the segments and operating conditions to detect or alternatively avoid large spatial gradients.

The context of the present study is the prediction of ends-of-service induced either by an exceedingly severe degradation of the stack performance after long-term operation, or by discrete structural failures, due to the combined effects of aging and operating procedures. This is a first step towards reliable guidance in the design and operation of SOFC stacks, against degradation. The study focuses on intermediate temperature (IT), anode-supported SOFC, but the modelling approach and validation procedure are more general. The electrochemical and degradation models for simulations at the SRU/stack scale developed here are presented in two parts. Part I focuses on the calibration of a one-dimensional electrochemical model. The implementation and study of degradation phenomena is described in Part II [69], together with a more detailed model of the cell and interconnection, to identify the limitations of the one-dimensional approach. First, a short literature survey is presented on the current state of knowledge and capabilities of existing models to provide guidance in the choice of modelling approaches. Variations among the selected ones are then discussed in light of accuracy in the prediction of the cell performance and further implementation of physical modelling of selected degradation phenomena. Next, the electrochemical model is calibrated on data gathered by two segmented-cell setups [66, 67, 70]. Finally, the model is implemented in a one-dimensional SRU model to track possible physical inconsistencies and to assess the influence of the choice of modelling assumptions on the calculation of the field variables assumed to drive the degradation.

2 Modelling approach

2.1 Field equations

The main zones in a SRU, e.g. manifold and electrochemically-active area, are spatially discretised along the gas-flow direction, and they include the local one-dimensional electrochemical model. The modular units, implemented in gPROMS [65], an equation-oriented process modelling tool, can be assembled in both gas flow and stacking directions, the former being sufficient to analyse experimental data from a segmented SRU. The one-dimensional nature of the models enables fast calculations but restricts their application to either co- or counter-flow configurations, with a fairly uniform gas distribution. The generic shape of a modular element is depicted in Figure 1a. Possible connection boundaries are Γ_1/Γ_8 and $\partial\mathcal{R}_1$. The species on the fuel side are restricted to H_2 , H_2O , CO , CO_2 , CH_4 and N_2 .

[Figure 1 about here.]

[Figure 2 about here.]

The model is not fully dynamic in terms of species transport and heat transfer, since only thermal inertia of the solid components and gases are accounted for. The energy conservation of the cell and of both top and bottom MICs are calculated as follows and all terms detailed further below in Eq.3 to Eq.10 :

$$\lambda_s \frac{\partial^2 T_s}{\partial y^2} + \dot{Q}_{s_{cond}} + \dot{Q}_{s_{conv}} + \dot{Q}_{s_{htl}} + \dot{Q}_{s_{bc}} = \rho_s c_{h_s} \frac{\partial T_s}{\partial t} \quad \text{in } \mathcal{R}_1, \mathcal{R}_7 \quad (1)$$

$$\lambda_s \frac{\partial^2 T_s}{\partial y^2} + \dot{Q}_{s_{rx}} + \dot{Q}_{s_{cond}} + \dot{Q}_{s_{conv}} = \rho_s c_{h_s} \frac{\partial T_s}{\partial t} \quad \text{in } \mathcal{R}_{3-5} \quad (2)$$

The cell layers are discretised in the electrochemical model, see also Section 2.2, but merged in \mathcal{R}_{3-5} in the field equations. Similarly, the thermal inertia of the GDLs and sealants are embedded in the MICs, but their in-plane thermal conductivities are neglected. $\dot{Q}_{s_{rx}}$ is used to relocate in the cell the rate of volumetric thermal energy generated by the chemical and electrochemical reactions. The energy released by the chemical reactions is computed from the balance of species at the anode-gas interface, assuming that all methane and carbon monoxide fluxes towards the anode are globally consumed by the steam-methane reforming (SMR) and the water-gas shift (WS) reactions:

$$\begin{aligned} \dot{Q}_{3-5_{rx}} = & \frac{N_{CH_4}|_{\text{GDL-an}}}{h_{3-5}} (-dH_{o_{\text{SMR}}} - dH_{o_{\text{WS}}}) + \frac{N_{CO}|_{\text{GDL-an}}}{h_{3-5}} (-dH_{o_{\text{WS}}}) \\ & + \frac{j_{tot}}{2F h_3} (-dH_{o_{\text{elchem}}}) - \frac{V \cdot j_u}{h_{3-5}} \end{aligned} \quad (3)$$

$\dot{Q}_{s_{cond}}$ refers to the rate of volumetric energy due to heat transfer between the cell and the MICs by conduction through the GDLs:

$$\dot{Q}_{s_{cond}} = \frac{\lambda_g}{h_s h_{3-5}} (T_{3-5} - T_s) \quad \text{in } \mathcal{R}_1, \mathcal{R}_7 \quad (4)$$

$$\dot{Q}_{s_{cond}} = \frac{\lambda_2}{h_2 h_s} (T_1 - T_s) + \frac{\lambda_6}{h_6 h_s} (T_7 - T_s) \quad \text{in } \mathcal{R}_{3-5} \quad (5)$$

Convection heat transfer between the gases and the solid structure is embedded in $\dot{Q}_{s_{conv}}$. Common relations are used for the computation of heat transfer coefficients [71].

$$\dot{Q}_{s_{conv}} = \frac{h_g^c}{h_s} (T_g - T_s) \quad \text{in } \mathcal{R}_1, \mathcal{R}_7 \quad (6)$$

$$\dot{Q}_{s_{conv}} = \sum_g \frac{h_g^c}{h_s} (T_g - T_s) \quad \text{in } \mathcal{R}_{3-5} \quad (7)$$

$\dot{Q}_{s_{htl}}$ and $\dot{Q}_{s_{bc}}$ refer to boundaries $\partial\mathcal{R}_2$ and, Γ_1 and Γ_8 (see Figure 1). $\dot{Q}_{s_{htl}}$ corresponds to the rate of volumetric energy due to averaged radiation exchanges between the sides of the SRU and its surroundings. Heat exchange by radiation between the SRU and its surrounding is modelled in a simplified manner, i.e. each node is coupled to an equivalent front node of the insulation. The exchange with above and underneath, and front and rear nodes is neglected [72].

$$\dot{Q}_{s_{htl}} = \frac{C_{s_{htl}}}{L_x} \varepsilon_{\zeta} (T_{s_{avg}}^4 - T_{isl}^4) \text{ in } \mathcal{R}_1, \mathcal{R}_7 \quad (8)$$

$C_{s_{htl}}$ is a geometrical correction factor for the GDL and sealant heights. $\dot{Q}_{s_{bc}}$ varies depending on the assembly of the modules. It includes thermal exchanges by either radiation with the surroundings or thermal conduction with above and underneath SRUs. The former case refers to top/bottom SRUs in a stack or a separately-tested SRU, while the latter is applied to SRUs in a stack.

$$\dot{Q}_{s_{bc}} = \frac{C_{bc}}{L_x} \varepsilon_{\zeta} (T_s^4 - T_{isl}^4) \text{ in } \mathcal{R}_1, \mathcal{R}_7, \text{ isolated SRU} \quad (9)$$

$$\dot{Q}_{s_{bc}} = \frac{2}{h_s^2} \lambda_s (T_{s_{bc}} - T_s) \text{ in } \mathcal{R}_1, \mathcal{R}_7, \text{ stacked SRU} \quad (10)$$

C_{bc} is a geometrical correction factor corresponding to additional heat losses over sealing or manifold areas not explicitly considered due to the 1D assumption. Adiabatic conditions for a SRU in a stack yield $\dot{Q}_{s_{bc}} = 0$. The energy conservation on the insulation yields:

$$\varepsilon_{\zeta} (T_{s_{avg}}^4 - T_{isl}^4) = \frac{\lambda_{isl}}{h_{isl}} (T_{isl} - T_{amb}) \quad (11)$$

$T_{isl} = T_{fnce}$ is enforced, depending on the conditions of the experiment.

The conservation of energy of gases as well as the conservation of species considers variations of gas densities, which are sometimes neglected in the literature [35] but of relevance in the case of internal steam-methane reforming. The ideal gas assumption is used and the required properties are computed from Todd et al. [73].

$$\frac{\partial(\rho_g u_g H_g)}{\partial y} + \dot{Q}_{g_{conv}} + \dot{Q}_{g_{rx}} = \rho_g c_{h_g} \frac{\partial T_g}{\partial t} \text{ in } \mathcal{R}_2, \mathcal{R}_6 \quad (12)$$

$$\frac{\partial(\rho_g u_g \omega_i)}{\partial y} = \frac{M_i N_i|_{\text{GDL-an}}}{h_g} \text{ in } \mathcal{R}_2, \mathcal{R}_6 \quad (13)$$

$$\frac{\partial(\rho_g u_g)}{\partial y} = \sum \mathfrak{R}_i^m \text{ in } \mathcal{R}_2, \mathcal{R}_6 \quad (14)$$

$\dot{Q}_{g_{rx}}$ are to re-insert the rate of heat generated by the electrochemical and chemical reactions at the proper place, and are computed in a similar manner to $\dot{Q}_{s_{rx}}$.

2.2 Electrochemical model

The one-dimensional electrochemical model considers both ohmic and non-ohmic losses. The calculation of the losses in the electrolyte, the anode and the cathode terms is described in Sections 2.2.1-2.2.3. Part II [69] presents the modelling approach and parameters for the ohmic losses in the MICs. A small electronic conductivity of the electrolyte, which induces a slight leakage current is included in the electrolyte [2]. Ohmic losses due to current constrictions in the GDLs are evaluated using analytical relations [74].

The electrochemical model is based on the equivalent circuit approach, which is depicted in Figure 3. The calculation of the Nernst potential from interfacial gas compositions, is based on hydrogen only, as equilibrium of the water-gas-shift reaction is approximated in the anode support. The equivalent circuit simplification, which is sometimes criticised, is tested against a more detailed model based on the complete computation of the potential in the ionic- and electronic-conducting networks in Part II [69].

[Figure 3 about here.]

2.2.1 Electrolyte and compatibility layer

The most common electrolyte material used in anode-supported SOFC is YSZ. The maximum ionic conductivity corresponds to the minimum amount of dopant needed to stabilise the cubic fluorite phase, which is obtained in 8 mol% YSZ. Further dopant addition causes an overall reduction of the defect mobility, hence ionic conductivity [75]. Another central material in anode supported SOFC is gadolinia-doped ceria (GDC). Despite its higher ionic conductivity than 8YSZ, its major drawback is a non-negligible electronic conduction at low oxygen partial pressure as well as isothermal expansion, which results in large stresses when subjected to gradients in oxygen partial pressure [76]. This prevents its use as sole electrolyte material in IT-SOFC. It can however serve as a compatibility layer, to prevent undesirable reactions between the YSZ electrolyte and a lanthanum strontium cobaltite ferrite (LSCF) cathode [77].

Ohmic losses in the electrolyte are computed in the present study using simple relations, without differentiation of the contributions of the grain boundaries and the bulk. Thin electrolytes used in anode-supported cells have a higher resistance than thick ones relative to their thickness. The difference is significant for the typical electrolyte thickness in anode-supported cell, ranging from 4 to 10 μm . Fleig et al. [78] have attributed this increase in resistance to current constriction, due to the uneven interface between the dense electrolyte

and the porous electrodes. Their interpolated relation satisfactorily reproduces their finite-element calculations and is used in the present work. It should however be stressed that in reality, constriction effects depend on reaction pathways and the extension of the active zone, hence on the type of cathode and anode. Charge transfer at the interface between the YSZ electrolyte and GDC compatibility layer is neglected.

$$\text{ASR}_{ion_{elect}} = \frac{h_{elect} - h_{cl}}{\sigma_{ion_{elect}}^e} + \frac{l_g}{\sigma_{ion_{elect}}^e} \left(\frac{l_g/d_g - 1}{d_g/l_g + 1} \right) + \frac{1 - n_{cl}}{1 + 0.5n_{cl}} \frac{h_{cl}}{\sigma_{ion_{cl}}^e}, \text{ in } \mathcal{R}_4 \quad (15)$$

In the absence of a compatibility layer, h_{cl} is set equal to zero. The ionic conductivity of 8YSZ, GDC or YDC strongly depends on temperature, according to:

$$\sigma_{ion}^e = \frac{k_{o_{ion}}}{T_s} \exp \left[-\frac{E_{a_{ion}}}{R} \left(\frac{1}{T_s} \right) \right] \quad (16)$$

This relation is used as well for the electronic and ionic conductivity of other SOFC and SRU materials.

2.2.2 Anode

Many investigations have been devoted to identify the underlying mechanisms of the hydrogen oxidation in SOFC Ni-YSZ anodes. These are based on the observation of the response during either DC polarisation, galvanostatic current interruption (GCI) or electrochemical impedance spectroscopy (EIS). Experimental studies have first inferred possible rate determining steps (RDS) from the visible influences on the polarisation resistance of variations of hydrogen and steam partial pressure, temperature, overpotential and even electrode microstructure. Possible initial RDS candidates include, among others, dissociative adsorption of hydrogen, formation of hydroxyl, desorption of water, surface diffusion of species or charge transfer reaction by different spillover mechanisms. Either bulk or surface pathways can, to some extent, contribute concurrently and competitively.

A porous Ni-YSZ cermet has a complex structure, which does not allow to draw unambiguous relations for instance between polarisation resistance and TPBL, as a precise measure of the latter in a real anode is difficult to access. Yet, TPBL is a key parameter for electrode development, which can be modified fairly easily, by varying the particle size distribution and the sintering procedure. Therefore, more fundamental studies have been performed on pattern anodes, among others, as the features of their geometry are comparatively well defined and can be varied in a controlled manner. The most referenced studies [79–81] share some trends, which highlight a linear dependence of the polarisation resistance on the TPBL, a weak dependence on the hydrogen partial pressure and a so-called catalytic effect of steam. The range of investigated

operating conditions is wide enough to cover that of intermediate temperature SOFCs. Reported Tafel slopes range from 1 [80,82] to 3/2 [81], and the number of arcs in the analysis of EIS measurements from 1 [80] to 3 [83], leading to discrepancies in the interpretation of the results. The process responsible for the main arc is either an adsorption or a diffusion process on Ni [80] or charge-transfer [81]. Bieberle et al. [79] have discarded diffusion and adsorption/desorption of water, but considered charge-transfer, removal of O^{2-} and adsorption of hydrogen as possible candidates. These authors have proposed a mechanism to account for the catalytic effect of water, where the active region is enlarged due to a hydroxylated YSZ surface.

Research on porous Ni-YSZ anodes has been carried out as well. The extension of the active zone in the composite structure is of interest for electrode optimisation. Brown et al. [84] have deduced an extension of approximately 10 μm at 1273 K. Another study [85] has qualitatively captured a similar trend, by varying the ionic conductivity of the electrolyte phase in the composite anode. At the particle scale, Brown et al. [84] suggest that effective active sites might overlap in the composite electrode, in which case conclusions drawn from experiments on pattern anodes do not necessarily hold for technological ones. Anyway, rate-limiting electrochemical processes produce one arc in general, two in several cases, the others being attributed to gas conversion or diffusion in the stagnant gas layer over the electrode [84,86]. Jiang et al. [87] have proposed readily usable relations for SRU performance simulations from GCI measurements on Ni-3YSZ anodes. Their further comparison between dependences on hydrogen and steam partial pressure on the one hand, and activation energy obtained from EIS or GCI on the other hand, stresses the care required when inferring values of parameters, even for performance modelling [88]. Holtappels et al. [89,90] have tested Ni-8YSZ anodes over a wide temperature range (998-1223 K), which has highlighted a transition around 1118 K and a somewhat lower apparent anodic charge-transfer coefficient of 0.7. These authors suggest that hydrogen oxidation is controlled by charge-transfer at low temperature, while adsorption together with chemical reaction between adsorbed species seems to contribute noticeably at high temperature. In general, reported apparent reaction order on hydrogen and steam, and activation energy range from -0.5 to 1.0, 0.3 to 1.0 and 70 to 170 kJmol^{-1} , respectively. Some researchers therefore suggest a dominant role of impurities to account for the strong influence of the anode response on the raw material and manufacturing route, which is supported by the detection of glassy phases at Ni/YSZ interfaces [19,91].

The aforementioned discrepancies highlight the need for refined modelling to assist the interpretation of experimental data. Comparatively limited efforts have been devoted to this task. Most of the comprehensive investigations using an elementary kinetic approach have focused on pattern anodes. Bieberle et al. [92] have applied state-space modelling (SSM) to the analysis of their experimental data [79]. Their study is

rather an illustration of the capability of SSM than an evaluation of different likely mechanisms, but the need for a large number of accurate parameters and complex dependences between the different assumed elementary steps, one being able to mimic the effect of another, has been demonstrated. The approach of Zhu et al. [93] is compatible with modelling at the SRU scale. The simplified elementary kinetic scheme, with a limited number of steps and a single RDS, yields an expression in Butler-Volmer form, with apparent reaction orders and charge-transfer coefficients. The RDS favoured by these authors is charge-transfer by hydrogen spillover to hydroxyl site on YSZ, which yields compatible apparent charge transfer coefficients with the data from De Boer et al. [81]. This formalism is not new in the SOFC field and has been presented earlier for the cathode [45,94], as discussed in Section 2.2.3. Bessler et al. [52] have pointed out the effect of equilibrium potential on the so-called catalytic effect of steam on the electrochemical oxidation of hydrogen and some limitations of the analytical approach of Zhu et al. [93], in particular at high fuel utilisation. In addition, comparisons of trends produced by different single limiting charge transfer mechanisms against experimental data generally suggest hydrogen spillover is the RDS. The same group of authors [82] has recently published one of the most advanced studies to date, where the best overall fit has been obtained by a combination of hydrogen spillover from Ni surface to oxygen ions and hydroxyl ions on YSZ, while the one-dimensional spatial discretisation has shown large surface coverage gradients on YSZ, over a large distance of $0.1 \mu\text{m}$, compared with the particle size in technological composite anodes. The RDS was detected through a sensitivity analysis, which has revealed among all considered elementary steps four possible co-limiting RDS: (i) hydrogen spillover to YSZ, (ii) water association on YSZ, (iii) water dissociation on YSZ and, (iv) surface diffusion of hydroxyl ions adsorbed on YSZ. The sensitivity analysis has also stressed the need for reliable thermodynamic data.

Modelling of electrochemical processes. A modelling approach for the chemical and electrochemical processes in the anode must be selected in view of the purpose of the present electrochemical model and the aforementioned survey. The physics behind hydrogen oxidation is complex. Yet, at the SRU/stack scale, the use of hydrogen causes lower efficiencies than fully or partially pre-reformed methane, for instance. In the latter case, the possibility of electrochemical conversion of carbon monoxide further complicates the situation. Furthermore, adsorbed species on Ni can be involved in either reforming reactions or hydrogen oxidation, which therefore occur concurrently and competitively. The elementary kinetic approach formally enables a consistent handling of the situation, at the cost of difficult model implementation, large yet reliable database, and ideally the need of a discretisation of the TPB. Yet, possibly dominant effects of impurities

would be neglected. To our knowledge, full coupling has not yet been performed in a SOFC model. SRU models for dynamic simulation can currently not afford this level of detail. A common older approach used here that is acknowledged of reasonable accuracy in performance modelling consists in first neglecting the contribution of carbon monoxide oxidation, and second in completely uncoupling the reforming and hydrogen oxidation reactions.

In the present context, the main rationale behind an increased level of complexity in the description of the electrochemical processes is the implementation of degradation phenomena. The knowledge acquired from investigation at the TPB or electrode scale has to be considered in a simplified manner at the SRU scale. The current knowledge on the oxidation of hydrogen is not extensive enough to provide a solid background for the handling of degradation in the view of altered sequences of elementary mechanisms and RDS. The dependence of the polarisation resistance on the TPBL is clear. The latter is affected by the coarsening of the nickel particles in the anode [15,95]. The limitations induced by the restriction of the electrochemical processes to the anode/electrolyte interface, which is a necessary simplification for simulation at the SRU scale, are discussed in Part II [69]. The choice of this significant simplification is due to the evolution patterns of the selected degradation phenomena which are MIC corrosion, decrease of the ionic conductivity of YSZ, nickel particle coarsening, chromium contamination and formation of insulating phases in LSM-YSZ cathodes. Either decreases of ionic conduction of the electrolyte phase or coarsening of the nickel particles reach a plateau, after an initial variation [95–98]. In the case of nickel particle coarsening, this is due to the structural constraint enforced by the YSZ backbone. These phenomena are not expected to provoke alone the end of life of a SOFC stack; a quantitative prediction enables to set a safety margin to fulfil requirements over long periods and to identify alterations of the temperature distribution and ensuing thermo-mechanical stresses. On the contrary, chromium contamination or development of insulating phases on the cathode side can fully block the active sites. Therefore, computing time is spared to afford a composite model for the cathode, rather than for the anode (see Section 2.2.3). This approach obviously depends on the selection of the degradation phenomena. The implementation of sulfur poisoning or carbon deposition, for instance, would require to place the emphasis on other physical processes.

Notwithstanding the difficulty in fixing a strong physical basis, a correct dependence of the electrochemical model on the local conditions in the SRU is paramount for structural analysis based on the temperature profile. The easiest but coarsest approach consists in implementing, without any assumption on the mechanisms or RDS, apparent reaction orders and charge-transfer coefficients from the literature. As discussed previously, the discrepancy in reported values is large and the temperature range considered in the available

studies does not necessarily match that of interest for a particular application. Therefore, these can be even included in the set of estimated parameters, during the calibration procedure. The generic expression, which embeds all electrochemical processes at the anode/electrolyte interface, is:

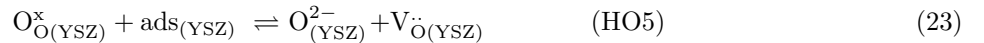
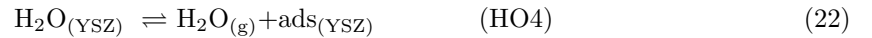
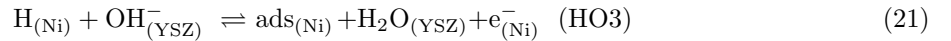
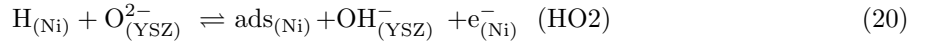
$$j_{tot} = \xi_{\text{TPB}_{an}} \cdot i_{o_{an}}^{\text{ct}} \cdot x_{H_2}^{r_{an1}^{\text{ct}}} \cdot x_{H_2O}^{r_{an2}^{\text{ct}}} \cdot \left[\exp\left(\alpha_{an}^a \frac{F}{RT_s} \eta_{an}^{\text{ct}}\right) - \exp\left(\alpha_{an}^c \frac{F}{RT_s} \eta_{an}^{\text{ct}}\right) \right] \text{ over } \Gamma_4 \quad (17)$$

The gas compositions at the interface are computed from the dusty-gas model. $\xi_{\text{TPB}_{an}}$ is a factor anticipating further implementation of degradation phenomena as described in Part II [69]. In the limiting case of a thick electrode, it does not depend linearly on the TPBL, but vary as the square root of the TPBL, i.e. $\xi_{\text{TPB}_{an}} = (A_{\text{TPB}_{an}}/A_{\text{TPB}_{ano}})^{0.5}$, as pointed out by Costamagna et al. [50]. Results of the present study show a good agreement with this case. The dependence on temperature of the exchange current is considered:

$$i_{o_{an}}^{\text{ct}} = T_s \cdot k_{o_{an}}^{\text{ct}} \cdot \exp\left[-\frac{E_{a_{an}}^{\text{ct}}}{R} \left(\frac{1}{T_s} - \frac{1}{T_{ref}}\right)\right] \quad (18)$$

A reference temperature is used to reduce the correlation between the pre-exponential factor and activation energy, and hence improves the quality of parameter estimations [99].

A reduction of the number of estimated parameters from individual measurements or physical consideration is always of interest. In this regard, the analytical approach of Zhu et al. [93] has a solid physical basis, yet remains compatible with parameter estimation at the SRU scale. However, the RDS has not yet been unambiguously identified, and considering a single RDS is evidently an oversimplification, see [82]. Evident transitions in the mechanism are unlikely, as the usual temperature range of IT-SOFC is lower than 1118 K [89,90]. The present study follows the set of limited elementary steps proposed by Zhu et al. [93]:



Two situations involving a single RDS are considered, yielding different apparent reaction orders and charge-

transfer coefficients:

$$j_{tot} = \xi_{\text{TPB}_{an}} i_{o_{an}}^{\text{ct}} \frac{\left(\frac{x_{H_2}}{\tilde{x}_{H_2}}\right)^{1/4} x_{H_2O}^{3/4}}{1 + \left(\frac{x_{H_2}}{\tilde{x}_{H_2}}\right)^{1/2}} \left[\exp\left(\frac{3}{2} \frac{F}{RT_s} \eta_{an}^{\text{ct}}\right) - \exp\left(-\frac{1}{2} \frac{F}{RT_s} \eta_{an}^{\text{ct}}\right) \right] \text{ at } \Gamma_4 \quad (24)$$

$$j_{tot} = \xi_{\text{TPB}_{an}} i_{o_{an}}^{\text{ct}} \frac{\left(\frac{x_{H_2}}{\tilde{x}_{H_2}}\right)^{1/4} x_{H_2O}^{1/4}}{1 + \left(\frac{x_{H_2}}{\tilde{x}_{H_2}}\right)^{1/2}} \left[\exp\left(\frac{1}{2} \frac{F}{RT_s} \eta_{an}^{\text{ct}}\right) - \exp\left(-\frac{3}{2} \frac{F}{RT_s} \eta_{an}^{\text{ct}}\right) \right] \text{ at } \Gamma_4 \quad (25)$$

$$\tilde{x}_{H_2} = \tilde{k}_{o_{an}} \exp\left[-\frac{\tilde{E}_{a_{an}}}{R} \left(\frac{1}{T_s}\right)\right] \quad (26)$$

Eq.24 and Eq.25 is obtained in case reaction 21 or reaction 20 is rate-limiting, respectively. The derivation of the former is presented by Zhu et al. [93], and the similar derivation of the latter is presented in Appendix A.1.

Modelling of diffusion and chemical processes. The apparent reaction orders in the Butler-Volmer expression and usually high fuel utilisation regime in SOFC stacks underscore the need for a reliable prediction of the gas composition at the anode/electrolyte interface. Preliminary in-house calculations with simpler diffusion models [37] exhibited somewhat similar limitations than those reported by Suwanwarangkul et al. [57]. On the anode side, the dusty-gas model [100] is solved in one-dimension through the anode support, along with the equation of continuity. The water-gas-shift reaction is assumed at equilibrium until the interface Γ_4 , between the anode and the electrolyte, whereas steam-methane reforming is computed according to the kinetic approach of Achenbach [33], as the species diffuse towards Γ_4 . The system of equations to solve is as follows:

$$-\frac{\partial}{\partial z} x_i - \frac{x_i}{p_{an}} \frac{\partial}{\partial z} p_{an} - x_i \frac{B_{o_{an}}}{\mu_{g_{an}} D_{iM}^e} \frac{\partial}{\partial z} p_{an} = \sum_{j=1, j \neq i}^n \frac{x_j N_i - x_i N_j}{c_{t_{an}} D_{ij}^e} + \frac{N_i}{c_{t_{an}} D_{iM}^e} \text{ in } \mathcal{R}_3 \quad (27)$$

$$\frac{\partial}{\partial z} p_{an} = \frac{\sum_{j=1}^n \frac{N_j}{D_{jM}^e}}{\frac{1}{RT} + \frac{B_{o_{an}}}{\mu_{g_{an}}} \sum_{i=1}^n \frac{x_i}{D_{iM}^e}} \text{ in } \mathcal{R}_3 \quad (28)$$

$$\frac{\partial}{\partial z} N_i = \mathfrak{R}_i \text{ in } \mathcal{R}_3 \quad (29)$$

$$\text{at } \Gamma_3 : \begin{cases} N_{H_2} = -N_{H_2O} = \frac{j_{tot}}{2F} \\ N_i = 0, \text{ i}=\text{N}_2, \text{CH}_4, \text{CO}, \text{CO}_2 \end{cases} \quad (30)$$

$$\text{at } \Gamma_3 : \begin{cases} x_{i_{an}} = x_i \\ p_{an} = p^{atm} \end{cases} \quad (31)$$

A main advantage of the Stefan-Maxwell approach for multi-component diffusion lies in the simplicity of the diffusion coefficients, which do not depend on the gas composition [100]:

$$D_{iM}^e = \frac{n_{an}}{\tau_{an}^2} \frac{d_n}{3} \sqrt{\frac{8RT_s}{\pi M_i}} \quad (32)$$

$$D_{ij}^e = \frac{n_{an}}{\tau_{an}^2} 1.43 \cdot 10^{-7} T_s^{1.75} \left(\frac{2}{1/M_i + 1/M_j} \right)^{-1} (\nu_{d_i}^{1/3} + \nu_{d_j}^{1/3})^{-2} \quad (33)$$

A fairly large amount of research has been performed to determine the catalytic activity of SOFC Ni-YSZ anode for methane steam-reforming. The proposed models range from detailed but heavy elementary heterogenous chemical kinetics models [51, 101] to simpler empirical relations. The kinetic approaches used here and proposed by Achenbach and Riensche [33] or Leinfelder [102] belong to the second category. It is believed that this level of detail is sufficient for the present application, if the range of operating conditions, i.e. temperature, steam-to-carbon ratios (SCR) and pressure, remains reasonable. However, significant differences exist between sources, which cannot be attributed to variations of microstructures or operating conditions. This is most evident for the apparent reaction orders [33, 102, 103]. The proposed relations can be expressed in a generic form:

$$\mathfrak{R}_{SMR} = \frac{k_{oan}^{SMR}}{h_{an}} x_{CH_4}^{r_{an1}^{SMR}} x_{H_2O}^{r_{an2}^{SMR}} \exp \left[-\frac{E_{aan}^{SMR}}{R} \left(\frac{1}{T_s} - \frac{1}{T_{ref}} \right) \right] \text{ in } \mathcal{R}_3 \quad (34)$$

It should be emphasised that both expressions [33, 102] do not account for any equilibrium and have been determined as averaged surface reaction rates. Furthermore, the temperature range of intermediate-temperature SOFC, i.e. 973-1073 K, is not included in the domain of validity of both relations (see Table

1).

[Table 1 about here.]

The equilibrium of the water-gas shift reaction is not strictly enforced but approximated by the following relation:

$$\mathfrak{R}_{\text{ws}} = k_{\text{oan}}^{\text{ws}} x_{\text{CO}} \left[1 - \frac{(x_{\text{CO}_2} x_{\text{H}_2}) / (x_{\text{CO}} x_{\text{H}_2\text{O}})}{K_{\text{ws}}^{\text{eq}}} \right] \text{ in } \mathcal{R}_3 \quad (35)$$

where $k_{\text{oan}}^{\text{ws}}$ is an arbitrarily high constant.

2.2.3 Cathode

The losses on the cathode side are acknowledged as the major contribution to the polarisation resistance of IT-SOFC, which motivated numerous investigations to identify the most promising materials. The amount of mechanistic studies on the ORR on perovskite cathodes exceeds that on the anode and originates from research on simpler systems, such as Pt-YSZ [104]. As expected, the difficulties encountered during the identification of the RDS and investigation methods display evident similarities to those discussed in Section 2.2.2: experiments on simple and functional geometries to understand the influence of the microstructure, identification of the dependence of the polarisation resistance on the oxygen partial pressure, overpotential and temperature from EIS measurements, models made of a sequence of elementary steps, of which one or two are rate-limiting, and, finally, considerable controversy [104].

Unlike the Ni-YSZ anode, the cathode is not necessarily a composite structure. Indeed, mixed-ionic and electronic conductors (MIEC) materials, such as LSCF, are extensively used in IT-SOFC. In MIEC materials with a significant ionic conductivity, the different elementary steps can be spread to a significant distance from the electrode/electrolyte interface, resulting in an overall increase of the effective zone [40]. The ionic conductivity of LSM in SOFC conditions remains limited, and the use of composite LSM-YSZ, or even LSCF-GDC [105] structures pursues the same aim of widening the electrochemically active zone. The means to improve the performance and mitigate degradation phenomena differ for the two technologies, since the processes involved in the ORR as well as their distributions are different. In a MIEC, the incorporation of oxygen ions in the ion-conducting electrode proceeds through surface reaction, whereas in the LSM-YSZ cathode, all elementary processes are confined to the distributed TPB. Therefore, the two main classes of cathodes found in IT-SOFC deserve a different handling for consistency, even for modelling at the SRU scale.

The knowledge of possibly co-limiting RDS and concurrent pathways for the reaction is the physical basis for the selection of modelling approaches at the SRU scale. The intrinsic properties of MIEC materials place much more importance on determining the ratio between bulk and surface pathways, compared with the Ni-YSZ case. Experiments performed on thick films [106,107] demonstrated the possible predominance of the bulk pathway for materials with a high ionic conductivity, and the small resistance to charge-transfer across SDC/LSC interfaces [107]. Therefore, the ORR in technological MIEC cathodes might not be necessarily limited by electrochemical kinetics, rather by chemical elementary steps. This is supported by the Gerischer shape usually observed in EIS for LSC [108] or LSCF [40].

The extensive research devoted to LSM, due to its chemical stability and coefficient of thermal expansion (CTE) close to those of other SOFC materials, has revealed its very complex behaviour. Tracer experiments on a LSM grid deposited on a YSZ substrate [109] have demonstrated the presence and likely interplay of the bulk and surface pathways. Furthermore, Siebert et al. [110] suggest the existence of a regime at high overpotential where enhanced ionic conductivity of LSM promotes the extension of the active zone. Van Heuveln et al. [94] have investigated the ability of different elementary reaction schemes to reproduce their experimental data on porous LSM electrodes and have proposed that the diffusion of adsorbed O^- species along the LSM surface and charge-transfer co-limit the ORR. Another suggested RDS is oxygen dissociation and adsorption, e.g. [111]. As a matter of fact, considerable discrepancy exists in the interpretation of experimental measurements. Most are based on equivalent circuit fitting, the weaknesses of which are often stressed, in particular one-to-one assignments [92, 104]. Anyway, Jorgensen et al. [112] have provided an extensive review of research carried out on LSM electrode to shed light on the behaviour of composite LSM-YSZ cathodes. They have identified five possible contributions from their data compilation, which includes their own and published measurements. The dominance and appearance of these contributions in EIS depend among others on manufacturing, test history and measurement conditions. The two high frequency arcs are related to transport and transfer of oxygen intermediates or oxides ions across the LSM-YSZ interface and through the YSZ backbone. The usually dominant and permanent arc located at intermediate frequencies is assumed to reflect separately or intricately dissociative adsorption, transfer of species to the TPB and surface diffusion. Finally, two low frequency arcs related to gas diffusion in the stagnant gas layer above the electrode and tentatively to impurity segregates at the TPB might appear. Jorgensen et al. [112] further emphasise the considerable variety in reported EIS, and indicate a possible variation of the apparent reaction order on oxygen in the range of 0-1, and activation energies in the range of 100-200 kJmol^{-1} for candidate RDS (145-183 kJmol^{-1} for the usually dominant arc at intermediate frequencies).

This high variability is further illustrated by the so-called activation phenomenon usually observed during the initial polarisation in performance testing of short stacks. Suggested causes are, among others, the dissolution of undesirable phases from impurities or manufacturing processes [112], or very localised changes in composition and morphology of the TPB [113]. At the SRU scale, this behaviour formally poses the question of a reference state.

Modelling studies on the underlying mechanisms of ORR are available in the literature, and can be selected and adapted for SRU models. Adler et al. [40] have developed a continuum, one-dimensional model of MIEC electrodes, which focuses on the bulk path. This approach is supported by the large amount of data on bulk diffusion D_v , surface kinetics K_{chem} and deviation from stoichiometry [114–121]. However, as pointed out by Adler et al. [122], most of this data holds only close to equilibrium, and extrapolation to large deviation is highly questionable. Their model enables an estimate of the utilisation length in the electrode, and displays agreement with measurements on good ionic conductors, such as LSC and LSCF [40]. The model however fails to represent the behaviour of LSM electrodes. The main reason is the aforementioned possibility of different pathways, which has been hence investigated by Svensson et al. [41] and later by Coffey et al. [44]. Similar to the case of the anode, these models require a large amount of reliable data, which is their major drawback as underscored by Coffey et al. [44]. Another limitation of one-dimensional continuum models arises once the extension of the active zone in the MIEC is similar to the particle size. The utilisation length and current distribution at the MIEC/electrolyte interface depends on the ratio K_{chem}/D_v [43], and hence they influence current constriction problems.

An identical modelling approach can be obviously applied to LSM-YSZ cathodes and Ni-YSZ anodes. The corresponding studies are usually not meant to clarify the contribution of underlying mechanisms, but rather seek to improve the performance of the electrode [9, 45, 50, 123]. None of the likely sequence of elementary mechanisms can be favoured in a generalised view of ORR in technological LSM-YSZ cathodes, even with the simplifications used at the SRU scale. In particular, as illustrated by Jiang et al. [124], the choice of co-limiting steps enables a fairly easy match of the oxygen partial dependence over a large temperature range. This emphasises the need for efficient calibration procedures to capture at least the correct dependences and enable a reliable prediction of the local performance and overall temperature distribution.

Composite electrode model: The present study uses the composite electrode model [9, 45, 50, 123] for the description of LSM-YSZ cathodes. It assumes that the ORR is restricted to the TPB, while electrons and ions are transported separately in the electronic and ionic phases. The charge balance is solved along

with mass transport [9, 45, 50]. The charge balance is described by the following system of equations:

$$\frac{\partial}{\partial z} V_{ion_{cath}} = -\rho_{ion_{cath}}^e j_{ion_{cath}} \quad \text{in } \mathcal{R}_5 \quad (36)$$

$$\frac{\partial}{\partial z} V_{el_{cath}} = -\rho_{el_{cath}}^e j_{el_{cath}} \quad \text{in } \mathcal{R}_5 \quad (37)$$

$$\eta_{cath} = (V_{ion_{cath}}^{eq} - V_{el_{cath}}^{eq}) - (V_{ion_{cath}} - V_{el_{cath}}) \quad \text{in } \mathcal{R}_5 \quad (38)$$

$$\frac{\partial^2}{\partial z^2} \eta_{cath} = A_{TPB_{cath}} (\rho_{el_{cath}}^e + \rho_{ion_{cath}}^e) i_{t_{cath}} \quad \text{in } \mathcal{R}_5 \quad (39)$$

$$\text{at } \Gamma_5 : \begin{cases} j_{ion_{cath}} = j_{tot} \\ j_{el_{cath}} = 0 \end{cases} \quad (40)$$

$$\text{at } \Gamma_6 : \begin{cases} j_{ion_{cath}} = 0 \\ j_{el_{cath}} = j_{tot} \end{cases} \quad (41)$$

A percolation theory is used to estimate the TPBL and effective conductivities (see Part II for description [69]).

Eq.42-Eq.43 are solved for the mass transport, and coupled to the charge-transfer problem by $i_{t_{cath}}$:

$$\frac{p_{cath}}{RT_s} \frac{\partial^2 x_{O_2}}{\partial z^2} = \frac{1}{4FD_{O_2}^e} A_{TPB_{cath}} i_{t_{cath}} \quad \text{in } \mathcal{R}_5 \quad (42)$$

$$\text{at } \Gamma_5 : D_{O_2}^e \frac{\partial x_{O_2}}{\partial z} = 0 \quad (43)$$

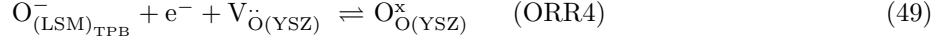
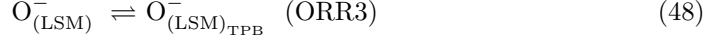
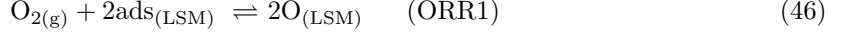
$$\text{at } \Gamma_6 : x_{i_{cath}} = x_i \quad (44)$$

The classical Bosanquet relation is used for the calculation of the overall effective diffusion coefficient, whereas the calculation of both Knudsen and binary diffusion coefficients proceed in a similar manner as for the anode.

$$\frac{1}{D_{O_2}^e} = \frac{1}{D_{O_2M}^e} + \frac{1}{D_{O_2-N_2}^e} \quad (45)$$

The selection of an expression for the transfer current for the present study is based on qualitative trend from the literature, due to the absence of extensive data (see Section 3). It should be considered as illustrative for the calibration of the SRU model. The sequence of elementary processes of van Heuveln et al. [9, 94] for

high temperature considers charge-transfer on adsorbed oxygen (ORR2) as RDS.



The surface diffusion step (ORR3) possibly co-limiting the ORR at low overpotential is not considered. The derivation of the apparent reaction order and charge-transfer coefficient presented by van Heuveln et al. [94] assumes a low coverage of adsorbed or intermediate oxygen species, which might hold at high temperature and low oxygen partial pressure, but not at low temperature [93, 124]. Hence, a modification is required for IT-SOFC. The derivation of the expression for the transfer current (see Appendix A.2) yields:

$$i_{t_{\text{cath}}} = i_{o_{\text{cath}}}^{\text{ct}} \frac{\left(\frac{x_{\text{O}_2}}{\tilde{x}_{\text{O}_2}} \right)^{3/8}}{1 + \left(\frac{x_{\text{O}_2}}{\tilde{x}_{\text{O}_2}} \right)^{1/2}} \left[\exp \left(-\frac{1}{2} \frac{F\eta_{\text{cath}}}{RT_s} \right) - \exp \left(\frac{3}{2} \frac{F\eta_{\text{cath}}}{RT_s} \right) \right] \quad (50)$$

$$i_{o_{\text{cath}}}^{\text{ct}} = T_s k_{o_{\text{cath}}} \exp \left[-\frac{E_{a_{\text{cath}}}}{R} \left(\frac{1}{T_s} - \frac{1}{T_{\text{ref}}} \right) \right] \quad (51)$$

Similar to \tilde{x}_{H_2} , \tilde{x}_{O_2} can be conveniently expressed as:

$$\tilde{x}_{\text{O}_2} = \tilde{k}_{o_{\text{cath}}} \exp \left[-\frac{\tilde{E}_{a_{\text{cath}}}}{R} \left(\frac{1}{T_s} \right) \right] \quad (52)$$

MIEC model. The approach used in the present study is a combination and simplification of the physical description proposed by Adler et al. [40] and Svensson et al. [41, 125]. One single path is considered: the surface adsorption of oxygen at the pore walls of the MIEC, followed by vacancy diffusion through the bulk,

and finally direct exchange of vacancies with the electrolyte.



The derivation of the model under the specific assumptions of the present study is recalled here, to highlight the nature of required data for the simulation at the SRU scale. The equations for the transport of vacancies in the bulk of the MIEC are derived by considering the MIEC as a moderately-dilute solution [126], containing ion vacancies, electrons and holes. The electrochemical potential is used as the driving force for the bulk diffusion of vacancies:

$$N_v = -\frac{D_v c_v}{RT} \frac{\partial \mu_v^*}{\partial z}, \quad (56)$$

where μ_v^* , the local electrochemical potential, depends on both the local electrical state and the local composition. The electrochemical potential of the electrons can be arbitrarily used to define a quasi-electrostatic potential Φ :

$$\mu_e^* = RT \ln c_e + z_e F \Phi \quad (57)$$

The expression of the gradient of the electrochemical potential of the vacancies can be rewritten as in [126], assuming the electron-hole pair reaction is at equilibrium [40]:

$$\frac{\partial \mu_v^*}{\partial z} = \frac{\partial}{\partial z} \left(\mu_v^* - \frac{z_v}{z_e} \mu_e^* \right) + \frac{z_v}{z_e} \frac{\partial \mu_e^*}{\partial z} \quad (58)$$

$$\frac{\partial \mu_v^*}{\partial z} = \frac{\partial}{\partial z} \left[RT \left(\ln c_v - \frac{z_v}{z_e} \ln c_e \right) \right] + \frac{\partial}{\partial z} \left[RT \left(\ln f_v - \frac{z_v}{z_e} \ln f_e \right) \right] + \frac{z_v}{z_e} \frac{\partial \mu_e^*}{\partial z} \quad (59)$$

hence the expression for the vacancy flux:

$$N_v = -D_v c_v \frac{\partial}{\partial z} \ln c_v + D_v c_v \frac{z_v}{z_e} \frac{\partial}{\partial z} \ln c_e - D_v c_v \frac{\partial}{\partial z} \left(\ln f_v - \frac{z_v}{z_e} \ln f_e \right) - \frac{z_v}{z_e} \frac{\partial \mu_e^*}{\partial z} \frac{D_v c_v}{RT} \quad (60)$$

$$N_v = -D_v c_v \frac{\partial}{\partial z} \ln c_v \left[1 - \frac{\partial \ln c_e^{\frac{z_v}{z_e}}}{\partial \ln c_v} + \frac{\partial \ln f_{v,e}}{\partial \ln c_v} \right] - \frac{z_v}{z_e} \frac{\partial \mu_e^*}{\partial z} \frac{D_v c_v}{RT} \quad (61)$$

$$N_v = -\mathcal{A} D_v \frac{\partial c_v}{\partial z} - \frac{z_v}{z_e} \frac{D_v c_v}{RT} \frac{\partial \mu_e^*}{\partial z} \quad (62)$$

where \mathcal{A} is defined as:

$$\mathcal{A} = 1 - \frac{\partial \ln c_e^{\frac{z_v}{z_e}}}{\partial \ln c_v} + \frac{\partial \ln f_{v,e}}{\partial \ln c_v} \quad (63)$$

The factor \mathcal{A} is a measurable thermodynamic quantity. Indeed, from the definitions:

$$\mu_v^* = \mu_{v,e}^* + RT \ln(f_{v,e} c_v c_e^2) - 2\mu_e^* \quad (64)$$

$$\mu_{O_2}^{chem} = \mu_{O_2}^{chem_o} + RT \ln(p_{O_2}) \quad (65)$$

The following relation holds (at the pore wall, at equilibrium, $\frac{1}{4}\mu_{O_2}^{chem} = \mu_h^* - \frac{1}{2}\mu_v^*$):

$$\mathcal{A} = \frac{\partial \mu_v^*}{\partial \ln c_v} = -\frac{1}{2} \frac{\partial \ln x_{O_2}}{\partial \ln c_v} \quad (66)$$

The problem due to the assumptions on the different elementary steps for the oxygen adsorption at the pore wall is overcome by using an apparent exchange coefficient, experimentally determined, close to equilibrium, for common LSCF. The simplified exchange reaction at the MIEC/gas interface is considered as an average volumetric reaction rate due to the 1D description.

$$\mathfrak{R}_{\text{MIEC}} = \frac{K_{chem} c_v}{\mathcal{A}} \left(\mathcal{A} \frac{c_v - c_v^{eq}}{c_v} + \frac{1}{2} \frac{x_i - x_i^{eq}}{x_i} \right) \quad (67)$$

Simple empirical relations proposed by Yang et al. [127] are used to estimate the dependence of the exchange coefficient on temperature and oxygen partial pressure in the gas found in literature, for LSCF and LSF, the two most common materials used in technological cathodes [114–121]. The same applies to the concentration

of vacancies at equilibrium in the perovskite and the diffusion coefficient.

$$D_{chem} = \mathcal{A}D_v = D_{o_v} \exp\left(-\frac{E_{a_v}}{RT}\right) \quad (68)$$

$$K_{chem} = C_{K_1} \exp\left(-\frac{E_{a_K}}{RT}\right) x_{O_2}^{C_{K_2}+C_{K_3}T} \quad (69)$$

$$c_v^{eq} = \frac{\delta}{V_m} = 3C_{\delta_1} \exp\left(-\frac{E_{a_\delta}}{RT}\right) x_{O_2}^{C_{\delta_2}+C_{\delta_3}T} \quad (70)$$

Insertion of Eq.62 and Eq.67 in the vacancy conservation equation, $-\partial N_v/\partial z - A_{\text{MIEC}}\mathfrak{R}_{\text{MIEC}} = 0$, yields the one-dimensional steady-state conservation equation:

$$\frac{1 - n_{cath}}{\tau_{cath}} \left(\mathcal{A}D_v \frac{\partial^2 c_v}{\partial z^2} + D_i \frac{\partial c_v}{\partial z} \frac{\partial \mathcal{A}}{\partial z} + \frac{z_v}{z_e} \frac{D_v c_v}{RT} \frac{\partial^2 \mu_e^*}{\partial z^2} + \frac{z_v}{z_e} \frac{D_v}{RT} \frac{\partial c_v}{\partial z} \frac{\partial \mu_e^*}{\partial z} \right) - A_{\text{MIEC}}\mathfrak{R}_{\text{MIEC}} = 0 \quad (71)$$

For modelling at the SRU scale, assuming a high electronic conductivity of the MIEC, i.e. $\nabla \mu_e^* = 0$ is an acceptable simplification, and $\nabla \mathcal{A} = 0$ is reasonable in the considered range of oxygen partial pressure for the typical MIEC materials used in SOFC:

$$\frac{1 - n_{cath}}{\tau_{cath}} \left(\mathcal{A}D_v \frac{\partial^2 c_v}{\partial z^2} \right) - A_{\text{MIEC}}\mathfrak{R}_{\text{MIEC}} = 0 \quad \text{in } \mathcal{R}_5 \quad (72)$$

Simplified boundary conditions are:

$$j_{tot} = -2F \frac{1 - n_{cath}}{\tau_{cath}} D_{chem} \frac{\partial c_v}{\partial z} \quad \text{at } \Gamma_5 \quad (73)$$

$$0 = \frac{1 - n_{cath}}{\tau_{cath}} D_{chem} \frac{\partial c_v}{\partial z} \quad \text{at } \Gamma_6 \quad (74)$$

The diffusion problem described previously (Eq.42 and Eq.43) still holds, except that $A_{\text{TPB}_{cath}} i_{t_{cath}}$ has to be replaced by $A_{\text{MIEC}}\mathfrak{R}_{\text{MIEC}}$.

The exchange of vacancies between the MIEC and the electrolyte Eq.55 formally involves a charge-transfer, modelled by a Butler-Volmer equation [41] :

$$j_{tot} = i_{o_{cath}}^{ct} \left[\exp\left(\frac{(1-\alpha)zF}{RT_s} \eta_{cath}^{ct}\right) - \exp\left(\frac{-\alpha zF}{RT_s} \eta_{cath}^{ct}\right) \right] \quad \text{at } \Gamma_5 \quad (75)$$

$$i_{o_{cath}}^{ct} = k_{o_{cath}}^{ct} \left(\frac{c_v}{c_v^{eq}} \right)^{1-\alpha} \exp\left[\frac{E_{a_{cath}}}{R} \left(\frac{1}{T_s} - \frac{1}{T_{ref}} \right) \right] \quad (76)$$

This term is likely not dominant for an LSCF/GDC interface [104] and therefore neglected in the present study. In the case of a direct exchange of vacancies at the interface, a supply term appears and is computed as output [41]:

$$\eta_{cath} = -\frac{RT_s}{2F} \ln \frac{c_v|_{\text{MIEC-elect}}}{c_v^{eq}}, \quad (77)$$

2.3 Parameter estimation

gPROMS [65] has parameter estimation and design of experiment capabilities, the comprehensive description of which is beyond the scope of this study. Only a brief survey is provided here, to illustrate the reported statistical results. The present SRU model is a set of partial differential equations and differential algebraic equations.

$$\mathcal{P}(\tilde{u}, \theta) = F \left(x_1, \dots, x_d, t, \tilde{u}, \frac{\partial \tilde{u}}{\partial t}, \frac{\partial \tilde{u}}{\partial x_1}, \frac{\partial \tilde{u}}{\partial x_d}, \frac{\partial^{p_1+\dots+p_d+p_t} \tilde{u}}{\partial x_1^{p_1} \dots \partial x_d^{p_d} \partial t^{p_t}}, \vartheta, \theta \right) = 0 \quad (78)$$

$$f \left(x_1, \dots, x_d, t, u, \frac{\partial u}{\partial t}, \vartheta, \theta \right) = 0 \quad (79)$$

The experiment provides access to the outputs y , which are some of the unknowns \tilde{u} , such as SRU voltage or average current density. ϑ contains the time-varying and time-invariant controls, which can be manipulated during the experiment, e.g. gas flow, composition, temperature or current. In contrast, θ represents the set of parameters of the electrochemical model that have to be determined experimentally. The calculation of the sensitivity matrix \mathbf{Q} , which is the predicted sensitivity of the outputs to the parameters, is paramount in parameter estimation and design of experiment theories. In a linear model, the sensitivity matrix contains the coefficients of the model, while in a non-linear model, the sensitivity matrix has to be evaluated locally at the best current estimates of the parameters $\hat{\theta}$.

$$[\mathbf{Q}]|_{\hat{\theta}} = \left. \frac{\partial \hat{y}_i}{\partial \theta_j} \right|_{\hat{\theta}}, \quad \text{where } i = 1 \dots \mathcal{N}_{resp}, \quad j = 1 \dots \mathcal{N}_{para} \quad (80)$$

In a dynamic system, \mathbf{Q} depends on the initial conditions, trajectories, sampling time and parameters.

Parameter estimation is achieved in the form of an optimisation problem, where the objective function

is based on the normal probability distribution (its natural logarithm).

$$\Psi = \frac{\mathcal{N}}{2} \ln(2\pi) + \frac{1}{2} \min_{\hat{\theta}} \sum_k^{\mathcal{N}_{rep}} \left\{ \sum_i^{\mathcal{N}_{resp}} \sum_j^{\mathcal{N}_{exp}} \left[\ln(s_{ij}^2) + \frac{(\hat{y}_{ij} - y_{ij})^2}{s_{ij}^2} \right] \right\}_k \quad (81)$$

This objective function takes into account the variance in the measurements. Indeed, the residuals are weighted by their variance, and therefore, favored for their increased reliability.

Once the parameters have been estimated, it is essential to statistically evaluate the adequacy of the model, by means of a careful analysis of the residual distribution and statistical tests. gPROMS [65] provide three main indicators, the significance of which can be qualitatively seen in light of the parallel drawn previously between linear (multilinear regression) and non-linear model. The first one is a lack-of-fit test. The sum of squares of the residuals $SS(\hat{\theta})$ is the result of the contribution of measurement errors, assumed to follow a normal distribution and of lack-of-fit (LOF)

$$SS(\hat{\theta}) = s^2 + \text{LOF} \quad (82)$$

A χ^2 -value can be tested against a χ^2 -distribution with $(n - p)$ degrees of freedom.

$$\chi^2 = \frac{SS(\hat{\theta})}{s^2} < \chi_{\beta, n-p}^2 \quad (83)$$

If the χ^2 -value is smaller than those in the distribution, then the model fits adequately to the data. A F -value may then be tested against a F -distribution with $(n - p - r)$ and $(r - 1)$ degrees of freedom

$$F_d = \frac{\frac{SS(\hat{\theta}) - r \hat{s}^2}{(n - p - r)}}{\hat{s}^2} < F_{\beta, n-p-r, r-1} \quad (84)$$

Again, if the F -value is smaller than those in the F -distribution, then the model fits adequately the data. Aside from testing the adequacy of the model, the statistical significance of the estimated parameters can be tested using a Student t -test for each parameter $\hat{\theta}_i$

$$t_i = \frac{\hat{\theta}_i}{\sqrt{V_{ii}}} > t_{\beta, n-p} \quad (85)$$

where V_{ii} is the variance of the i th parameter. If the t -value is larger than those of the t -distribution of degree of freedom $(n - p)$ then the estimate tends to be reliable. On the contrary, if the t -value is lower,

the parameter can eventually be dropped out. Low t -value can also indicate the correlation between some parameters.

Joint confidence regions are also useful to assess the reliability of parameter estimates. A linear approximation of the parameter variance-covariance matrix \mathbf{V} is given by

$$\mathbf{V} = (\mathbf{Q}^T \mathbf{Q})^{-1} \frac{SS(\hat{\theta})}{n - p} \quad (86)$$

and the linear approximation $(1 - \beta)$ of the joint confidence region of the parameters can be calculated

$$(\theta - \hat{\theta})^T \mathbf{Q}^T \mathbf{Q} (\theta - \hat{\theta}) \leq p s^2 F_{\beta, p, n-p} \quad (87)$$

Care should be taken, as these approximations may be unreliable in the case of important non-linearity.

This quick description of statistical tests and objective functions underscores the importance of the accuracy of the variance model. A preliminary study has shown that DOE procedures are highly dependent on the selection of the variance model. However, in the particular case of a constant variance model, a wrong variance does not affect the parameter estimation and only invalidates the statistical tests.

3 Experimental

The calibration of the models is performed on current-voltage (IV) characteristics measured by means of two different segmented-cell test rigs, the detailed description of which is provided elsewhere [66,67]. Only the key features of the experiments are discussed here.

The two setups are designed for different purposes. The first one, developed at the German Aerospace Center (DLR) aims at studying the variation of SOFC characteristics over a generic geometry [66], while the second, developed at LENI-EPFL, aims at identifying and mitigating issues related to a specific SRU design [67]. This implies different arrangements of the segments, as depicted in Figure 1a and b. The present study takes advantage of the capability of segmented tests to gather simultaneously a large amount of data for different currents, potentials, temperatures and gas compositions. For this purpose, the usefulness of both setups is identical. The ease of data processing and suitability for parameter estimation slightly differ, however, in favour of the DLR setup, owing to the continuous arrangement of the segments, better uniformity of the fuel flow and increased gas-tightness of the cathode compartment.

The DLR setup can accommodate metal-, electrolyte- or anode-supported cells of 100 cm². The active

area for measurements is 73.8 cm^2 , divided into 16 electrically-isolated segments of 4.6 cm^2 , equally distributed over the active area of the SRU (see Figure 1b). Gases can be supplied in either co- or counter-flow configuration. Mixtures of H_2 , H_2O , CO , CO_2 , CH_4 and N_2 can be fed into the anode compartment, within the safe ranges to prevent carbon deposition, limited by the maximum achievable amount of steam of 3%. The molar fraction of O_2 in the cathode gas can be varied as well.

The LENI-EPFL setup is based on the SRU design developed within the frame of the FLAMESOFC project [7, 8, 67, 70]. The shape of the SRU with an active area of 200 cm^2 is depicted in Figure 1a, along with the arrangement of the 18 segments of 1.7 cm^2 . Local measurements are not performed on the remaining active area, reduced to 133 cm^2 , due to the implementation of the segmentation. All segments can be independently polarised or not, to measure the local Nernst potential which gives an assessment of the quality of the gas distribution [67]. Experiments are carried out with air, while nitrogen-diluted or not, wetted or dry hydrogen is fed on the fuel side. Data on the extensive post-mortem analysis is available elsewhere [67, 70].

In the case of an anode-supported cell, only the cathode can be segmented. An ASC2 cell (InDec, Netherland) has been tested in the DLR setup. It consists of a $540 \mu\text{m}$ thick anode, a $7 \mu\text{m}$ YDC compatibility layer on top of the $7 \mu\text{m}$ 8YSZ electrolyte. The thickness of the LSCF cathode along with its current collection layer is $60 \mu\text{m}$. An anode compensating layer is added to reduce the curvature of the cell. A similar anode support has been tested in the LENI-EPFL setup, but with a LSM-YSZ composite cathode (HTceramix, Switzerland), screen-printed on the 8YSZ electrolyte. The typical operating conditions applied during both tests and used for model calibration here are listed in Table 2.

[Table 2 about here.]

4 Investigated cases

The following model variations, described in Section 2, are tested against the experimental data:

- 3 different approaches for the description of the electrochemical processes on the anode side, one empirical (referred to as EMP, Eq.17) and two based on different RDS (Eq.24, HO3 and Eq.25 , HO2).
- Two different sets of parameters for the calculation of \tilde{x}_{O_2} (Eq.52) [124, 128].
- Two empirical relations (Eq.34 and Table 1) for internal steam-methane reforming in SOFC anodes, from Achenbach and Riensche [33] and Leinfelder et al. [102].

The particularities of the two setups imply distinct processing strategies. The data gathered by the DLR setup is more extensive in terms of measurement points and conditions. Four units of the one-dimensional model with the electrochemical model for a MIEC cathode material are assembled to model one single row of segments (see Figure 1). The setting of the inlet gas flow rate assumes a uniform distribution. To partially overcome this simplification, the calculation of the variance includes the responses recorded on the two central rows. This modelling strategy provides increased accuracy, compared with a previous simpler approach, based on averaged conditions for each segment. This is due to the uneven distribution of temperature and gas species, and current leakage, which prevent the calculation of the inlet condition for a segment from the current drawn from the upstream ones. The available specific variations of temperature, gas flow rates, and anode and cathode gas compositions are spread over a time period of 325 h. Degradation phenomena can therefore affect the accuracy of the calibration. The approach pursued here is not meant to clarify the reasons for the degradation, but seeks to avoid the overestimation of parameters affected by operating conditions varied at the end of the measurement campaign. Two degradation phenomena, the loss of ionic conduction of the electrolyte and of electronic conduction of the uncoated MIC due to corrosion, are arbitrarily applied to correct the data for the observed overall degradation. Their simple modelling is provided in Part II [69]. Results with and without application of the correction for degradation are compared.

The data from LENI-EPFL is smaller in amount and affected by experimental contingencies, such as a marked local degradation at the inlet of the SRU due to contamination of the cathode from volatile species transported by the air, and small deficiencies in the anode flow field. Insights into the improvement cycles of the design from this diagnostic is provided in [67]. As a result, only data from segment 2,3 and 4 are suitable for the present study. The discontinuous experimental discretisation of the central line (segments 1 to 6) prevents the straightforward use of the one-dimensional modular model for the in-plane direction, as the local current density is not resolved in the main area. Therefore, averaged conditions over the segments are computed by a 2D model [69] and applied as local conditions on the electrochemical model alone. An ohmic resistance is added in the inlet area delimited by segment 1 to coarsely model the large degradation and to prevent an underestimation of the hydrogen molar fraction on the downstream segments.

The choice of the fitting parameters, as listed in Table 4, is dictated by considerations on the possible dedicated experiments, which should be included in a comprehensive calibration procedure. The following parameters are fixed according to data from literature, despite the scatter in the reported values:

- The electronic and ionic conductivities of all materials ($k_{o_{ion}}$, $E_{a_{ion}}$, $k_{o_{el}}$, $E_{a_{el}}$).
- The morphological parameters of the electrode, only those of the cathode being all explicitly required

in the present study, to compute the effective conductivities and TPBL (r_{el} , r_{ion} , ϕ_{el} , ϕ_{ion} , l_g , d_g , n , d_n).

- The tortuosity of the porous and solid network in the cathode (τ_{cath}).
- One set of parameters for the calculation of \tilde{x}_{H_2} (Eq.26), two sets for \tilde{x}_{O_2} (Eq.52).
- Two different sets of parameters for the steam-methane reaction ($k_{o_{an}}^{SMR}$, $E_{a_{an}}^{SMR}$, $r_{an_1}^{SMR}$, $r_{an_2}^{SMR}$) (Eq.34 and Table 1).
- The dependence on temperature and oxygen partial pressure of the surface (Eq.69) and bulk (Eq.68) properties of the LSCF cathode material (E_{a_v} , E_{a_K} , C_{K_2} , C_{K_3}) (Figure 4).
- The parameters for the calculation of the deviation from stoichiometry in the LSCF cathode (C_{delta_1} , C_{delta_2} , C_{delta_3} , $E_{a_{delta}}$) (Eq.70 and Figure 4).
- The internal surface area of the LSCF cathode (A_{MIEC}).

The fitting parameters are therefore:

- The parameters for the description of the electrochemical processes in the anode : $k_{o_{an}}^{ct}$ and $E_{a_{an}}^{ct}$ for HO3 and HO2, $r_{an_1}^{ct}$, $r_{an_2}^{ct}$ are added for the empirical relation EMP (Eq.17).
- The parameters for the description of the electrochemical processes in the cathode (Eq.50), $k_{o_{cath}}^{ct}$ and $E_{a_{cath}}^{ct}$.
- The pre-exponential factor for the diffusion of vacancies (D_{o_v}) (Eq.68).

The ratio of the surface to bulk properties is a key value which controls the extension of the active zone in an electrode made of a MIEC material [40, 43]. Therefore, while D_{o_v} is fitted, C_{K_1} is accordingly varied, constrained by the ratio K_{chem}/D_{chem} . Figure 4 depicts the surface properties and deviation from stoichiometry implemented in the model.

The calibration sequence starts with the data gathered by the DLR setup. Parameter estimation runs are first performed on measurements with hydrogen as fuel, with the three anode models (EMP, HO2, HO3). Some experiments are not included, but used separately to verify the reliability of the calibrated model. Measurements with internal steam-methane reforming are sparse and the variations limited by the maximum amount of steam of 3%. Therefore, the parameters of the empirical relation Eq.34 are not estimated. The data is used to discriminate between the parameters provided by Achenbach and Riensche [33] or Leinfelder et al. [102]. Thanks to the similar anode support used in all experiments, the data from LENI-EPFL are used to estimate only the parameters of the cathode composite model. The calibration is performed separately with the three previously calibrated anode models (EMP, HO2 and HO3).

The differences in behaviour between the three anode models and two cathode materials are assessed at the SRU level on a one-dimensional description of the non-segmented version of the SRU depicted in Figure 1a. Adiabatic boundary conditions are set, inducing temperature differences exceeding 100 K, typical of a SRU embedded in a stack.

[Table 3 about here.]

[Table 4 about here.]

[Figure 4 about here.]

5 Results and discussion

5.1 Parameter estimation, case of a MIEC cathode

The variance in the measurements affects the information conveyed by the experiments. Its assessment is required to evaluate the adequacy of a model and whether the quality of the data is sufficient to discriminate between different models. In the case of the data gathered at DLR, imprecision in the data used for parameter estimation originates both from limitations of the experimental setup and the choice of the measurement sequence (Section 4).

[Figure 5 about here.]

Figure 5 depicts the IV curves measured on the two central rows of the DLR setup, for different gas flows and hydrogen inlet molar fractions, from 10% to 50%, at 1073 K. The onset of limitation shifts towards lower current densities, along the flow path, due to the depletion of hydrogen. The conditions yielding the highest current densities in Figure 5 are referred to as the nominal operating point: the furnace temperature is set at 1073 K, and air (80 nmlpm cm^{-2}) and 50% diluted wet hydrogen (25 nmlpm cm^{-2}) are fed in the cathode and anode compartments, respectively. Measurements in these conditions are available at different operating times. The effects of the degradation phenomena are significant over the time period included in Figure 5, from 136 h to 377 h. These induce a maximum decrease in cell voltage of approximately 55 mV. The corresponding value of the variance is used for the parameter estimation, whether correction for the degradation is applied or not on the data. This conservative simplification is believed to be sufficient, owing to the experimental sequence, which has not been optimised for model calibration. A comparison in Figure 5 of the response of segments located at identical positions along the flow path shows that the measurement

error can be potentially much smaller. A refinement that is enabled in gPROMS [65] would consist in using a distinct heteroscedastic variance model for each segment. The degradation does not drastically affect the pattern of the measured IV characteristics over the considered time period, which allows for the relevance, for practical use, of the addition of degradation phenomena inducing an increase of the ohmic losses to correct the data.

[Figure 6 about here.]

Figure 6 provides a comparison between the experimental data from various segments and the predictions provided by the HO2 model, calibrated with a correction for the degradation (see also Figure 7). The agreement is acceptable over a wide range of local conditions which are representative of those in a SOFC stack. The emphasis in the parameter estimation runs is placed on the variation of the temperature and anode gas composition, as in most cases a high air ratio is required for the thermal management of a functional stack. Experiments with the lowest inlet oxygen molar fraction of 0.02 are not fitted satisfactorily (not depicted), despite the validity of Eq.68-Eq.70 in this range (see Figure 4). Difficulties concern mainly the detection of the onset of limitation. An unlikely high tortuosity of the gas phase in the cathode is required to reproduce the data. One reason is the one-dimensional discretisation of the cathode, which cannot capture limitations caused by the geometry of the GDL system, when coupled to a thin electrode. The range over which the calibration is acceptable remains however wide enough to ensure a reliable prediction of the behaviour of a functional SRU, to show the relevance of a MIEC model at the SRU scale and to confirm the dependences included in Eq.68-Eq.70 [118, 119].

A word of caution is warranted on the assessment of the validity of a model from the quality of a fit. Previous calibrations with simpler models, the terms of which lack a strict physical meaning, such as Wilcke formulation for diffusion losses on the anode side, or Butler-Volmer equation to describe the electrochemical processes in the MIEC cathode, produced satisfactorily agreement with part of the dataset shown in Figure 6, except significant discrepancies that occurred for the highest hydrogen and oxygen dilutions.

The details of the results of the parameter estimations are listed in Table 5, for the three anode models and correction or not for the degradation. The values of the objective function ψ are directly comparable, as the same dataset is used for all calibrations. The lowest objective function, i.e. the best fit, is obtained with the EMP model, with a correction of the data for the degradation. The two other models based on physical assumptions on the anode RDS yield comparable results in terms of overall quality. All runs listed in Table 5 successfully pass the adequacy tests described in Section 2.3. The choice of the fitting parameters and the use of a reference temperature prevent high correlations between the parameters. The optimal values,

along with their confidence intervals, fall within the ranges reported in the literature (see Section 2.2.2): 70-170 kJmol⁻¹ for $E_{a_{an}}^{ct}$, -0.5 to 1.0 and 0.3 to 1.0 for the apparent reaction orders on hydrogen and steam, respectively. The estimated tortuosity around 3.6 is slightly higher than expected [129]. Possible reasons are the one-dimensional discretisation which does not account for the geometry of the GDL system and the presence of the contacting and compensating layers. The fitted value is therefore an averaged one which lumps the mass transfer resistance of all functional layers and that of the GDL. The EMP model yields slightly lower values of the tortuosity, since $r_{an_1}^{ct}$ and $r_{an_2}^{ct}$ modify the apparent onset of diffusion limitation. The optimal values of 0.29 and 0.62 are close to those set in the HO3 model.

[Table 5 about here.]

The computed 90% confidence intervals are overall between 2-25% of the estimated value. These do however not contain the optimal value of all parameter estimation runs. The tightest intervals, between 2-12%, are obtained with the HO2 model, with correction of the data, partly due to the reduced number of estimated parameters. The different models predict comparable contributions of the cathode, expressed by D_{o_v} in Table 5.

The implementation of a correction for the degradation noticeably reduces the objective function. The furnace temperature has been varied at the end of the experiment, after 400 h of operation. As the temperature dependence of all contributions, except that of the anode, are fixed, the degradation induces higher activation energy of the hydrogen oxidation, if the data is not corrected. This effect is less pronounced for the EMP model, as the apparent reaction orders can be varied. Figure 7 shows the effect of the correction for the degradation on IV characteristics for the standard operating conditions, recorded at 201 h and 377 h. The overall trend is well reproduced, but the subtle changes in the onset of diffusion limitation are not modelled.

Operation with methane achieves higher efficiency than with hydrogen. While internal steam-methane reforming can be beneficial for the thermal management of the stack, structural issues can arise from its endothermic nature. A calibration under these conditions of higher technological relevance is essential to ensure the reliability of a SRU model. The DLR setup does not comprise an evaporator, which drastically limits the achievable testing conditions with methane. Therefore, the data is too sparse in amount to estimate reliably the parameters of Eq.34. Instead, the parameters listed in Table 1 are discretely tested. Despite the low current densities due to the steam molar fraction limited to 3%, the IV characteristics predicted with the relation from Achenbach and Riensche [33] or Leinfelder et al. [102], are significantly different,

in favour of the former. The choice of an anode model does not drastically alter the simulated responses, despite the differences in the apparent reaction orders on hydrogen and steam. The EMP model exhibits a slightly better agreement. Figure 7 includes the comparison between measurements and simulations with the relation from Achenbach and Riensche [33], without any specific adjustment of the parameters. Unlike experiments carried out with hydrogen as fuel, the current density increases along the flow path, as methane is progressively reformed. The model correctly captures this trend. Figure 8 shows the simulated distribution of methane and hydrogen in the anode, along a row of segments, for the operating points characterised by the highest current density in Figure 7. The molar fraction of methane decreases along the flow path in the gas channel and towards the interface. That of hydrogen, depicted by the ribbons, exhibits a maximum in the anode in the upstream segment and overall increases along the flow path, which accounts for the higher potential at the outlet. The results confirm the assertion that acceptable predictions of the behaviour under internal steam reforming can be achieved with a simplified modelling approach, based on the electrochemical conversion of hydrogen, coupled to an empirical kinetic relation for the steam-methane reforming. The present study however relies on a limited number of experiments, performed with highly-diluted methane. A reliable calibration of the models requires an additional measurement campaign, on a setup equipped with an evaporator.

[Figure 7 about here.]

[Figure 8 about here.]

5.2 Parameter estimation, case of a composite LSM-YSZ cathode

The main feature of the LENI-EPFL experiment is its design-oriented nature. The gas manifold is identical to that of a functional stack. Issues related to the anode flow affected the measurements and have been subsequently addressed [67]. The present study overcomes this limitation by using the values of the anode parameters estimated with the DLR data, thanks to the similar anode used in both experiments. Another drawback of the LENI-EPFL experiment for the present study is the difficulty to vary the oxygen molar fraction on the cathode side. This is inherent to the setup, which has an air manifold dimensioned for a stack and consequently increased relative gas leaks.

[Figure 9 about here.]

Figure 9 shows the results of the parameter estimation. All curves exhibit the same pattern, as only the measurements on the central segments, 2 to 4 (see Figure 1), are usable for the present study. The differences

between the two experiments carried out after 15 h and 23 h of operation are the dilution and flux of the anode gas. Despite the fixed furnace and gas inlet temperature, the temperature range in the data is of approximately 20 K, owing to the polarisation and locations of the segments.

Table 6 lists the results of the parameter estimations. The limited amount of data induces large confidence intervals and a high correlation between the parameters. The lowest objective function ψ is achieved with the HO2 model, along with the use of the parameters from Matsuzaki et al. [128] for the calculation of \tilde{x}_{O_2} . The optimal values of the cathode activation energy falls within the range of 100-200 kJmol⁻¹ reported in the literature.

[Table 6 about here.]

5.3 Simulations of the behaviour of a repeating unit

The results of the parameter estimations described in Section 5.1 and Section 5.2 do not allow discriminating between the different models: the objective function is the lowest for the EMP model, and acceptable predictions can still be obtained without a correction of the data for the degradation. Further investigations, with the help of design of experiment theories, are required to determine whether the data gathered by the kind of experiments used in the present study are of any help for model discrimination. The rationale behind the development and calibration of the present electrochemical model is the further implementation of degradation phenomena for the prediction of lifetime and identification of structural failures. Because of the failure of the unambiguous selection of model assumptions, it is crucial to verify if the choice of a model critically affects the prediction of the field variables driving the degradation phenomena included in Part II of this study [69], over the range of local conditions found in a SRU in operation. The other aim of this section is to identify any inconsistent behaviour, hence to confirm or infirm the physical meaning of the values of the optimal values of the parameters.

[Figure 10 about here.]

Figure 10 compares the response of the SRU shown in Figure 1c, embedded in a stack, with a cell based on a LSM-YSZ or LSCF cathode, operated in co- or counter-flow configuration. The case of partially pre-reformed methane fed in the SRU (see Table 3) is considered, as it tests all the features of the model and induces the largest variety of local conditions. The air ratio is coarsely adjusted to yield a maximum local temperature of 1100 K in the SRU for both co- and counter-flow cases, at a fuel utilisation of 0.8-0.85. The behaviour is barely affected by the choice of an anode model. As expected, the LSCF cathode has a

better performance than LSM-YSZ (e.g. [130]). The same applies to the comparison between counter- and co-flow configuration, at the cost, however, of a higher air ratio for the former. The difference in behaviour is amplified by the endothermic nature of the steam-methane reforming: at a fuel utilisation of 0.8, the temperature difference over $\mathcal{R}_{\text{area}}$ (see Figure 1c), for the case of a LSCF cathode, is of 148 K in co-flow, against 115 K in counter-flow. The gain of the counter-, compared with co-flow, with hydrogen as fuel is less pronounced, as the lowest temperature in the SRU is higher than the air inlet temperature in any case. Indeed, the distribution of the current density follows a trade-off in the co-flow configuration, between highest temperature (low ohmic and electrochemical resistances) and depleted fuel (low local Nernst potential and high anode diffusion losses), both located at the air outlet of the active area. The noticeable decay of the potential at low current density is due to the evolution of the maximum temperature which increases from 950 K to 1203 K (co-flow, LSM-YSZ cathode), as the polarisation proceeds.

[Figure 11 about here.]

Figure 11 provides the details of the contribution of the cathode and the Nernst potential, including resistance to mass transfer in the electrode. The higher performance of LSCF is explicitly seen. The difference between the anode models is consistent with the optimal values of D_{o_v} listed in Table 5, that of the calibrated EMP model being the highest. The zone of highest current density, as observed in Figure 12 moves towards the fuel inlet at the highest fuel utilisation, which induces different trends in the evolution of the ASR of the cathode in co- and counter-flow configurations. In the co-flow case, this shift results in a monotonic increase of the local temperature all over the active area. In contrast, in the counter-flow case, the local temperature decreases at the end of the IV characterisation, over approximately the first half of the SRU, from the air inlet. This phenomenon in turn amplifies the relative increase of the local current density at the fuel inlet. The onset of diffusion limitation is higher and shifted towards lower fuel utilisations in the co-flow, compared with the counter-flow case, owing to the distribution of the Nernst potential and lower rate of the steam-methane reforming reaction in the anode in the zone of highest current density.

[Figure 12 about here.]

The design of a SRU in view of its long-term performance relies on the prediction of the distribution of the field variables driving the degradation. The modelling approach described in Part II [69] assumes a predominant effect of the overpotential on the risks of formation of lanthanum (LZO) or strontium zirconates (SZO) and chromium contamination in a LSM-YSZ cathode, as suggested by recent studies [17,131]. Figure 12 shows the distribution over the active area $\mathcal{R}_{\text{area}}$ of the anode and cathode contributions, and Nernst

potential, computed at the interfaces between the electrolyte and electrodes, Γ_4 and Γ_5 . The fuel utilisation is of 0.8 and the corresponding temperature differences over the active area are 152 K and 116 K in co- and counter-flow, respectively. The fuel flow direction is kept constant. Thus, the zone of highest temperature is inverted between co- and counter flow. The effect of the previously discussed trade-off between temperature and anode gas composition driving the location of the maximum current density and uniformity of the local Nernst potential is clearly observed. The discrepancy between the profiles predicted by the different anode models is small. The contribution of the ORR on the cathode side to the overall losses consistently exceeds that of electrochemical processes on the anode side, over the whole active area. In contrast to the distribution of the current density, that of the Nernst potential and cathode overpotential is less uniform in the co-flow configuration. The local degradation rate cannot, however, be deduced from the profile of the overpotential, as the degradation phenomena have their own temperature dependence. For instance, the formation of LZO and/or SZO in the LSM-YSZ system is thermodynamically promoted by increasing the temperature [17]. Even though the respective effects of the current density and overpotential on the degradation are not yet clarified, this observation shows that designing a SRU to ensure an even current distribution can lead to misleading conclusions, depending on the dominant degradation phenomena.

[Figure 13 about here.]

The extension of the active zone in a cathode made of MIEC material depends on the ratio K_{chem}/D_v [43]. The extension predicted by the model is in the range of 10 μm , as deduced from the profile of the vacancy concentration c_v within the electrode depicted in Figure 13. This falls within the range of 2 to 22 μm reported in the literature [40], for other materials. The value of K_{chem}/D_v is determined from the data found in the literature (see Table 4), due to the choice of the fitting parameters described in Section 4. Therefore, an anode model does not alter the computed extension, but significantly affects the calculated concentration of vacancies at the interface between the cathode and the electrolyte. The MIEC model contains three activation energies for the calculation of the deviation from the stoichiometry, the diffusion of vacancies in the bulk of the cathode and the reaction at the pore wall. The effect of the first one, E_{a_δ} , is reflected in the value of c_v close to the gas channel. The value of the two others, E_{a_K} and E_{a_v} , are comparable, which, together with the high air ratio, yields a uniform distribution of the extension of the active zone. The deviation from stoichiometry enables the calculation of local isothermal expansions, which can lead to structural failure, depending on the type of cell and presence or not of localised zones of dramatically low oxygen content, due to a defective sealing concept [132].

6 Conclusion

The underlying mechanisms of the electrochemical reactions in SOFCs have not yet been identified unambiguously. Impurities in the raw starting materials could be a reason for the large scatter in the results reported by different groups. This context highlights the need for efficient calibration procedures of SRU and stack models. The approach pursued in the present study consists in using two large existing experimental datasets, gathered on two different segmented setups, for the estimation of the parameters of a physical electrochemical model, the refinement of which is sufficient to support the further implementation of degradation phenomena (Part II of this study [69]).

The agreement between model predictions and measurements is satisfactory in both the cases of a LSM-YSZ and LSCF cathode, over a wide range of operating conditions. This result shows the relevance of the existing models for electrodes made of a MIEC material available from literature [40, 41] for simulations at the SRU scale. The optimal values of the parameters, along with their confidence interval, lie within the ranges reported in literature. This result, as well as the successful statistical tests, ascertains their physical meaning. In the case of internal steam-reforming, a reasonable agreement is achieved, using the empirical kinetic relation from Achenbach and Riensche [33]. Further investigations could not be performed, since the amount of data is insufficient for parameter estimation.

Fits of acceptable quality are achievable, however, with models lacking a solid physical ground. The failure of the attempt to discriminate between model assumptions illustrates the limitations of the information conveyed by polarisation curves. A drastic improvement in the calibration procedure could be obtained from a better interrelation between the experiments and modelling. For instance, the effects of degradation could have been avoided by selecting another sequence of experiments, while the design of the setup can help to reduce uncertainties caused by the averaging of local conditions. Therefore, although a satisfactory fit is not a proof of the physical consistency of a model in the conditions of the present study, additional work, involving design of experiments theories, will be able to assess the real capabilities of the present approach.

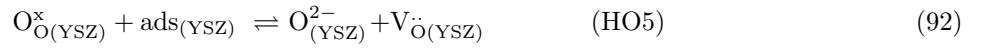
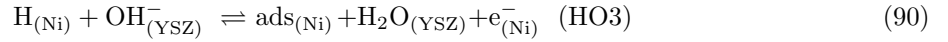
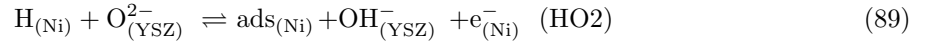
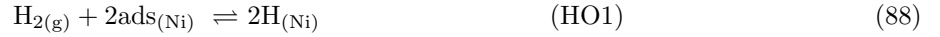
The behaviour of the electrochemical model implemented in a one-dimensional SRU model does not exhibit any significant inconsistencies. The variations in the assumptions of the model do not drastically alter the prediction of the overall performance and local values of the cathode overpotential, which is suspected to govern the degradation of LSM-YSZ cathodes.

Acknowledgements

This work was funded by the Swiss SOFC Consortium, co-financed by the Swiss Federal Office of Energy (SFOE), contract number 152210 and Swisselectric Research. The author would like to thank warmly Nicola Bundschuh for porosimetry measurements on anode supports and Arne Vogel (LBO-EPFL) for his contribution on the parameter estimation, and Shigehisa Kasahara (UNCTAD) for careful reading of the manuscript. gPROMS, a modelling tool from Process System Enterprise (PSE) has been used under academic licensing.

A Appendix

A.1 Hydrogen oxidation



The derivation of Eq.25 is provided here and proceeds in a similar way to Eq.24, which has been described in [93]. The assumption of equilibrium for reactions 88, 91 and 92 yields respectively:

$$\frac{a_{\text{H}_{(\text{Ni})}}^2}{a_{(\text{Ni})}^2 x_{\text{H}_2}} = K_1 \quad (\text{HO1}) \quad (93)$$

$$\frac{a_{(\text{YSZ})} x_{\text{H}_2\text{O}}}{a_{\text{H}_2\text{O}_{(\text{YSZ})}}} = K_4 \quad (\text{HO4}) \quad (94)$$

$$\frac{a_{(\text{YSZ})}}{a_{\text{O}_{(\text{YSZ})}^{2-}}} = K_5 \quad (\text{HO5}) \quad (95)$$

The expressions for hydrogen spillover charge transfer reaction 90 and reaction 89 are

$$\frac{a_{(\text{Ni})} a_{\text{H}_2\text{O}_{(\text{YSZ})}}}{a_{\text{H}_{(\text{Ni})}} a_{\text{OH}_{(\text{YSZ})}^-}} = K_3 \exp\left(\frac{FE}{RT}\right) \quad (90), \text{ as } i = 0 \quad (96)$$

$$j = A_{\text{TPB}} F \left[k_3^a a_{H(\text{Ni})} a_{O_{(\text{YSZ})}^{2-}} \exp\left(\frac{\alpha_3^a FE}{RT}\right) - k_3^c a_{OH_{(\text{YSZ})}^-} a_{(\text{Ni})} \exp\left(-\frac{\alpha_3^c FE}{RT}\right) \right] \quad (89) \quad (97)$$

The first step consists in expressing explicitly the site fractions on the YSZ particle in terms of surface coverage on the anode. The constraint on the YSZ surface is:

$$a_{H_2O_{(\text{YSZ})}} + a_{(\text{YSZ})} + a_{O_{(\text{YSZ})}^{2-}} + a_{OH_{(\text{YSZ})}^-} = 1 \quad (98)$$

The ratios of different site fractions on the YSZ over that of H_2O are:

$$\frac{a_{(\text{YSZ})}}{a_{H_2O_{(\text{YSZ})}}} = \frac{K_4}{x_{H_2O}} \quad (99)$$

$$\frac{a_{O_{(\text{YSZ})}^{2-}}}{a_{H_2O_{(\text{YSZ})}}} = \frac{K_4}{K_5} \frac{1}{x_{H_2O}} \quad (100)$$

$$\frac{a_{OH_{(\text{YSZ})}^-}}{a_{H_2O_{(\text{YSZ})}}} = \frac{a_{(\text{Ni})}}{a_{H(\text{Ni})}} \frac{1}{K_3} \exp\left(-\frac{FE}{RT}\right) \quad (101)$$

These ratios, along with a simple factorisation of Eq.98:

$$a_{H_2O_{(\text{YSZ})}} \left(1 + \frac{a_{(\text{YSZ})}}{a_{H_2O_{(\text{YSZ})}}} + \frac{a_{O_{(\text{YSZ})}^{2-}}}{a_{H_2O_{(\text{YSZ})}}} + \frac{a_{OH_{(\text{YSZ})}^-}}{a_{H_2O_{(\text{YSZ})}}} \right) = 1 \quad (102)$$

enable to determine explicit expressions of the site fractions on the YSZ in terms of surface coverage on the anode:

$$a_{H_2O_{(\text{YSZ})}} = \frac{x_{H_2O}}{x_{H_2O} + K_4 + \frac{K_4}{K_5} + \frac{a_{(\text{Ni})}}{a_{H(\text{Ni})}} \frac{x_{H_2O}}{K_3} \exp\left(-\frac{FE}{RT}\right)} \quad (103)$$

$$a_{(\text{YSZ})} = \frac{K_4}{x_{H_2O} + K_4 + \frac{K_4}{K_5} + \frac{a_{(\text{Ni})}}{a_{H(\text{Ni})}} \frac{x_{H_2O}}{K_3} \exp\left(-\frac{FE}{RT}\right)} \quad (104)$$

$$a_{O_{(\text{YSZ})}^{2-}} = \frac{\frac{K_4}{K_5}}{x_{H_2O} + K_4 + \frac{K_4}{K_5} + \frac{a_{(\text{Ni})}}{a_{H(\text{Ni})}} \frac{x_{H_2O}}{K_3} \exp\left(-\frac{FE}{RT}\right)} \quad (105)$$

$$a_{OH_{(\text{YSZ})}^-} = \frac{\frac{a_{(\text{Ni})}}{a_{H(\text{Ni})}} \frac{x_{H_2O}}{K_3} \exp\left(-\frac{FE}{RT}\right)}{x_{H_2O} + K_4 + \frac{K_4}{K_5} + \frac{a_{(\text{Ni})}}{a_{H(\text{Ni})}} \frac{x_{H_2O}}{K_3} \exp\left(-\frac{FE}{RT}\right)} \quad (106)$$

These expressions can then be inserted in the RDS, Eq.97, reaction 20 (HO2):

$$j = A_{\text{TPB}} F \frac{1}{C} \left[k_3^a a_{H(\text{Ni})} \frac{K_4}{K_5} \exp\left(\frac{\alpha_3^a FE}{RT}\right) - k_3^c \frac{a_{(\text{Ni})}}{a_{H(\text{Ni})}} \frac{x_{H_2O}}{K_3} \exp\left(-\frac{(1 + \alpha_3^a) FE}{RT}\right) \right] \quad (107)$$

where C is the denominator in the expressions of the site fractions on the YSZ surface. Setting $j = 0$ enables the calculation of the equilibrium potential E^{eq} :

$$\frac{FE^{eq}}{RT} = \ln \left(\frac{x_{H_2}}{x_{H_2O}} \frac{K_1 K_2 K_3 K_4}{K_5} \right)^{\frac{1}{2}} \quad (108)$$

Insertion in Eq.107, along with $\eta = E - E^{eq}$ and $a_{H(\text{Ni})}/a_{(\text{Ni})} = K_1^{1/2} x_{H_2}^{1/2}$ yields respectively for the anodic and cathodic branches:

$$a_{(\text{Ni})} \left[k_3^a K_1 x_{H_2} \right]^{1/2} \frac{K_1 K_2 K_3 K_4}{K_5}^{-1/2(1-\alpha_3^a)} \frac{K_4}{K_5} x_{H_2}^{-1/2(1-\alpha_3^a)} x_{H_2O}^{1/2(1-\alpha_3^a)} \exp\left(-\frac{\alpha_3^a FE}{RT}\right) \quad (109)$$

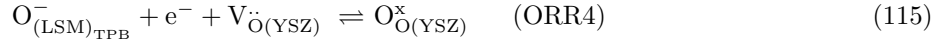
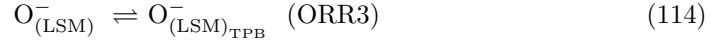
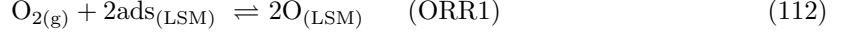
$$a_{(\text{Ni})} \left[k_3^c (K_1 x_{H_2})^{-1/2} \frac{x_{H_2O}}{K_3} \left(\frac{x_{H_2}}{x_{H_2O}} \frac{K_1 K_2 K_3 K_4}{K_5} \right)^{1/2(1+\alpha_3^c)} \exp\left(-\frac{(1 + \alpha_3^c) FE}{RT}\right) \right] \quad (110)$$

Assuming $a_{O_{(\text{YSZ})}^{2-}} \approx 1$, which is qualitatively supported by detailed calculation of Vogler et al. [82] simplifies $C = K_4/K_6$. Further, setting $\alpha = 1/2$ simplifies the identification of apparent reaction and charge-transfer reaction orders:

$$j = i_o^{\text{ct}} \frac{x_{H_2O}^{1/4} (K_1 x_{H_2})^{1/4}}{1 + (K_1 x_{H_2})^{1/2}} \left[\exp\left(\frac{1}{2} \frac{F}{RT} \eta^{\text{ct}}\right) - \exp\left(-\frac{3}{2} \frac{F}{RT} \eta^{\text{ct}}\right) \right] \quad (111)$$

with $\tilde{x}_{H_2} = 1/K_1$ in Eq.24-Eq.26.

A.2 Oxygen reduction



This model, where the second step (ORR2) is rate-limiting has been proposed by van Heuveln et al. [94] and used among others by Kenney et al. [9]. An adaptation is however required for IT-SOFC. The equilibrium of ORR1 yields

$$\frac{x_{\text{O}_2} a_{(\text{LSM})}^2}{a_{\text{O}_{(\text{LSM})}}} = K_1 \quad (116)$$

and enables to express the site fractions on the LSM surface:

$$a_{(\text{LSM})} = \frac{1}{1 + (K_1 x_{\text{O}_2})^{1/2}} \quad (117)$$

$$a_{\text{O}_{(\text{LSM})}} = \frac{(K_1 x_{\text{O}_2})^{1/2}}{1 + (K_1 x_{\text{O}_2})^{1/2}} \quad (118)$$

The equilibrium of ORR3 and ORR4 induces:

$$a_{\text{O}_{(\text{TPB})}^-} = K_4 \frac{1}{1 + (K_1 x_{\text{O}_2})^{1/2}} \exp\left(\frac{FE}{RT}\right) \quad (\text{ORR4}) \quad (119)$$

$$a_{\text{O}_{(\text{LSM})}^-} = K_3 K_4 \frac{1}{1 + (K_1 x_{\text{O}_2})^{1/2}} \exp\left(\frac{FE}{RT}\right) \quad (\text{ORR3}) \quad (120)$$

Insertion in ORR2 and $\alpha = 1/2$ produces:

$$j = A_{\text{TPB}} F \frac{1}{1 + (K_1 x_{\text{O}_2})^{1/2}} \left[k_2^c (K_1 x_{\text{O}_2})^{1/2} \exp\left(-\frac{1}{2} \frac{FE}{RT}\right) - k_2^a K_4 \exp\left(\frac{3}{2} \frac{FE}{RT}\right) \right] \quad (121)$$

Setting $j = 0$ yields the expression of E^{eq} :

$$\frac{FE^{eq}}{RT} = \ln \left[\left(\frac{K_2}{K_4} \right)^{1/2} (K_1 x_{O_2})^{1/2} \right] \quad (122)$$

Finally, insertion in Eq.121 and $\eta = E - E^{eq}$ enables the identification of the apparent reaction order.

$$i_t = i_o^{ct} \frac{(K_1 x_{O_2})^{3/8}}{1 + (K_1 x_{O_2})^{1/2}} \left[\exp \left(-\frac{1}{2} \frac{F\eta}{RT} \right) - \exp \left(\frac{3}{2} \frac{F\eta}{RT} \right) \right] \quad (123)$$

with $\tilde{x}_{O_2} = 1/K_1$ in Eq.50-Eq.52.

References

- [1] N. Autissier, F. Palazzi, F. Marechal, J. Van herle, and D. Favrat. Thermo-economic optimization of a solid oxide fuel cell, gas turbine hybrid system. *Journal of Fuel Cell Science and Technology*, 4(2):123 – 129, 2007.
- [2] D. Larrain, J. Van herle, F. Maréchal, and D. Favrat. Generalized model of planar SOFC repeat element for design optimization. *Journal of Power Sources*, 131(1-2):304 – 312, 2004.
- [3] Christoph Stiller, Bjørn Thorud, Olav Bolland, Rambabu Kandepu, and Lars Imsland. Control strategy for a solid oxide fuel cell and gas turbine hybrid system. *Journal of Power Sources*, 158(1):303 – 315, 2006.
- [4] Fabian Mueller, Robert Gaynor, Allie E. Auld, Jacob Brouwer, Faryar Jabbari, and G. Scott Samuelsen. Synergistic integration of a gas turbine and solid oxide fuel cell for improved transient capability. *Journal of Power Sources*, 176(1):229 – 239, 2008.
- [5] Mahshid Fardadi, Fabian Mueller, and Faryar Jabbari. Feedback control of solid oxide fuel cell spatial temperature variation. *Journal of Power Sources*, 195(13):4222 – 4233, 2010.
- [6] Chih-Kuang Lin, Tsung-Ting Chen, Yau-Pin Chyou, and Lieh-Kwang Chiang. Thermal stress analysis of a planar SOFC stack. *Journal of Power Sources*, 164(1):238 – 251, 2007.

- [7] Arata Nakajo, Zacharie Wuillemin, Jan Van herle, and Daniel Favrat. Simulation of thermal stresses in anode-supported solid oxide fuel cell stacks. Part I: Probability of failure of the cells. *Journal of Power Sources*, 193(1):203 – 215, 2009.
- [8] Arata Nakajo, Zacharie Wuillemin, Jan Van herle, and Daniel Favrat. Simulation of thermal stresses in anode-supported solid oxide fuel cell stacks. Part II: Loss of gas-tightness, electrical contact and thermal buckling. *Journal of Power Sources*, 193(1):216 – 226, 2009.
- [9] Ben Kenney and Kunal Karan. Engineering of microstructure and design of a planar porous composite SOFC cathode: A numerical analysis. *Solid State Ionics*, 178(3-4):297 – 306, 2007.
- [10] L.C.R. Schneider, C.L. Martin, Y. Bultel, D. Bouvard, and E. Siebert. Discrete modelling of the electrochemical performance of SOFC electrodes. *Electrochimica Acta*, 52(1):314 – 324, 2006.
- [11] Jaroslaw Milewski and Konrad Swirski. Modelling the SOFC behaviours by artificial neural network. *International Journal of Hydrogen Energy*, 34(13):5546 – 5553, 2009.
- [12] A. Hagen, R. Barfod, P.V. Hendriksen, Y.L. Liu, and S. Ramousse. Degradation of anode supported SOFCs as a function of temperature and current load. *Journal of The Electrochemical Society*, 153:A1165 – A1171, 2006.
- [13] A. Faes, A. Hessler-Wyser, D. Presvytes, CG Vayenas, and J. Van herle. Nickel-Zirconia Anode Degradation and Triple Phase Boundary Quantification from Microstructural Analysis. *Fuel Cells*, 9(6):841–851, 2009.
- [14] P. Tanasini, M. Cannarozzo, P. Costamagna, A. Faes, J. Van herle, A. Hessler-Wyser, and C. Comninellis. Experimental and Theoretical Investigation of Degradation Mechanisms by Particle Coarsening in SOFC Electrodes. *Fuel Cells*, 9(5):740–752, 2009.
- [15] D. Simwonis, F. Tietz, and D. Stöver. Nickel coarsening in annealed Ni/8YSZ anode substrates for solid oxide fuel cells. *Solid State Ionics*, 132(3-4):241 – 251, 2000.
- [16] A. Mitterdorfer and L. J. Gauckler. $\text{La}_2\text{Zr}_2\text{O}_7$ formation and oxygen reduction kinetics of the $\text{La}_{0.85}\text{Sr}_{0.15}\text{Mn}_y\text{O}_3$, $\text{O}_2(\text{g})/\text{YSZ}$ system. *Solid State Ionics*, 111(3-4):185 – 218, 1998.
- [17] Y.L. Liu, A. Hagen, R. Barfod, M. Chen, H.J. Wang, F.W. Poulsen, and P.V. Hendriksen. Microstructural studies on degradation of interface between LSM-YSZ cathode and YSZ electrolyte in SOFCs. *Solid State Ionics*, 180(23-25):1298 – 1304, 2009.

- [18] M. Chen, YL Liu, A. Hagen, PV Hendriksen, and FW Poulsen. LSM-YSZ Reactions in Different Atmospheres. *Fuel Cells*, 2009.
- [19] YL Liu and C. Jiao. Microstructure degradation of an anode/electrolyte interface in SOFC studied by transmission electron microscopy. *Solid State Ionics*, 176(5-6):435 – 442, 2005.
- [20] M. Hattori, Y. Takeda, Y. Sakaki, A. Nakanishi, S. Ohara, K. Mukai, J.H. Lee, and T. Fukui. Effect of aging on conductivity of yttria stabilized zirconia. *Journal of Power Sources*, 126(1-2):23 – 27, 2004.
- [21] CC Appel, N. Bonanos, A. Horsewell, and S. Linderoth. Ageing behaviour of zirconia stabilised by yttria and manganese oxide. *Journal of Materials Science*, 36(18):4493 – 4501, 2001.
- [22] E. Konyshva, J. Mertens, H. Penkalla, L. Singheiser, and K. Hilpert. Chromium poisoning of the porous composite cathode. *Journal of The Electrochemical Society*, 154(12):B1252 – B1264, 2007.
- [23] Teruhisa Horita, YuePing Xiong, Masashi Yoshinaga, Haruo Kishimoto, Katsuhiko Yamaji, Manuel E. Brito, and Harumi Yokokawa. Determination of Chromium Concentration in Solid Oxide Fuel Cell Cathodes: (La,Sr)MnO₃ and (La,Sr)FeO₃. *Electrochemical and Solid-State Letters*, 12(10):B146 – B149, 2009.
- [24] S. P. Jiang, J. P. Zhang, L. Apateanu, and K. Foger. Deposition of chromium species at Sr-doped LaMnO₃ electrodes in solid oxide fuel cells. I. Mechanism and kinetics. *Journal of The Electrochemical Society*, 147(11):4013 – 4022, 2000.
- [25] S. P. Jiang, J. P. Zhang, and K. Foger. Deposition of chromium species at Sr-doped LaMnO₃ electrodes in Solid Oxide Fuel Cells II. Effect on O₂ reduction reaction. *Journal of The Electrochemical Society*, 147(9):3195 – 3205, 2000.
- [26] S. P. Jiang, J. P. Zhang, and K. Foger. Deposition of chromium species at sr-doped LaMnO₃ electrodes in Solid Oxide Fuel Cells: III. Effect of air flow. *Journal of The Electrochemical Society*, 148(7):C447 – C455, 2001.
- [27] K. Hilpert, D. Das, M. Miller, D. H. Peck, and R. Weiß. Chromium vapor species over solid oxide fuel cell interconnect materials and their potential for degradation processes. *Journal of The Electrochemical Society*, 143(11):3642 – 3647, 1996.

- [28] D. Larrain, J. Van herle, and D. Favrat. Simulation of SOFC stack and repeat elements including interconnect degradation and anode reoxidation risk. *Journal of Power Sources*, 161(1):392 – 403, 2006.
- [29] A. Nakajo, F. Mueller, J. Brouwer, Jan Van herle, and Daniel Favrat. Progressive activation of degradation processes in SOFC stacks. Part I : Lifetime extension by optimisation of the operating conditions. *Manuscript in preparation*.
- [30] A. Nakajo, F. Mueller, J. Brouwer, Jan Van herle, and Daniel Favrat. Progressive activation of degradation processes in SOFC stacks. Part II : Modelling of the spatial distribution of the degradation. *Manuscript in preparation*.
- [31] Fabian Mueller, Faryar Jabbari, Robert Gaynor, and Jacob Brouwer. Novel solid oxide fuel cell system controller for rapid load following. *Journal of Power Sources*, 172(1):308 – 323, 2007.
- [32] J. Van herle, D. Larrain, N. Autissier, Z. Wullemin, M. Molinelli, and D. Favrat. Modeling and experimental validation of solid oxide fuel cell materials and stacks. *Journal of the European Ceramic Society*, 25(12):2627 – 2632, 2005.
- [33] E. Achenbach and E. Riensche. Methane/steam reforming kinetics for solid oxide fuel cells. *Journal of Power Sources*, 52(2):283 – 288, 1994.
- [34] M. A. Khaleel, Z. Lin, P. Singh, W. Surdoval, and D. Collin. A finite element analysis modeling tool for solid oxide fuel cell development: coupled electrochemistry, thermal and flow analysis in MARC®. *Journal of Power Sources*, 130(1-2):136 – 148, 2004.
- [35] P. Aguiar, C.S. Adjiman, and N.P. Brandon. Anode-supported intermediate temperature direct internal reforming solid oxide fuel cell. I: model-based steady-state performance. *Journal of Power Sources*, 138(1-2):120 – 136, 2004.
- [36] P. Aguiar, C.S. Adjiman, and N.P. Brandon. Anode-supported intermediate-temperature direct internal reforming solid oxide fuel cell: II. model-based dynamic performance and control. *Journal of Power Sources*, 147(1-2):136 – 147, 2005.
- [37] S. Campanari and P. Iora. Definition and sensitivity analysis of a finite volume SOFC model for a tubular cell geometry. *Journal of Power Sources*, 132(1-2):113 – 126, 2004.

- [38] Florian P. Nagel, Tilman J. Schildhauer, Serge M.A. Biollaz, and Samuel Stucki. Charge, mass and heat transfer interactions in solid oxide fuel cells operated with different fuel gases—a sensitivity analysis. *Journal of Power Sources*, 184(1):129 – 142, 2008.
- [39] Florian P. Nagel, Tilman J. Schildhauer, Serge M.A. Biollaz, and Alexander Wokaun. Performance comparison of planar, tubular and delta8 solid oxide fuel cells using a generalized finite volume model. *Journal of Power Sources*, 184(1):143 – 164, 2008.
- [40] S. B. Adler, J. A. Lane, and B. C. H. Steele. Electrode kinetics of porous mixed-conducting oxygen electrodes. *Journal of The Electrochemical Society*, 143(11):3554 – 3564, 1996.
- [41] Ann Mari Svensson, Svein Sunde, and Kemal Nişancıoğlu. Mathematical Modeling of Oxygen Exchange and Transport in Air-Perovskite-Yttria-Stabilized Zirconia Interface Regions. *Journal of The Electrochemical Society*, 145(4):1390 – 1400, 1998.
- [42] J. Fleig and J. Maier. The polarization of mixed conducting SOFC cathodes: Effects of surface reaction coefficient, ionic conductivity and geometry. *Journal of the European Ceramic Society*, 24(6):1343 – 1347, 2004.
- [43] J. Fleig. On the width of the electrochemically active region in mixed conducting solid oxide fuel cell cathodes. *Journal of Power Sources*, 105(2):228 – 238, 2002.
- [44] Gregory W. Coffey, Larry R. Pederson, and Peter C. Rieke. Competition between bulk and surface pathways in mixed ionic electronic conducting oxygen electrodes. *Journal of The Electrochemical Society*, 150(8):A1139 – A1151, 2003.
- [45] S. H. Chan, X. J. Chen, and K. A. Khor. Cathode micromodel of solid oxide fuel cell. *Journal of The Electrochemical Society*, 151(1):A164 – A172, 2004.
- [46] D. Bouvard and F.F. Lange. Relation between percolation and particle coordination in binary powder mixtures. *Acta Metallurgica et Materialia*, 39(12):3083 – 3090, 1991.
- [47] Daifen Chen, Zijing Lin, Huayang Zhu, and Robert J. Kee. Percolation theory to predict effective properties of solid oxide fuel-cell composite electrodes. *Journal of Power Sources*, 191(2):240 – 252, 2009.
- [48] Jr. John R. Izzo, Abhijit S. Joshi, Kyle N. Grew, Wilson K. S. Chiu, Andrei Tkachuk, Siew H. Wang, and Wenbing Yun. Nondestructive Reconstruction and Analysis of SOFC Anodes Using X-ray

- Computed Tomography at Sub-50 nm Resolution. *Journal of The Electrochemical Society*, 155(5):B504 – B508, 2008.
- [49] Abhijit S. Joshi, Kyle N. Grew, Aldo A. Peracchio, and Wilson K.S. Chiu. Lattice Boltzmann modeling of 2D gas transport in a solid oxide fuel cell anode. *Journal of Power Sources*, 164(2):631 – 638, 2007.
- [50] Paola Costamagna, Paolo Costa, and Vincenzo Antonucci. Micro-modelling of solid oxide fuel cell electrodes. *Electrochimica Acta*, 43(3-4):375 – 394, 1998.
- [51] Robert J. Kee, Huayang Zhu, and David G. Goodwin. Solid-oxide fuel cells with hydrocarbon fuels. *Proceedings of the Combustion Institute*, 30(2):2379 – 2404, 2005.
- [52] Wolfgang G. Bessler, Jürgen Warnatz, and David G. Goodwin. The influence of equilibrium potential on the hydrogen oxidation kinetics of SOFC anodes. *Solid State Ionics*, 177(39-40):3371 – 3383, 2007.
- [53] G. Schiller, W.G. Bessler, K.A. Friedrich, S. Gewies, and C. Willich. Spatially resolved electrochemical performance in a segmented planar SOFC. *ECS Transactions*, 17(1):79–87, 2009.
- [54] P. Metzger, Friedrich K.A., G. Schiller, and C. Willich. Spatially resolved measuring technique for solid oxide fuel cells. *Journal of Fuel Cell Science and Technology*, 6:021304–1 – 021304–4, 2009.
- [55] W.G. Bessler, S. Gewies, C. Willich, G. Schiller, and K.A. Friedrich. Spatial distribution of electrochemical performance in a segmented SOFC: A combined modeling and experimental study. *Fuel Cells*, 10(3):411–418, 2010.
- [56] Huayang Zhu and Robert J. Kee. A general mathematical model for analyzing the performance of fuel-cell membrane-electrode assemblies. *Journal of Power Sources*, 117(1-2):61 – 74, 2003.
- [57] R. Suwanwarangkul, E. Croiset, M. W. Fowler, P. L. Douglas, E. Entchev, and M. A. Douglas. Performance comparison of Fick’s, dusty-gas and Stefan-Maxwell models to predict the concentration overpotential of a SOFC anode. *Journal of Power Sources*, 122(1):9 – 18, 2003.
- [58] Fatma N. Cayan, Suryanarayana R. Pakalapati, Francisco Elizalde-Blancas, and Ismail Celik. On modeling multi-component diffusion inside the porous anode of solid oxide fuel cells using Fick’s model. *Journal of Power Sources*, 192(2):467 – 474, 2009.
- [59] Vinod M. Janardhanan, Vincent Heuveline, and Olaf Deutschmann. Performance analysis of a SOFC under direct internal reforming conditions. *Journal of Power Sources*, 172(1):296 – 307, 2007.

- [60] Think X. Ho, Pawel Kosinski, Alex C. Hoffmann, and Arild Vik. Numerical analysis of a planar anode-supported SOFC with composite electrodes. *International Journal of Hydrogen Energy*, 34(8):3488 – 3499, 2009.
- [61] A. Chaisantikulwat, C. Diaz-Goano, and E.S. Meadows. Dynamic modelling and control of planar anode-supported solid oxide fuel cell. *Computers Chemical Engineering*, 32(10):2365 – 2381, 2008.
- [62] Graham M. Goldin, Huayang Zhu, Robert J. Kee, David Bierschenk, and Scott A. Barnett. Multidimensional flow, thermal, and chemical behavior in solid-oxide fuel cell button cells. *Journal of Power Sources*, 187(1):123 – 135, 2009.
- [63] Vinod M. Janardhanan and Olaf Deutschmann. CFD analysis of a solid oxide fuel cell with internal reforming: Coupled interactions of transport, heterogeneous catalysis and electrochemical processes. *Journal of Power Sources*, 162(2):1192 – 1202, 2006.
- [64] Gaia Franceschini and Sandro Macchietto. Model-based design of experiments for parameter precision: State of the art. *Chemical Engineering Science*, 63(19):4846 – 4872, 2008.
- [65] gPROMS (General Process Modelling and Simulation Tool), v3.2, Process Systems Enterprise Ltd., London.
- [66] P. Metzger, K.-A. Friedrich, H. Müller-Steinhagen, and G. Schiller. SOFC characteristics along the flow path. *Solid State Ionics*, 177(19-25):2045 – 2051, 2006.
- [67] Zacharie Wuillemin. *Experimental and modeling investigations on local performance and local degradation in solid oxide fuel cells*. PhD thesis, Lausanne, 2009.
- [68] Frédéric Ravussin, Jan Van herle, Nordahl Autissier, Michele Molinelli, Diego Larrain, and Daniel Favrat. Local current measurement in a solid oxide fuel cell repeat element. *Journal of the European Ceramic Society*, 27(2-3):1035–1040, 2007.
- [69] A. Nakajo, P. Tanasini, Jan Van herle, and Daniel Favrat. Electrochemical model of solid oxide fuel cell for simulation at the stack scale. Part II: Implementation of degradation processes. *Manuscript submitted to the Journal of The Electrochemical Society*.
- [70] Zacharie Wuillemin, Arata Nakajo, Andres Müller, Andreas J. Schuler, Stefan Diethelm, Jan Van Herle, and Daniel Favrat. Locally-Resolved Study of Degradation in a SOFC Repeat-Element. *ECS Transactions*, 25(2):457 – 466, 2009.

- [71] F.P. Incropera, D.P. DeWitt, T.L. Bergman, and A.S. Lavine. Fundamentals of heat and mass transfer. 1996.
- [72] Christoph Stiller, Bjørn Thorud, Steinar Seljebø, Øistein Mathisen, Håvard Karoliussen, and Olav Bolland. Finite-volume modeling and hybrid-cycle performance of planar and tubular solid oxide fuel cells. *Journal of Power Sources*, 141(2):227 – 240, 2005.
- [73] B. Todd and J. B. Young. Thermodynamic and transport properties of gases for use in solid oxide fuel cell modelling. *Journal of Power Sources*, 110(1):186 – 200, 2002.
- [74] Kemal Nisancioglu. Ohmic losses. *Proceedings of the IEA workshop on mathematical modelling. Charmey*, pages 87 – 98, 1998.
- [75] Jeffrey W. Fergus. Electrolytes for solid oxide fuel cells. *Journal of Power Sources*, 162(1):30 – 40, 2006.
- [76] A. Atkinson. Chemically-induced stresses in gadolinium-doped ceria solid oxide fuel cell electrolytes. *Solid State Ionics*, 95(3-4):249 – 258, 1997.
- [77] Andreas Mai, Vincent A.C. Haanappel, Sven Uhlenbruck, Frank Tietz, and Detlev Stöver. Ferrite-based perovskites as cathode materials for anode-supported solid oxide fuel cells: Part I. Variation of composition. *Solid State Ionics*, 176(15-16):1341 – 1350, 2005.
- [78] J. Fleig, H.L. Tuller, and J. Maier. Electrodes and electrolytes in micro-SOFCs: a discussion of geometrical constraints. *Solid State Ionics*, 174(1-4):261 – 270, 2004.
- [79] A. Bieberle, L. P. Meier, and L. J. Gauckler. The electrochemistry of Ni pattern anodes used as solid oxide fuel cell model electrodes. *Journal of The Electrochemical Society*, 148(6):A646 – A656, 2001.
- [80] Junichiro Mizusaki, Hiroaki Tagawa, Takatoshi Saito, Tamaki Yamamura, Kouji Kamitani, Katsuhiko Hirano, Shaw Ehara, Toshinori Takagi, Tomoji Hikita, Masamichi Ippommatsu, Shigeto Nakagawa, and Keiichi Hashimoto. Kinetic studies of the reaction at the nickel pattern electrode on YSZ in $H_2 - H_2O$ atmospheres. *Solid State Ionics*, 70-71(Part 1):52 – 58, 1994.
- [81] B. de Boer. *SOFC Anode-hydrogen oxidation at porous nickel and nickel/yttria-stabilised zirconia cermet electrodes, 1998*. PhD thesis, Ph. D. Thesis, University of Twente, Enschede, The Netherlands.

- [82] Marcel Vogler, Anja Bieberle-Hütter, Ludwig Gauckler, Jürgen Warnatz, and Wolfgang G. Bessler. Modelling Study of Surface Reactions, Diffusion, and Spillover at a Ni/YSZ Patterned Anode. *Journal of The Electrochemical Society*, 156(5):B663 – B672, 2009.
- [83] A. Bieberle and L. J. Gauckler. Reaction mechanism of Ni pattern anodes for solid oxide fuel cells. *Solid State Ionics*, 135(1-4):337 – 345, 2000.
- [84] M. Brown, S. Primdahl, and M. Mogensen. Structure/performance relations for Ni/Yttria-Stabilized Zirconia anodes for solid oxide fuel cells. *Journal of The Electrochemical Society*, 147(2):475 – 485, 2000.
- [85] Xiaoge Wang, Nobuyoshi Nakagawa, and Kunio Kato. Anodic polarization related to the ionic conductivity of zirconia at Ni-Zirconia/Zirconia electrodes. *Journal of The Electrochemical Society*, 148(6):A565 – A569, 2001.
- [86] S. Primdahl and M. Mogensen. Durability and thermal cycling of Ni/YSZ cermet anodes for solid oxide fuel cells. *Journal of Applied Electrochemistry*, 30(2):247 – 257, 2000.
- [87] S. P. Jiang and Y. Ramprakash. H₂ oxidation on Ni/Y-TZP cermet electrodes - polarisation behaviour. *Solid State Ionics*, 116(1-2):145 – 156, 1999.
- [88] S. P. Jiang and Y. Ramprakash. H₂ oxidation on Ni/Y-TZP cermet electrodes - a comparison of electrode behaviour by GCI and EIS techniques. *Solid State Ionics*, 122(1-4):211 – 222, 1999.
- [89] P. Holtappels, L. G. J. de Haart, and U. Stimming. Reaction of hydrogen/water mixtures on nickel-zirconia cermet electrodes: I. DC Polarization characteristics. *Journal of The Electrochemical Society*, 146(5):1620 – 1625, 1999.
- [90] P. Holtappels, I. C. Vinke, L. G. J. de Haart, and U. Stimming. Reaction of hydrogen/water mixtures on nickel-zirconia cermet electrodes: II. AC Polarization characteristics. *Journal of The Electrochemical Society*, 146(8):2976 – 2982, 1999.
- [91] Y. L. Liu, S. Primdahl, and M. Mogensen. Effects of impurities on microstructure in Ni/YSZ-YSZ half-cells for SOFC. *Solid State Ionics*, 161(1-2):1 – 10, 2003.
- [92] A. Bieberle and L. J. Gauckler. State-space modeling of the anodic SOFC system Ni, H₂-H₂O|YSZ. *Solid State Ionics*, 146(1-2):23 – 41, 2002.

- [93] Huayang Zhu, Robert J. Kee, Vinod M. Janardhanan, Olaf Deutschmann, and David G. Goodwin. Modeling elementary heterogeneous chemistry and electrochemistry in solid-oxide fuel cells. *Journal of The Electrochemical Society*, 152(12):A2427 – A2440, 2005.
- [94] F. H. van Heuveln and H. J. M. Bouwmeester. Electrode Properties of Sr-Doped LaMnO₃ on Yttria-Stabilized Zirconia. *Journal of The Electrochemical Society*, 144(1):134 – 140, 1997.
- [95] R. Vaßen, D. Simwonis, and D. Stöver. Modelling of the agglomeration of Ni-particles in anodes of solid oxide fuel cells. *Journal of Materials Science*, 36(1):147 – 151, 2001.
- [96] Junya Kondoh, Tsuyoshi Kawashima, Shiomi Kikuchi, Yoichi Tomii, and Yasuhiko Ito. Effect of aging on yttria-stabilized zirconia. 1: A study of its electrochemical properties. *Journal of The Electrochemical Society*, 145(5):1527 – 1536, 1998.
- [97] Junya Kondoh, Shiomi Kikuchi, Yoichi Tomii, and Yasuhiko Ito. Effect of aging on yttria-stabilized zirconia. 2: A study of the effect of the microstructures on conductivity. *Journal of The Electrochemical Society*, 145(5):1536 – 1550, 1998.
- [98] Junya Kondoh, Shiomi Kikuchi, Yoichi Tomii, and Yasuhiko Ito. Effect of aging on yttria-stabilized zirconia. *Journal of The Electrochemical Society*, 145(5):1550 – 1560, 1998.
- [99] G. Franceschini and S. Macchietto. Validation of a model for biodiesel production through model-based experiment design. *Ind. Eng. Chem. Res*, 46(1):220 – 232, 2007.
- [100] R. Krishna and J. A. Wesselingh. The Maxwell-Stefan approach to mass transfer. *Chemical Engineering Science*, 52(6):861 – 911, 1997.
- [101] Ethan S. Hecht, Gaurav K. Gupta, Huayang Zhu, Anthony M. Dean, Robert J. Kee, Luba Maier, and Olaf Deutschmann. Methane reforming kinetics within a Ni-YSZ SOFC anode support. *Applied Catalysis A: General*, 295(1):40 – 51, 2005.
- [102] R. Leinfelder. Reaktionskinetische Untersuchungen zur Methan-Dampf-Reformierung und Shift-Reaktion an Anoden oxidkeramischer Brennstoffzellen. *Universität Erlangen-Nürnberg, Erlangen-Nürnberg, Germany*, 2004.
- [103] Khaliq Ahmed and Karl Foger. Kinetics of internal steam reforming of methane on Ni/YSZ-based anodes for solid oxide fuel cells. *Catalysis Today*, 63(2-4):479 – 487, 2000.

- [104] S.B. Adler. Factors Governing Oxygen Reduction in Solid Oxide Fuel Cell Cathodes. *Chem. Rev.*, 104(10):4791 – 4844, 2004.
- [105] Q. Xu, D. Huang, F. Zhang, W. Chen, M. Chen, and H. Liu. Structure, electrical conducting and thermal expansion properties of $\text{La}_{0.6}\text{Sr}_{0.4}\text{Co}_{0.8}\text{Fe}_{0.2}\text{O}_{3-\delta}\text{-Ce}_{0.8}\text{Sm}_{0.2}\text{O}_{2-\delta}$ composite cathodes. *Journal of Alloys and Compounds*, 454(1-2):460 – 465, 2008.
- [106] T. Kawada, J. Suzuki, M. Sase, A. Kaimai, K. Yashiro, Y. Nigara, J. Mizusaki, K. Kawamura, and H. Yugami. Determination of oxygen vacancy concentration in a thin film of $\text{La}_{0.6}\text{Sr}_{0.4}\text{CoO}_{3-\delta}$ by an electrochemical method. *Journal of The Electrochemical Society*, 149(7):E252 – E259, 2002.
- [107] T. Kawada, K. Masuda, J. Suzuki, A. Kaimai, K. Kawamura, Y. Nigara, J. Mizusaki, H. Yugami, H. Arashi, N. Sakai, and H. Yokokawa. Oxygen isotope exchange with a dense $\text{La}_{0.6}\text{Sr}_{0.4}\text{CoO}_{3-\delta}$ electrode on a $\text{Ce}_{0.9}\text{Ca}_{0.1}\text{O}_{1.9}$ electrolyte. *Solid State Ionics*, 121(1-4):271 – 279, 1999.
- [108] S. B. Adler. Mechanism and kinetics of oxygen reduction on porous $\text{La}_{1-x}\text{Sr}_x\text{CoO}_{3-\delta}$ electrodes. *Solid State Ionics*, 111(1-2):125 – 134, 1998.
- [109] Teruhisa Horita, Katsuhiko Yamaji, Masahiko Ishikawa, Natsuko Sakai, Harumi Yokokawa, Tatsuya Kawada, and Tohru Kato. Active sites imaging for oxygen reduction at the $\text{La}_{0.9}\text{Sr}_{0.1}\text{MnO}_{3-x}$ /yttria-stabilized zirconia interface by secondary-ion mass spectrometry. *Journal of The Electrochemical Society*, 145(9):3196 – 3202, 1998.
- [110] E. Siebert, A. Hammouche, and M. Kleitz. Impedance spectroscopy analysis of $\text{La}_{1-x}\text{Sr}_x\text{MnO}_3$ -yttria-stabilized zirconia electrode kinetics. *Electrochimica Acta*, 40(11):1741 – 1753, 1995.
- [111] Erica Perry Murray, Tsepin Tsai, and Scott A. Barnett. Oxygen transfer processes in $(\text{La},\text{Sr})\text{MnO}_3/\text{Y}_2\text{O}_3$ -stabilized ZrO_2 cathodes: an impedance spectroscopy study. *Solid State Ionics*, 110(3-4):235 – 243, 1998.
- [112] M. J. Jørgensen and M. Mogensen. Impedance of solid oxide fuel cell LSM/YSZ composite cathodes. *Journal of The Electrochemical Society*, 148(5):A433 – A442, 2001.
- [113] S. P. Jiang and W. Wang. Effect of polarization on the interface between $(\text{La},\text{Sr})\text{MnO}_3$ electrode and $\text{Y}_2\text{O}_3 - \text{ZrO}_2$ electrolyte. *Electrochemical and Solid-State Letters*, 8(2):A115 – A118, 2005.

- [114] Majid Mosleh, Martin Søgaaard, and Peter Vang Hendriksen. Kinetics and mechanisms of oxygen surface exchange on $\text{La}_{0.6}\text{Sr}_{0.4}\text{FeO}_{3-\delta}$ thin films. *Journal of The Electrochemical Society*, 156(4):B441 – B457, 2009.
- [115] Martin Søgaaard, Peter Vang Hendriksen, and Mogens Mogensen. Oxygen nonstoichiometry and transport properties of strontium substituted lanthanum ferrite. *Journal of Solid State Chemistry*, 180(4):1489 – 1503, 2007.
- [116] Junichiro Mizusaki, Masafumi Yoshihiro, Shigeru Yamauchi, and Kazuo Fueki. Nonstoichiometry and defect structure of the perovskite-type oxides $\text{La}_{1-x}\text{Sr}_x\text{FeO}_3$. *Journal of Solid State Chemistry*, 58(2):257 – 266, 1985.
- [117] J. E. ten Elshof, M. H. R. Lankhorst, and H. J. M. Bouwmeester. Oxygen exchange and diffusion coefficients of strontium-doped lanthanum ferrites by electrical conductivity relaxation. *Journal of The Electrochemical Society*, 144(3):1060 – 1067, 1997.
- [118] M. H. R. Lankhorst and J. E. ten Elshof. Thermodynamic quantities and defect structure of $\text{La}_{0.6}\text{Sr}_{0.4}\text{Co}_{1-y}\text{Fe}_y\text{O}_{3-\delta}$ ($y=0-0.6$) from high-temperature coulometric titration experiments. *Journal of Solid State Chemistry*, 130(2):302 – 310, 1997.
- [119] HJM Bouwmeester, MW Den Otter, and BA Boukamp. Oxygen transport in $\text{La}_{0.6}\text{Sr}_{0.4}\text{Co}_{1-y}\text{Fe}_y\text{O}_{3-\delta}$. *Journal of Solid State Electrochemistry*, 8(9):599 – 605, 2004.
- [120] J. E. ten Elshof, M. H. R. Lankhorst, and H. J. M. Bouwmeester. Chemical diffusion and oxygen exchange of $\text{La}_{0.6}\text{Sr}_{0.4}\text{Co}_{0.6}\text{Fe}_{0.4}\text{O}_{3-\delta}$. *Solid State Ionics*, 99(1-2):15 – 22, 1997.
- [121] Dionissios Mantzavinos, Anne Hartley, Ian S. Metcalfe, and Mortaza Sahibzada. Oxygen stoichiometries in $\text{La}_{1-x}\text{Sr}_x\text{Co}_{1-y}\text{Fe}_y\text{O}_{3-\delta}$ perovskites at reduced oxygen partial pressures. *Solid State Ionics*, 134(1-2):103 – 109, 2000.
- [122] S.B. Adler, X.Y. Chen, and J.R. Wilson. Mechanisms and rate laws for oxygen exchange on mixed-conducting oxide surfaces. *Journal of Catalysis*, 245(1):91 – 109, 2007.
- [123] X. J. Chen, S. H. Chan, and K. A. Khor. Simulation of a composite cathode in solid oxide fuel cells. *Electrochimica Acta*, 49(11):1851 – 1861, 2004.

- [124] Yi Jiang, Shizhong Wang, Yahong Zhang, Jingwang Yan, and Wenzhao Li. Electrochemical reduction of oxygen on a strontium doped lanthanum manganite electrode. *Solid State Ionics*, 110(1-2):111 – 119, 1998.
- [125] Ann Mari Svensson, Svein Sunde, and Kemal Nisancioglu. Mathematical Modeling of Oxygen Exchange and Transport in Air-Perovskite-YSZ Interface Regions. *Journal of The Electrochemical Society*, 144(8):2719 – 2732, 1997.
- [126] J.S. Newman and K.E. Thomas-Alyea. *Electrochemical systems, p289-291*. Wiley-Interscience, 2004.
- [127] Zhaohui Yang and Y. S. Lin. A semi-empirical equation for oxygen nonstoichiometry of perovskite-type ceramics. *Solid State Ionics*, 150(3-4):245 – 254, 2002.
- [128] Yoshio Matsuzaki and Isamu Yasuda. Relationship between the steady-state polarization of the SOFC air electrode, $\text{La}_{0.6}\text{Sr}_{0.4}\text{MnO}_{3+\delta}/\text{YSZ}$, and its complex impedance measured at the equilibrium potential. *Solid State Ionics*, 126(3-4):307 – 313, 1999.
- [129] D. Gostovic, J. R. Smith, D. P. Kundinger, K. S. Jones, and E. D. Wachsman. Three-dimensional reconstruction of porous lscf cathodes. *Electrochemical and Solid-State Letters*, 10(12):B214 – B217, 2007.
- [130] LGJ de Haart, J. Mougín, O. Posdziech, J. Kiviaho, and NH Menzler. Stack Degradation in Dependence of Operation Parameters; the Real-SOFC Sensitivity Analysis. *Fuel Cells*, 9(6):794 – 804, 2009.
- [131] A. Hagen, Y. L. Liu, R. Barfod, and P. V. Hendriksen. Assessment of the cathode contribution to the degradation of anode-supported solid oxide fuel cells. *Journal of The Electrochemical Society*, 155(10):B1047 – B1052, 2008.
- [132] Zacharie Wuillemin, Nordahl Autissier, Arata Nakajo, Minh-Tam Luong, Jan Van herle, and Daniel Favrat. Modeling and Study of the Influence of Sealing on a Solid Oxide Fuel Cell. *Journal of Fuel Cell Science and Technology*, 5(1):011016 – 9, 2008.
- [133] CM Kleinlogel and LJ Gauckler. Mixed electronic-ionic conductivity of cobalt doped cerium gadolinium oxide. *Journal of Electroceramics*, 5(3):231 – 243, 2000.
- [134] Sutin Kuharuangrong. Effects of Ni on the electrical conductivity and microstructure of $\text{La}_{0.82}\text{Sr}_{0.16}\text{MnO}_3$. *Ceramics International*, 30(2):273 – 277, 2004.

- [135] K.T.S. Thydén. *Microstructural degradation of Ni-YSZ anodes for solid oxide fuel cells*. PhD thesis, Technical University of Denmark, Risø National Laboratory for Sustainable Energy, Fuel Cells and Solid State Chemistry Division.
- [136] D. Simwonis. Optimierung der Anoden der Hochtemperatur-Brennstoffzelle durch Korrelation von Herstellungsverfahren, Gefüge und Eigenschaften; Jül-report 3678. *Edited by Forschungszentrum Jülich, Germany, 1999.*

List of Figures

- 1 (a) Description of the domains and boundaries in the 1D model. The cell layers are merged in \mathcal{R}_{3-5} , which is detailed in Fig.
- 2 Representation of the MEA of a SOFC, along with the denomination of the domains and interfaces. Case of a LSM-YSZ cathode.
- 3 Equivalent circuit of the one-dimensional electrochemical model. 60
- 4 Comparison between experimental (gray dots) [118, 119] and implemented (black dots) properties of a LSCF material, as compared to the literature.
- 5 IV characteristics measured with the DLR setup (LSCF cathode), for different gas flows and inlet molar fractions of hydrogen and methane.
- 6 Comparison between experimental (lines) and simulated (squares) IV characteristics for various conditions. DLR data. HO2 as oxidant.
- 7 Comparison between measured and simulated IV characteristics of experiments not included in the parameter estimations. DLR data. HO2 as oxidant.
- 8 Distribution of the hydrogen (ribbons) and methane molar fractions in the anode, along the flow path, as predicted with the model.
- 9 Comparison between experimental (squares) and simulated (lines) IV characteristics used for the calibration of the LSM-YSZ cathode.
- 10 IV characteristics of SRUs embedded in a stack, for different flow configurations and cathode materials. Curve series corresponding to the different cathode materials.
- 11 Contributions of the cathode to the ASR and Nernst potential, along with mass transfer resistance, during an IV characteristic.
- 12 Top: distribution of the overpotential due to electrochemical processes on the cathode and anode side, and current density. Bottom: distribution of the overpotential due to mass transfer processes.
- 13 Profile of the vacancy concentration in the LSCF cathode, depending on the flow configuration. The fuel utilisation is 0.8, corresponding to the maximum current density.

Figure 1: (a) Description of the domains and boundaries in the 1D model. The cell layers are merged in \mathcal{R}_{3-5} , which is detailed in Figure 2. (b) In-plane arrangement of the segments in the DLR setup and (c) view of the FlameSOFC SRU design, along with the location of the segments in the LENI-EPFL setup.

Figure 2: Representation of the MEA of a SOFC, along with the denomination of the domains and interfaces. Case of a LSM-YSZ cathode.

Figure 3: Equivalent circuit of the one-dimensional electrochemical model.

Figure 4: Comparison between experimental (gray dots) [118, 119] and implemented (black dots) properties of a LSCF material, as computed by Eq.69 (top) and Eq.70 (bottom).

Figure 5: IV characteristics measured with the DLR setup (LSCF cathode), for different gas flows and inlet molar fractions of hydrogen, from 10% to 50%, at 1073 K (see Table 2). The indications refer to the inlet conditions in the SRU. Standard conditions: air 80 nmlpm cm^{-2} , fuel 3% humidified $\text{H}_2:\text{N}_2$ 50:50. The curves appear in pairs, corresponding to the 2 central segment rows.

Figure 6: Comparison between experimental (lines) and simulated (squares) IV characteristics for various conditions. DLR data. HO2 anode model, calibrated on data corrected for the degradation.

Figure 7: Comparison between measured and simulated IV characteristics of experiments not included in the parameter estimations. DLR data. The correction for the degradation is shown for the standard conditions. The experiments including internal steam-methane reforming (SMR insert) are simulated with the HO2 model and the kinetic relation from Achenbach et al. [33].

Figure 8: Distribution of the hydrogen (ribbons) and methane molar fractions in the anode, along the flow path, as predicted with the HO2 model, coupled to the relation for steam-methane reforming from Achenbach et al. [33]. The operating point is that of highest current density in Figure 7. Color online.

Figure 9: Comparison between experimental (squares) and simulated (lines) IV characteristics used for the calibration of the LSM-YSZ model.

Figure 10: IV characteristics of SRUs embedded in a stack, for different flow configurations and cathode materials. Curve series correspond to the three anode models. Color online.

Figure 11: Contributions of the cathode to the ASR and Nernst potential, along with mass transfer resistance, during an IV characterisation of a SRU embedded in a stack. Color online.

Figure 12: Top: distribution of the overpotential due to electrochemical processes on the cathode and anode side, and current density. Bottom: distribution of the Nernst potential, including diffusion, and temperature over $\mathcal{R}_{\text{area}}$. Case of a LSM-YSZ cathode. The fuel utilisation is of 0.8, corresponding to 0.405 Acm^{-2} . The temperature difference is of 152 K and 116 K in co- (black) and counter flow (gray), respectively.

Figure 13: Profile of the vacancy concentration in the LSCF cathode, depending on the flow configuration. The fuel utilisation is 0.8, corresponding to 0.405 Acm^{-2} . The temperature difference is 152 K and 116 K in co-flow and counter flow, respectively.

List of Tables

1	Domain of validity for the parameters proposed by Achenbach and Riensche [33] and Leinfelder et al. [102]	72
2	Range of operating conditions included in the parameter estimations.	73
3	Operating conditions for the SRU simulations.	74
4	Values of the fixed parameters and allowable range of the fitted parameters.	75
5	Results of the parameter estimations with the DLR data, LSCF cathode. Inside brackets are the 90% confidence interval and	
6	Results of the parameter estimation performed on the experimental data from the LENI-EPFL setup (LSM-YSZ). Inside brackets are the 90% confidence interval and	

Parameter	Achenbach et al. [33]	Leinfelder et al. [102]
T [K]	1073-1273	884-973
SCR [-]	3 - 8	2
p [Pa]	$1.1 \cdot 10^5 - 2.8 \cdot 10^5$	$1.1 \cdot 10^5$
h_{an} [μm]	1400	25
n [-]	0.4	0.3

Table 1: Domain of validity for the parameters proposed by Achenbach and Riensche [33] and Leinfelder et al. [102]

	DLR setup	LENI-EPFL setup
Operating time [h]	75-400	15-23
Furnace temperature [K]	973-1073	1057-1062
Air inlet temperature [K]	973-1073 ^a	1043
E [V]	0.575-1.07	0.7-1.05
$j_{u_{max}}$ [A cm ⁻²]	1.2	0.7
Air flow [nmlpm cm ⁻²]	20-80	9.62 ^c
Fuel flow [nmlpm cm ⁻²]	6.25-25	7.3-11.0
Anode inlet molar fractions		
H ₂	0.1-0.97	0.5-0.97
H ₂ O	0-0.03	0.03
N ₂	0-0.9	0-0.5
CH ₄	0.02-0.1 ^b	0
Cathode inlet molar fraction		
O ₂	0.05-0.5	0.21

^a Assumed identical to the furnace temperature

^b Not included in parameter estimation

^c Air ratio

Table 2: Range of operating conditions included in the parameter estimations.

Air inlet temperature [K]	973
Fuel inlet temperature [K]	973
Fuel flow [nmlpm cm ⁻²]	3.6
Air ratio	5-7.5 ^a
Inlet molar fractions	
H ₂	0.263
H ₂ O	0.493
CH ₄	0.171
CO	0.029
CO ₂	0.044

^a Value coarsely adjusted to yield a similar maximum temperature of 1100 K at FU=0.8, in co-flow, respectively counter-flow

Table 3: Operating conditions for the SRU simulations.

Conductivities							
	8YSZ	20GDC	LSM	Ni	MIC, air	MIC, fuel	
$k_{o_{ion}}$	7.92e8 [9]	$7.04e4 \cdot T_s$ [133]	-	-	-	-	-
$E_{a_{ion}}$ [kJ mol ⁻¹]	110.0 [9]	21.9 [133]	-	-	-	-	-
$k_{o_{el}}$	50.0 ^a	-	$10700 \cdot T_s$ [134]	60000 [135]	45.8 [69]	120.5 [69]	
$E_{a_{el}}$ [kJ mol ⁻¹]	-	-	12.9 [134]	-	33.3 [69]	45.3 [69]	
Electrochemical processes							
	k_o^{ct} [A cm ⁻²]	E_a^{ct} [kJ mol ⁻¹]	\tilde{k}_o^{ct} [atm]	\tilde{E}_a^{ct} [kJ mol ⁻¹]	$r_{an_1}^{ct}$	$r_{an_2}^{ct}$	r_{cath}^{ct}
anode (HO2)	0.05-100 ^b	60-190 ^b	2.136 [51]	96 [51]	1/4 ^c	1/4 ^c	-
anode (HO3)	0.05-100 ^b	60-190 ^b	2.136 [51]	96 [51]	1/4 ^c	3/4 ^c	-
anode (EMP)	0.05-100 ^b	60-190 ^b	2.136 [51]	96 [51]	0-0.5 ^b	^b	-
cathode	0.001-20 ^b	80-290 ^b	3.33e9 [128]	186 [128]	-	-	3/8 ^c
cathode	0.001-20 ^b	80-290 ^b	4.9e8 [124]	200 [124]	-	-	3/8 ^c
Chemical reactions in porous media							
	τ^2	n	d_n	$k_{o_{an}}^{SMR}/h_{an}$	$E_{a_{an}}^{SMR}$ [kJ mol ⁻¹]	$r_{an_1}^{SMR}$	$r_{an_2}^{SMR}$
anode	6-14 ^b	0.31 ^d	6.98e-7 ^d	0.053 [33]	82 [33]	1	0
anode	6-14 ^b	0.31 ^d	6.98e-7 ^d	32.255 [102]	205 [102]	1	1
cathode	3 ^e	0.42 [14]	4.4e-7 [14]	-	-	-	-
Electrode morphology							
	ϕ_{el}	ϕ_{ion}	r_{el}	r_{ion}	τ_s	l_g	d_g
anode	0.4 [136]	0.6 [136]	6.25e-7 [136]	5.75e-7 [136]	-	9e-7 [17]	1e-7 [17]
cathode	0.49	0.51	2.25e-7 [14]	1.75e-7 [14]	3 ^f	9e-7 [17]	1e-7 [17]
MIEC surface properties							
	A_{MIEC} [cm ⁻¹]	C_{K_1}	C_{K_2}	C_{K_3}	E_{a_K} [kJ mol ⁻¹]		
LSCF	20000 [40]	1.805 [119]	2.0611 [119]	-0.00142 [119]	98.3 [119]		
MIEC bulk properties							
	V_m	C_{δ_1}	C_{δ_2}	C_{δ_3}	E_{a_δ} [kJmol ⁻¹]	D_{o_v}	E_{a_v} [kJmol ⁻¹]
LSCF	34.09	39.30 [118]	-0.772 [118]	5.04e-4 [118]	77.1 [118]	0.0497 [119] 0.0050 - 0.1 ^b	159.6 [119]
Geometry							
	$elect$	cl	$cath$	an	GDL _{an}	GDL _{cath}	MIC
h (DLR)	7e-6	7e-6	60e-6	540e-6	0.95e-3	0.95e-3	6e-3 ^g
h (EPFL)	7e-6	7e-6	60e-6	540e-6	1.00e-3	2.00e-3	2e-3

^a ASR value, [Ω cm²]

^b Fitting parameter, range in parameter estimations

^c From model assumption

^d Mercury porosity measurement performed at the DLR

^e Averaged value, no strong influence in the conditions of the calibration

^f Value merged with D_{o_v} during the parameter estimations

^g Height of segment

Table 4: Values of the fixed parameters and allowable range of the fitted parameters.

Anode model	EMP	
	w/o correction	correction
ψ	-4930.5	-4990.7
E_{aan}^{ct} [kJ mol ⁻¹]	113.3 [8.4, 5.1]	109.5 [10.4, 6.4]
k_{oan}^{ct} [A cm ⁻²]	13.26 [3.12, 1.90]	21.69 [6.02, 3.66]
r_{an1}^{ct}	0.46 [0.06, 0.04]	0.29 [0.07, 0.05]
r_{an2}^{ct}	0.52 [0.04, 0.02]	0.62 [0.06, 0.04]
τ_{an}^2	8.13 [1.46, 0.89]	12.86 [0.78, 0.48]
D_{ov} [cm ² s ⁻¹]	186.3 [54.0, 32.8]	206.2 [54.8, 33.3]
Anode model	HO2	
	w/o correction	correction
ψ	-4851.6	-4943.5
E_{aan}^{ct} [kJ mol ⁻¹]	153.1 [7.1, 4.3]	131.1 [9.3, 5.6]
k_{oan}^{ct} [A cm ⁻²]	5.95 [0.54, 0.33]	13.46 [1.68, 1.02]
τ_{an}^2	12.99 [0.34, 0.20]	13.35 [0.32, 0.20]
D_{ov} [cm ² s ⁻¹]	141.4 [17.7, 10.8]	137.6 [16.5, 10.0]
Anode model	HO3	
Correction	correction	
ψ	-4935.1	
E_{aan}^{ct} [kJ mol ⁻¹]	133.0 [11.6, 7.1]	
k_{oan}^{ct} [A cm ⁻²]	12.60 [3.45, 2.10]	
τ_{an}^2	13.66 [0.33, 0.20]	
D_{ov} [cm ² s ⁻¹]	163.2 [48.8, 29.6]	

Table 5: Results of the parameter estimations with the DLR data, LSCF cathode. Inside brackets are the 90% confidence interval and standard deviation.

Model	EMP	EMP
\tilde{x}_{O_2}	Jiang et al. [124]	Matsuzaki et al. [128]
ψ	-522.3	-531.9
$E_{a_{cath}}^{ct}$ [kJ mol ⁻¹]	161.4 [69.8, 42.2]	150.5 [70.1, 42.4]
$k_{o_{cath}}^{ct}$ [A cm ⁻²]	0.0553 [0.100, 0.061]	0.1377 [0.251, 0.152]
Model	HO2	HO2
\tilde{x}_{O_2}	Jiang et al. [124]	Matsuzaki et al. [128]
ψ	-546.6	-552.9
$E_{a_{cath}}^{ct}$ [kJ mol ⁻¹]	157.0 [65.7, 39.8]	140.2 [66.0, 39.9]
$k_{o_{cath}}^{ct}$ [A cm ⁻²]	0.1492 [0.255, 0.154]	0.0530 [0.091, 0.055]
Model	HO3	HO3
\tilde{x}_{O_2}	Jiang et al. [124]	Matsuzaki et al. [128]
ψ	-512.6	-524.5
$E_{a_{cath}}^{ct}$ [kJ mol ⁻¹]	159.0 [66.2, 40.0]	147.9 [66.5, 40.2]
$k_{o_{cath}}^{ct}$ [A cm ⁻²]	0.0510 [0.086, 0.053]	0.1329 [0.229, 0.139]

Table 6: Results of the parameter estimation performed on the experimental data from the LENI-EPFL setup (LSM-YSZ). Inside brackets are the 90% confidence interval and standard deviation.

Nomenclature

Latin letters

\dot{Q}	volumetric rate generated thermal energy (W m^{-3})
\mathcal{A}	thermodynamic factor
\mathfrak{R}_i	rate of production of species i ($\text{mol m}^{-3} \text{s}^{-1}$)
\mathfrak{R}_i^m	rate of production of species i ($\text{kg m}^{-3} \text{s}^{-1}$)
ASR	area specific resistance (Ωm^2)
\tilde{u}	unknown variable
\mathbf{Q}	sensitivity matrix
\mathbf{V}	variance-covariance matrix
a	surface coverage of adsorption site or adsorbed species
A_{TPB}	specific area at the triple phase boundary ($\text{m}^2 \text{m}^{-3}$)
A_{MIEC}	internal area of a porous electrode (m^2)
B_o	permeability in porous medium (m^2)
C	constant
c_h	heat capacity (J kg^{-1})
c_i	molar concentration of species i (mol m^{-3})
c_t	total molar concentration (mol m^{-3})
D	diffusion coefficient in solid medium ($\text{m}^2 \text{s}^{-1}$)
d_g	particle diameter (m)
d_p	pore diameter (m)
D_{ij}^e	effective bulk diffusivity of binary pair in porous medium ($\text{m}^2 \text{s}^{-1}$)
D_{iM}^e	effective Knudsen diffusivity of species i in porous medium ($\text{m}^2 \text{s}^{-1}$)

dH_o	enthalpy of reaction (J mol^{-1})
E	electric potential (V)
E_a	activation energy (J mol^{-1})
F	Faraday's constant 96485 (C mol^{-1})
f	molar activity coefficient
F_d	F value in statistical test
H	enthalpy (J kg^{-1})
h	thickness (m)
h^c	convection heat transfer coefficient ($\text{W m}^{-2} \text{K}^{-1}$)
i_o	exchange current density (A m^{-2})
i_t	faraidic transfer current density (A m^{-2})
j	current density (A m^{-2})
K	ratio of rate constants
k	rate constant
K^{eq}	equilibrium constant
k_o	kinetic constant
K_{chem}	apparent surface exchange coefficient (m s^{-1})
L	length (m)
l_g	distance between grains (m)
M_i	molecular weight of species i (kg mol^{-1})
n	porosity
N_i	molar flux of species i ($\text{mol m}^{-2} \text{s}^{-1}$)
p	pressure (Pa)

p^{atm}	atmospheric pressure 101325 (Pa)
R	universal gas constant 8.314 (J mol ⁻¹ K ⁻¹)
r	apparent reaction order
s	variance
T	temperature (K)
t	time (s)
t_i	Student distribution
T_{amb}	ambient temperature, 298 (K)
T_{ref}	reference temperature, 873 (K)
u	gas velocity (m s ⁻¹)
V	potential in ionic or electronic conducting phases (V)
V_m	molar volume (m ³ mol ⁻¹)
x_i	mole fraction of species i
y	system response
z_i	charge number of species i

Greek letters

α	symmetry coefficient
β	probability level
χ^2	χ^2 distribution
δ	deviation from stoichiometry
η	overpotential (V)
λ	thermal conductivity (W m ⁻¹ K ⁻¹)
μ^*	electrochemical potential (J mol ⁻¹)

μ^{chem}	chemical potential (J mol ⁻¹)
μ_g	viscosity (Pa s)
ν_d	diffusion volume (m ³)
ω	mass fraction of species i
Φ	potential [V]
Ψ	objective function
ρ	density (kg m ⁻³)
ρ^e	effective electrical resistivity (Ω m)
σ^e	effective electrical conductivity (S m ⁻¹)
τ	tortuosity
θ	parameter
ε	emissivity
ς	Stefan-Boltzmann constant $5.670 \cdot 10^{-8}$ (W m ⁻² K ⁻⁴)
ϑ	control variable
ξ	correction factor

Indices

elchem electrochemical

a anodic

an anode

avg average

bc boundary conditions

c cathodic

cath cathode

<i>cl</i>	compatibility layer
<i>cond</i>	conduction
<i>conv</i>	convection
<i>e</i>	electron
<i>el</i>	electronic
<i>elect</i>	electrolyte
<i>exp</i>	experiment
<i>fnce</i>	furnace
<i>g</i>	indice for gases, either air or fuel
<i>h</i>	hole
<i>htl</i>	heat losses
<i>ion</i>	ionic
<i>isl</i>	insulation
<i>leak</i>	leakage
<i>o</i>	initial, dense state
<i>rep</i>	repetition
<i>resp</i>	response
<i>rx</i>	reaction
<i>s</i>	index for solid parts, individual components or averaged structure
<i>tot</i>	total
<i>u</i>	useful
<i>v</i>	oxygen vacancy

Superscripts

ct charge transfer

a anodic

c cathodic

eq equilibrium

Acronyms

ASC anode-supported cell

ASR area specific resistance

CTE coefficient of thermal expansion

CT charge-transfer

DEM discrete element method

DGM dusty gas model

DOE design of experiment

EIS electrochemical impedance spectroscopy

GCI galvanostatic current interruption

GDC gadolinia-doped ceria

GDL gas diffusion layer

HO hydrogen oxidation

IT intermediate temperature

IV current-voltage

LOF lack of fit

LSCF lanthanum strontium cobaltite ferrite

LSF lanthanum strontium ferrite

LSM lanthanum strontium manganite

LZO lanthanum zirconate

MEA membrane electrode assembly

MIC metallic interconnect

MIEC mixed-ionic-electronic conductor

Ni-YSZ nickel-YSZ anode in reduced state

ORR oxygen reduction reaction

RDS rate-determining step

SCR steam-to-carbon ratio

SDC samaria-doped ceria

SMR steam-methane reforming reaction

SRU single repeating unit

SSM state-space modelling

SS sum of square

SZO strontium zirconate

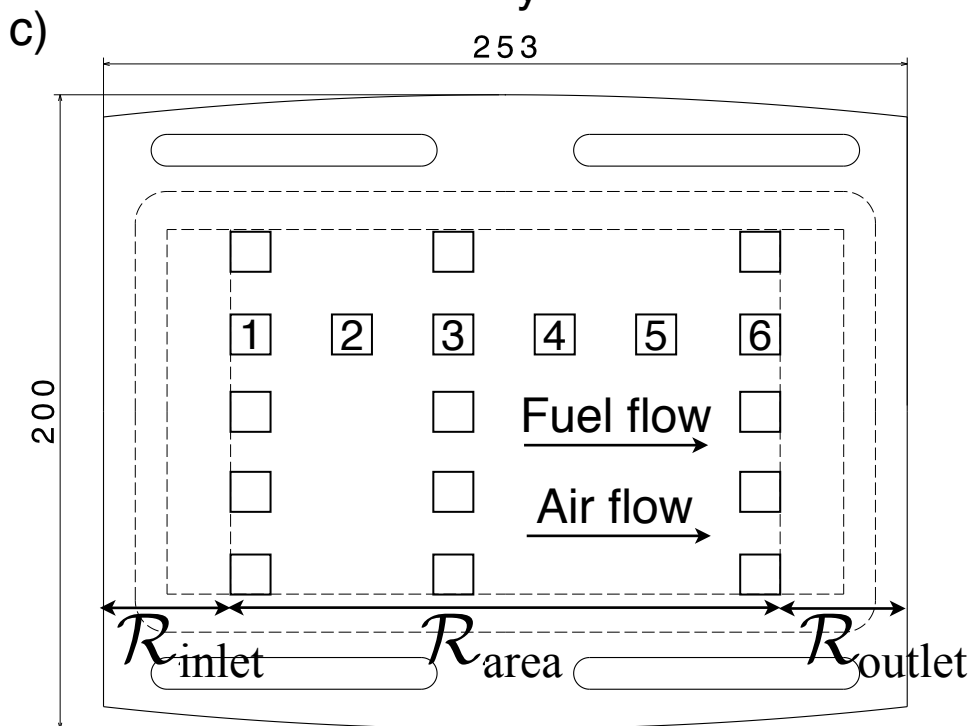
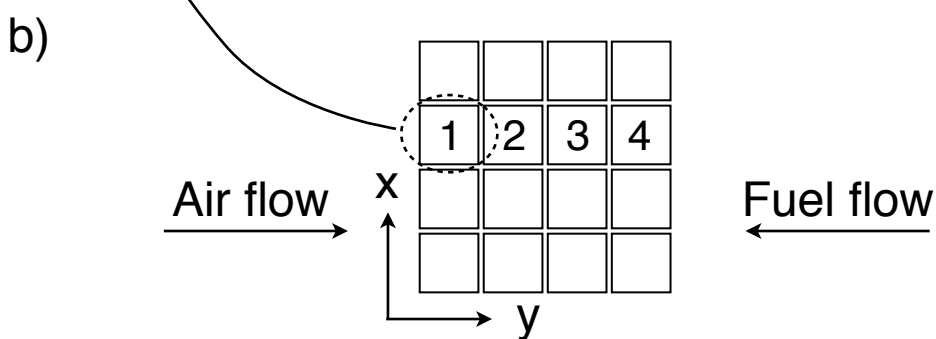
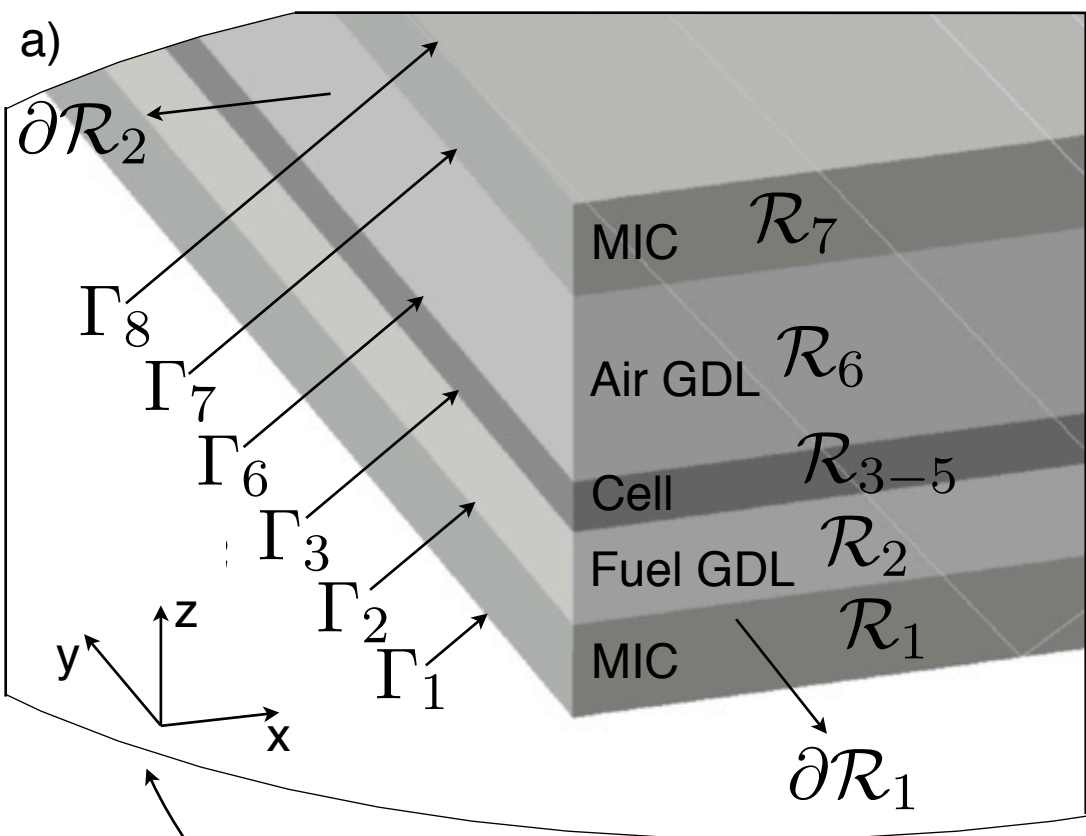
TPBL triple phase boundary length

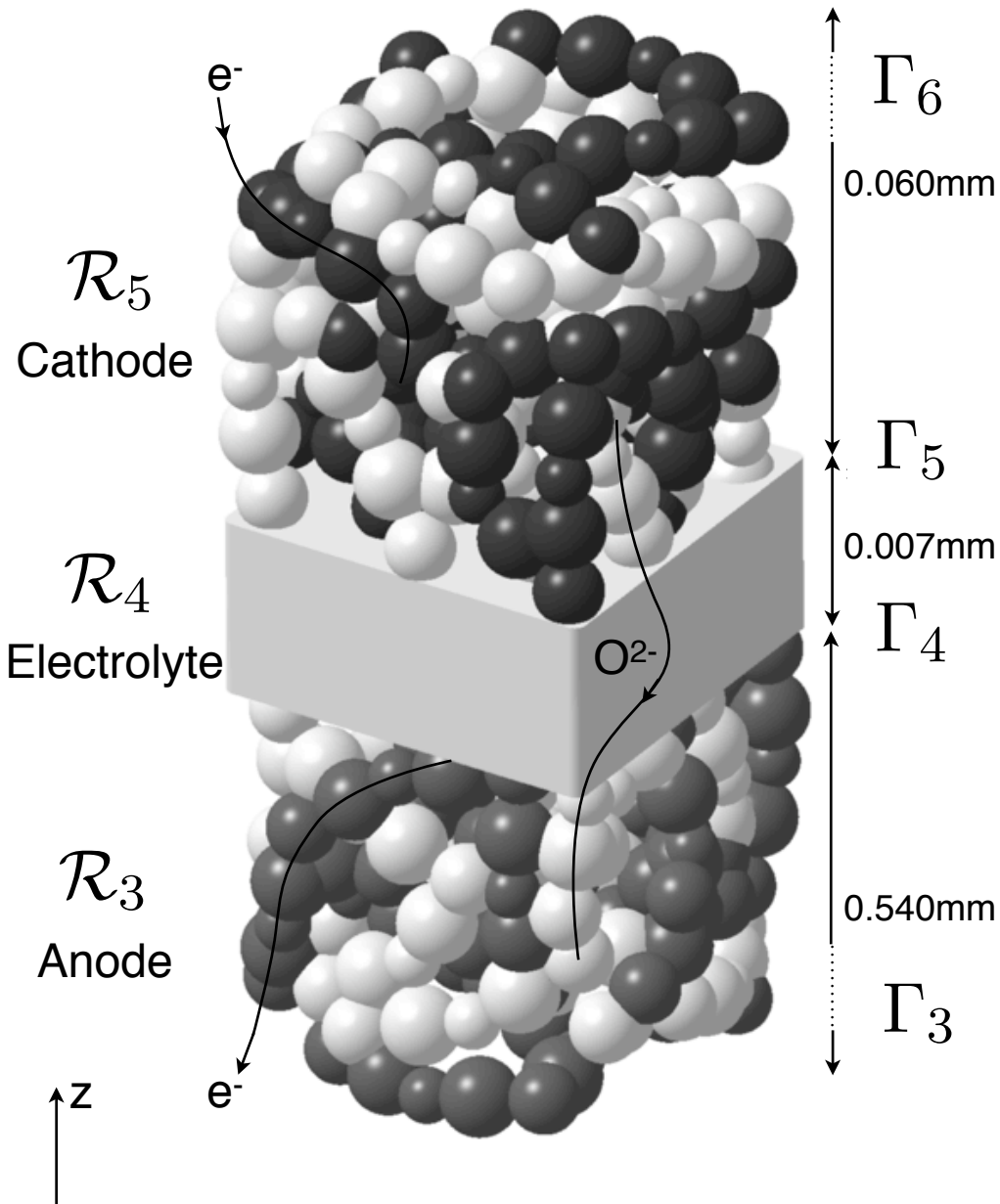
TPB triple phase boundary

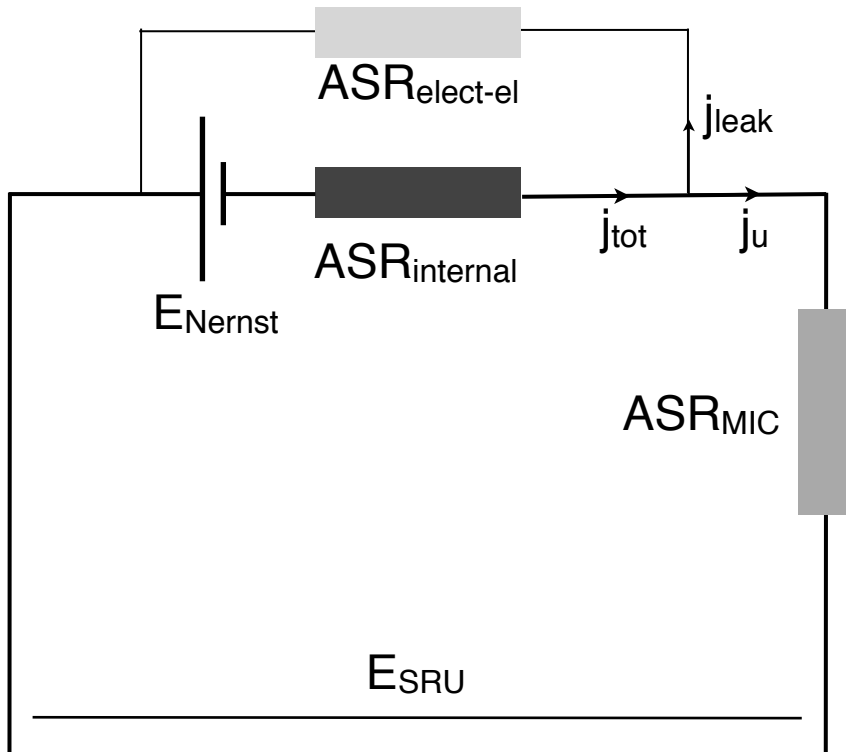
WS water-gas shift reaction

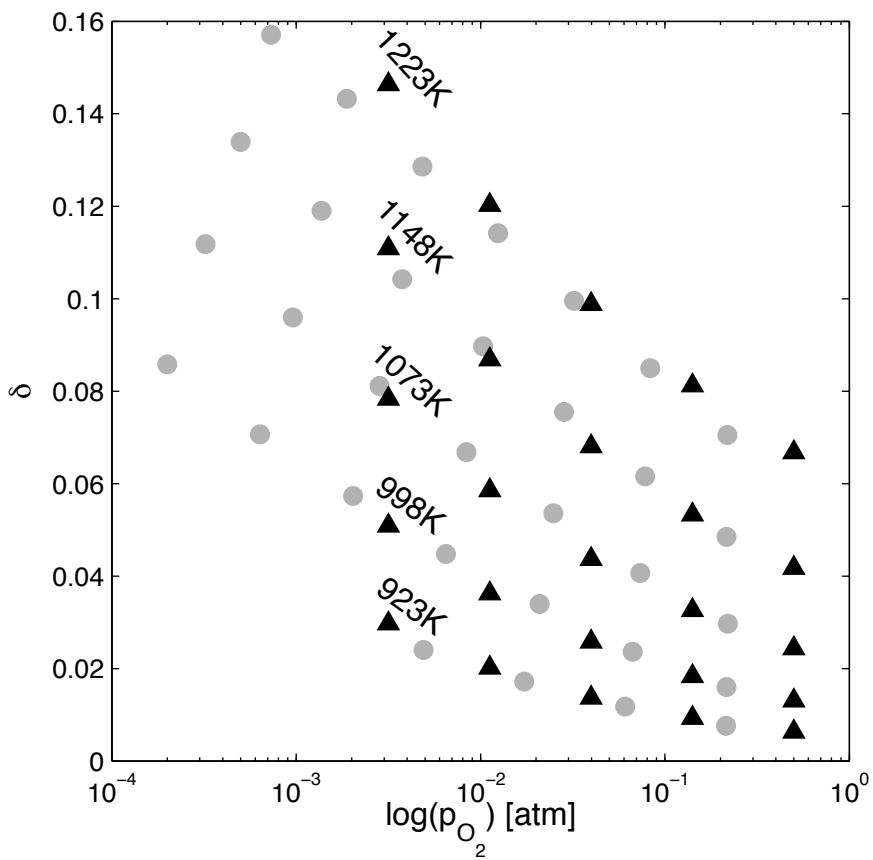
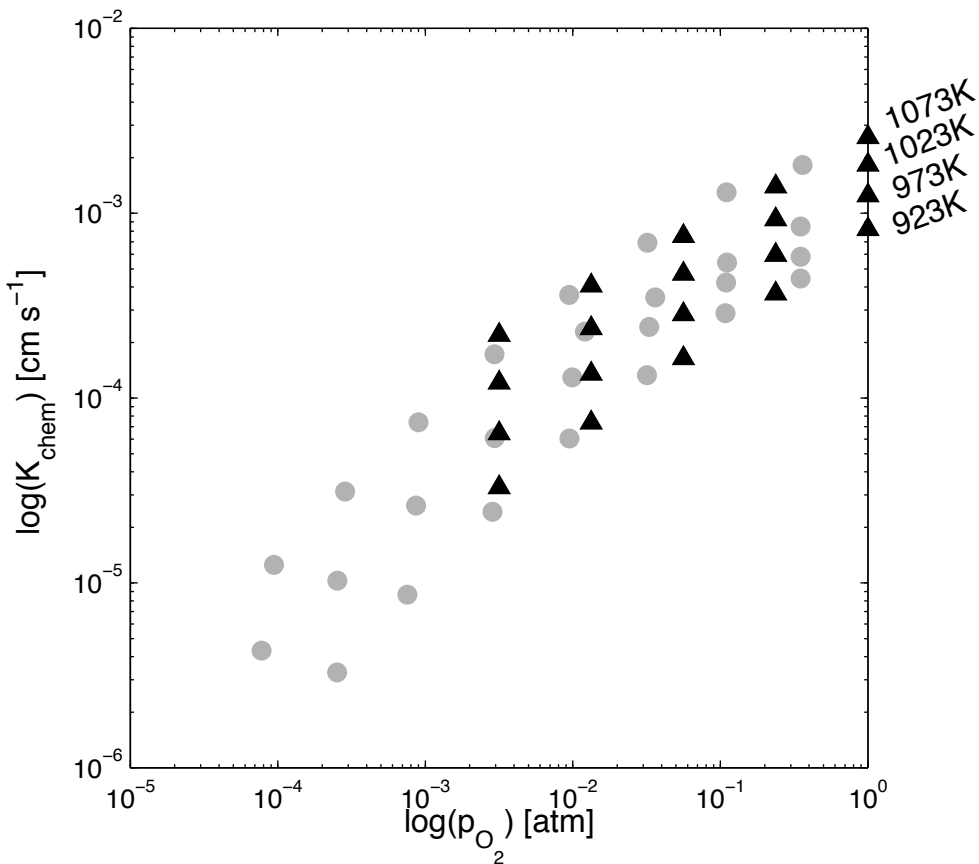
YDC yttria-doped ceria

YSZ yttria-stabilised zirconia





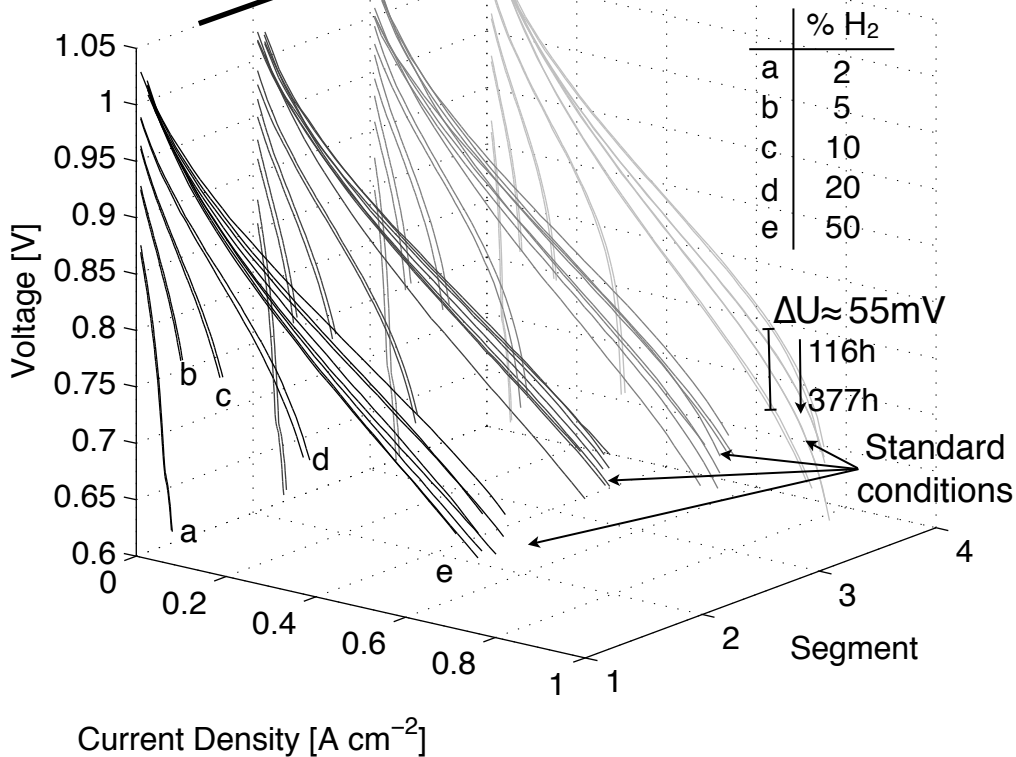


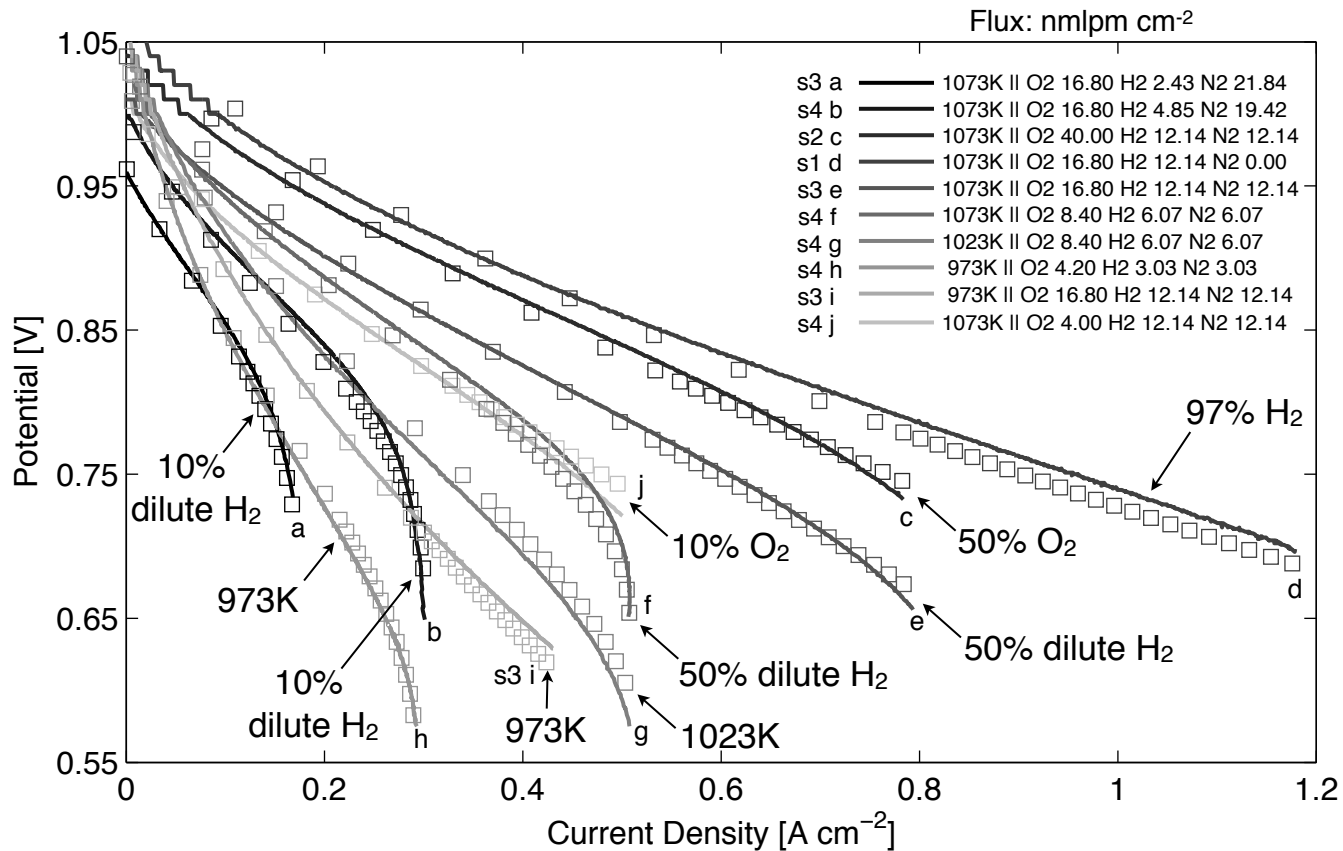


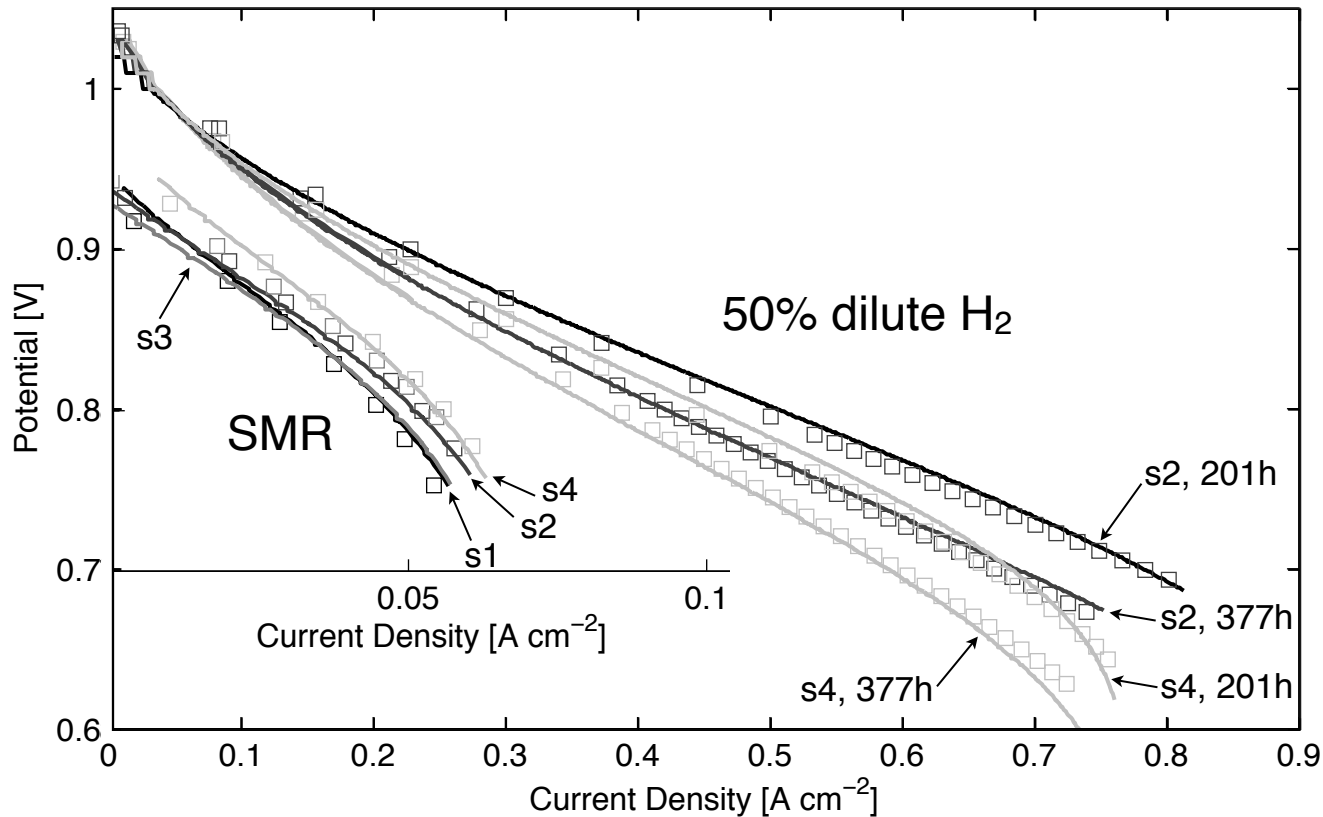
Air: 80 nmlpm cm⁻²

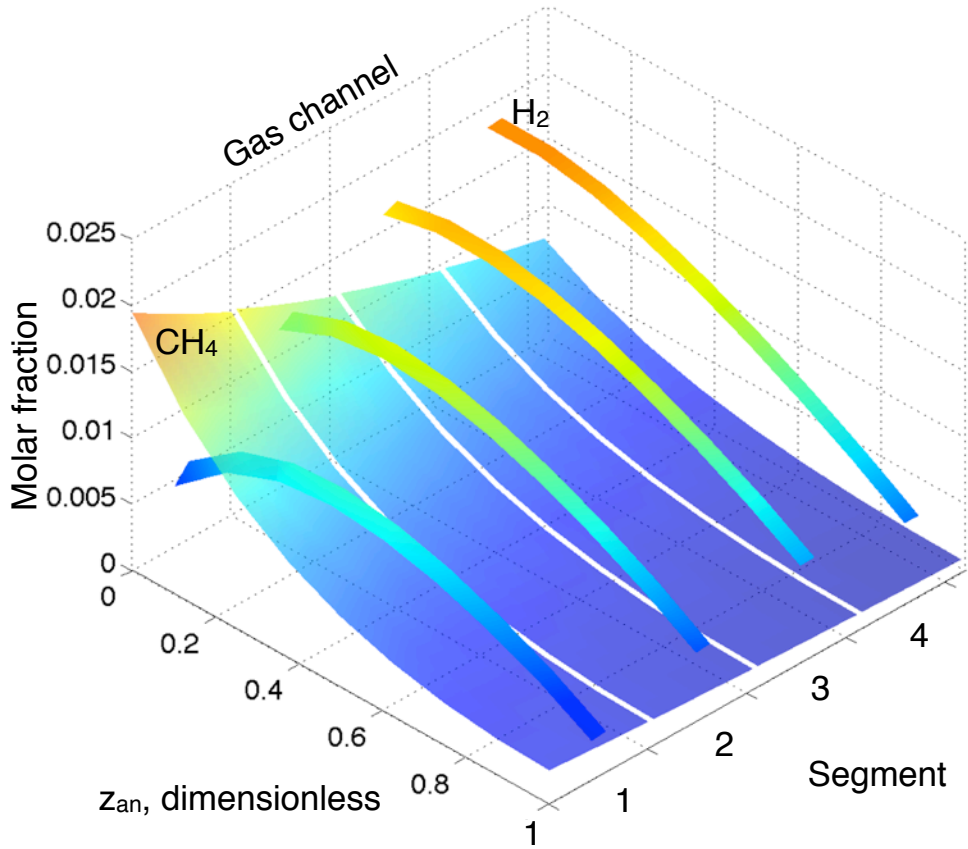
Fuel: 25 nmlpm cm⁻²

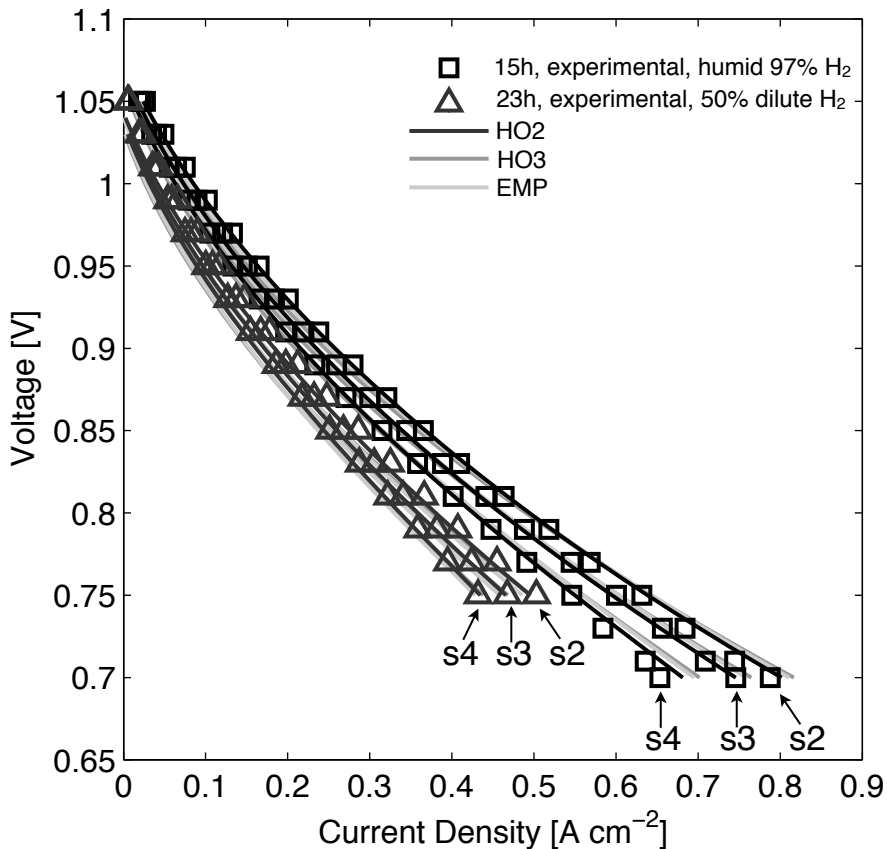
Fuel flow 

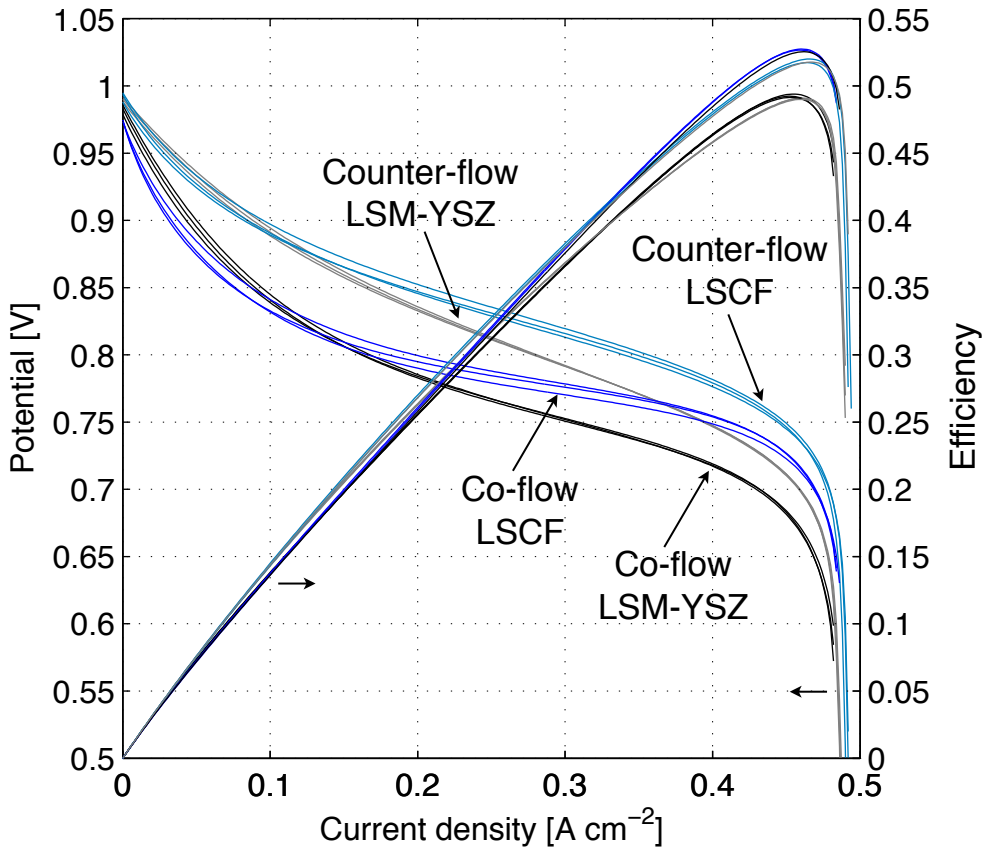


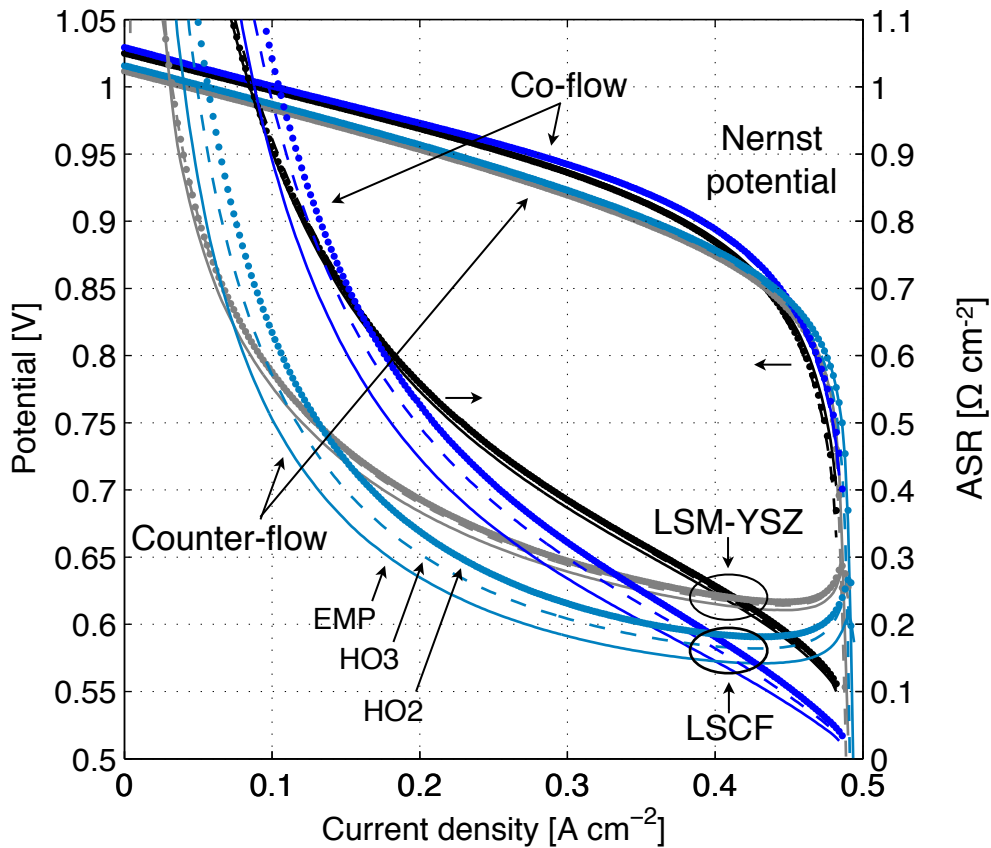


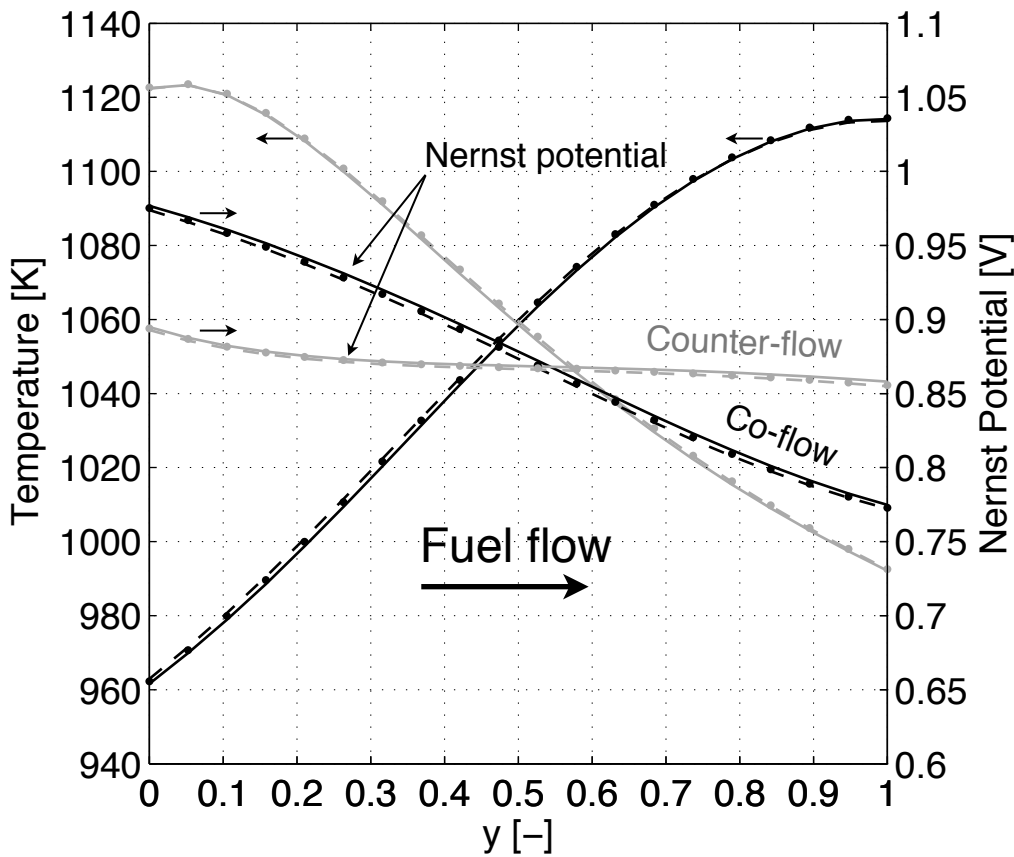
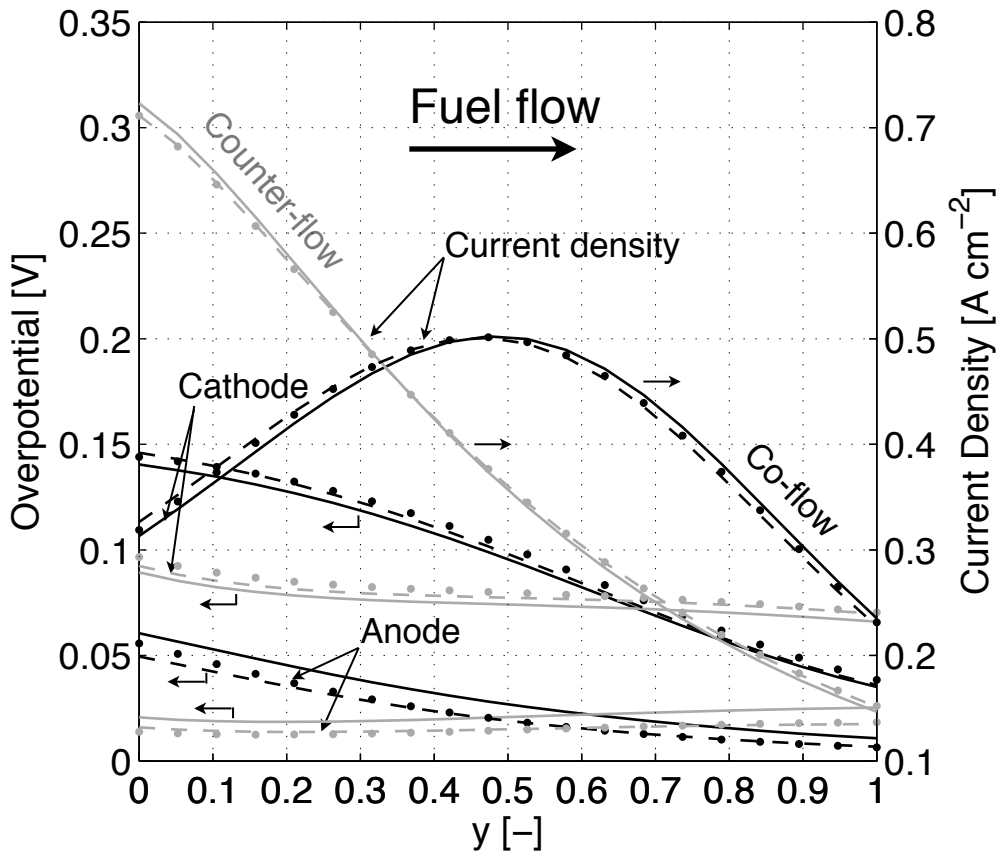


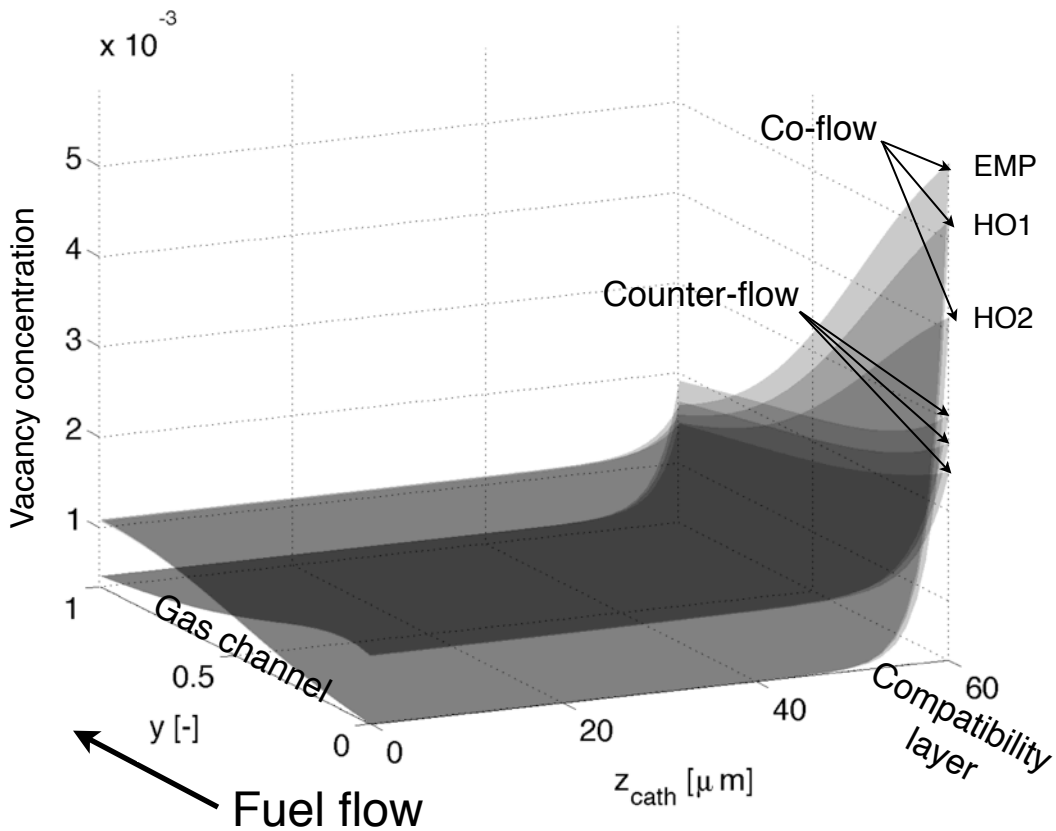












Electrochemical model of solid oxide fuel cell for simulation at the stack scale. Part II: Implementation of degradation processes

Arata Nakajo^{*1}, Pietro Tanasini¹, Stefan Diethelm¹, Jan Van herle¹, and Daniel Favrat¹

¹Laboratoire d'Energétique Industrielle (LENI), Institut de Génie Mécanique, Ecole Polytechnique Fédérale de Lausanne, 1015 Lausanne, Switzerland

^{*}corresponding author: arata.nakajo@epfl.ch, tel: +41 21 693 35 05

Abstract

The degradation of the electrochemical performance of solid oxide fuel cell (SOFC) devices is a major hurdle to overcome before commercialisation. The interplay between the phenomena and the long testing times complicate the research, which highlights the relevance of modelling to propose mitigation approaches.

This study comprises two parts. This Part II proposes approaches for the simulation of the degradation induced by: (i) interconnect corrosion, (ii) loss of ionic conductivity of the ion-conducting materials, (iii) nickel particle growth in the anode, (iv) chromium contamination and (v) formation of insulating phases in the cathode. The literature survey highlights the lack of data for a completely consistent calibration of the models, despite the simplifications. The support for the implementation is the electrochemical model validated in Part I and a two-dimensional model of the cell and interconnection system. The cathode largely contributes to the degradation. The local overpotential predominantly governs chromium contamination, which can promote the formation of insulating phases, as operation proceeds. The local electronic current density has comparatively a weak direct influence on the degradation. Qualitative agreement with experimental data from the literature could be achieved, without dedicated adjustments of the parameters.

Keywords: Solid Oxide Fuel Cell, electrochemical modelling, degradation, electrode contamination, nickel coarsening

1 Introduction

Commercialisation of solid oxide fuel cell (SOFC) devices is currently hindered by the degradation of their performance, which is above the specification of most foreseen applications. There are various possible causes mainly related to localised micro-structural and composition alterations, ranging from the nature of materials to defective control strategy or implementation in a system. A main difficulty in the elaboration of mitigation strategies arises from the interplay between all possible degradation processes. Therefore, the means to ensure an adequate lifetime of SOFC devices require investigations at different scales, from particles to system response. Knowledge from correspondingly overlapping fields of research is required, from material science to system integration, through structural analysis.

Button cells and short-stack testing is the practical common way to validate new materials or designs before their implementation in a functional stack. Long-term and/or cycling conditions enable to infer possible degradation mechanisms. Primdahl et al. [1] have focused on Ni-YSZ anodes operated at high temperature. A negligible degradation rate is observed at 1323 K, while it increases at lower temperature (1123 K). In addition, the use of raw materials from different suppliers results in different behaviours. The study of Koch et al. [2] on anode supported cells based on lanthanum strontium cathodes (LSM) is a typical example of button cell tests in an alumina setup. These authors suggest that the strong dependence of the degradation rate on the cell potential is dominated mainly by the anode and related to the Ni-NiO reduction-oxidation potential. In contrast, Hagen et al. [3] have identified a predominant contribution of the LSM-YSZ cathode to the overall degradation in their similar tests, especially at low temperature. Post-mortem analysis has revealed local delaminations at the interface between the cathode and the electrolyte, coarsening and loss of nickel as possible causes of the observed degradation patterns. Further investigations on these experiments [4, 5] have enabled to attribute quite reliably the degradation to the formation of lanthanum or strontium zirconates (LZO,SZO).

Button cell tests are of great help to understand and reduce the intrinsic degradation of different SOFC materials and configurations. Besides discrete mechanical failures in the membrane electrode assembly (MEA) due to thermal stresses, mechanical interactions with other components or reoxidation/reduction (redox), the degradation processes acting during controlled aging experiments are driven by the chemical instability of the materials [6]. Therefore, button cell tests in alumina housing do not reflect the conditions that a cell has to withstand in a SOFC stack. Indeed, detrimental direct or indirect reactions can arise from chemical interactions with the other components of the stack, with volatile species carried by the gases or impurities in the raw materials [7]. This embraces all issues related to poisoning or pollution, epitomised by

the contamination of the cathode by chromium evaporated from the metallic parts of the system [8,9], and poisoning of the anode by sulfur in natural gas. The effects of these issues are visible in short-stack tests [10] or can be specifically investigated in controlled conditions [11].

A careful one-by-one test strategy inevitably results in a huge, hence costly and time-consuming, test matrix. There is currently growing interest in accelerated testing methods, which consist in using wisely selected harsh test conditions. The accuracy relies on the understanding of the degradation mechanisms. Indeed, the selected test conditions should activate the correct degradation processes; yet it should also ensure that their regime is representative of stack conditions. Interactions between the degradation processes further complicate the situation. This is evident at the single repeating unit (SRU) scale, where the composition of the gases, the temperature and the local overpotential are unevenly distributed. A non-uniform degradation over the SRUs hence affects the behaviour of the stack, which can lead to discrete mechanical failures during transient operation [12–14]. Modelling can be of great help to design experiments and provide insights into the underlying physics.

A first practical approach consists in recasting the data of a measurement campaign into a look-up table, which expresses degradation, and possibly recovery rates as a function of conditions. While this approach can serve for the simulation at the SRU scale, its durability and versatility is somewhat compromised by the complexity of the degradation phenomena and their interaction. Therefore, its ability to provide guidance for mitigation strategies and accelerated testing is very limited. In contrast, physical modelling enables a separation of the contributions at the cost of dedicated measurements, and flexibility in the addition of interactions and phenomena, as the knowledge increases. The parameters needed for the simulation of the individual degradation processes can be estimated from post-mortem analysis [5, 10], or dedicated measurements [15–17].

An example of a degradation phenomenon considered in SOFC models is nickel coarsening which can be quantified by imaging techniques [18,19]. Indeed, a modification of the triple-phase boundary length (TPBL) is straightforward in existing composite models for electrode development [20–22]. Nickel coarsening alone can not explain all reported degradation patterns. In particular, the trend reported by Primdahl et al. [1] is opposite. At the SRU scale, the increase of the resistance of the metallic interconnect (MIC) has been investigated [23]. A more refined analysis of degradation patterns in electrochemical impedance spectra (EIS) for delamination has been carried out by Gazzarri et al. [24]. Nevertheless, the relative lack in quantitative data on the primary causes of the degradation phenomena, e.g. grain coarsening or chromium deposition rates, enables in the best case preliminary modelling investigations of the degradation. This is particularly

evident when dependences on temperature or gas composition are needed, which are vital for a comprehensive analysis at the SRU/stack scale. The current density or temperature profiles over the SRU can be modified by design, e.g. co- or counter-flow, and/or control strategy, to indirectly prevent a premature degradation of specific areas.

Part II of the present study seeks to integrate degradation phenomena in the electrochemical model described in Part I [25] for simulation at the SRU/stack scale. Investigations are performed for intermediate temperature, anode-supported cells (IT-SOFC) with a LSM-YSZ cathode. The first task is to identify relevant degradation processes, for which the amount of available data is sufficient to deduce and calibrate empirical or physically-based relations. Then, the modelling strategy and ensuing assumptions are discussed to enlighten the kind of experimental data needed by the proposed implementation of degradation phenomena. The one-dimensional electrochemical model described in Part I [25] has some limitations for the present study in terms of geometry, as well as details in the modelling of the anode. Therefore, the implementation of external degradation relations is illustrated on a two-dimensional model of the MEA/gas diffusion layer (GDL)/MIC, hereafter referred to as REV, to better identify the range of validity of the one-dimensional model. Comparison between the one-dimensional model and the REV model are performed for three local conditions found in a SRU in operation. The relative contributions of the degradation phenomena to the possible patterns in the evolution of the current density during polarisation at a constant potential are investigated, with an emphasis on the interactions. A coarse comparison between experimental data from literature and simulations is then performed. The variation of the thickness of the cathode to alleviate chromium contamination of the LSM-YSZ cathode is discussed in light of model assumptions. Finally, the effects of operating conditions on the behaviour of the selected degradation phenomena are explored, to provide guidance for control strategy and design.

2 Modelling approach

2.1 Model of cell and interconnection

The geometry of the REV model is depicted in Figure 1, along with the denomination of the different domains and boundaries. Similar to the one-dimensional version of the electrochemical model for the simulation at the SRU/stack model described in Part I [25], a uniform temperature T_s is assumed in the whole REV. Properties and relations for the calculation of diffusion coefficients and effective conductivities remain unchanged. The main improvement is the model of composite electrode implemented on the anode side.

Indeed, degradation rates can be increased by local current constrictions or depletion of reactants, which are not captured in a one-dimensional approach. The model, as well as all degradation models, is implemented in gPROMS [26], an equation-oriented process modelling tool.

[Figure 1 about here.]

[Figure 2 about here.]

Charge conservation equations for both electronic and ionic conducting phases must be fulfilled in all domains.

$$\nabla \cdot (\sigma_{el_s}^e \nabla V_{el_s}) = 0 \quad \text{in } \mathcal{R}_s, s = 1, 2, 6, 7 \quad (1)$$

$$\nabla \cdot (\sigma_{el_s}^e \nabla V_{el_s}) = -A_{\text{TPB}_s} i_{t_s} \quad \text{in } \mathcal{R}_s, s = 3, 5 \quad (2)$$

$$\nabla \cdot (\sigma_{ion_s}^e \nabla V_{ion_s}) = A_{\text{TPB}_s} i_{t_s} \quad \text{in } \mathcal{R}_s, s = 3, 5 \quad (3)$$

$$\frac{\partial}{\partial z} \left(\sigma_{el}^e \frac{\partial V_{el}}{\partial z} \right) = 0 \quad \text{in } \mathcal{R}_4 \quad (4)$$

$$\frac{\partial}{\partial z} \left(\sigma_{ion}^e \frac{\partial V_{ion}}{\partial z} \right) = 0 \quad \text{in } \mathcal{R}_4 \quad (5)$$

$$\sigma_{el_s}^e \nabla V_{el_s} = -\mathbf{j}_{el_s} \quad \text{in } \mathcal{R}_s, s = 1-7 \quad (6)$$

$$\sigma_{ion_s}^e \nabla V_{ion_s} = -\mathbf{j}_{ion_s} \quad \text{in } \mathcal{R}_s, s = 3-5 \quad (7)$$

A small leakage current in the thin electrolyte due to a finite electronic resistivity [27] is included. σ^e refers to effective conductivities of the ionic and electronic conducting phases. A correction is therefore required in the electrode (see Appendix A.2). The modelled geometry lacks in detail to consistently handle current constriction at the particle scale. Yet, thin electrolytes are known to exhibit a higher resistance compared with that of thick ones, relative to their thickness. Therefore, an equivalent ionic conductivity computed by the interpolated relation proposed by Fleig et al. [28] and described in Part I [25] is used together with a one-dimensional description.

Symmetry boundary conditions are applied on side boundaries, while continuity is enforced in the MEA.

$$\mathbf{n} \cdot (\sigma_{el_s}^e \nabla V_{el_s}) = 0 \quad \text{at } \Gamma_s \quad s = sy, c_2, s_2, c_3, c_6, s_6, c_7 \quad (8)$$

$$\mathbf{n} \cdot (\sigma_{ion_s}^e \nabla V_{ion_s}) = 0 \quad \text{at } \Gamma_s \quad s = sy, c_3, r_3, c_6, r_6 \quad (9)$$

$$V_{el_{elect}} = V_{el_{an}} \quad , \quad V_{ion_{elect}} = V_{ion_{an}} \quad \text{at } \Gamma_4 \quad (10)$$

$$\mathbf{j}_{el_{elect}} = \mathbf{j}_{el_{an}} \quad , \quad \mathbf{j}_{ion_{elect}} = \mathbf{j}_{ion_{an}} \quad \text{at } \Gamma_4 \quad (11)$$

$$V_{el_{elect}} = V_{el_{cath}} \quad , \quad V_{ion_{elect}} = V_{ion_{cath}} \quad \text{at } \Gamma_5 \quad (12)$$

$$\mathbf{j}_{el_{elect}} = \mathbf{j}_{el_{cath}} \quad , \quad \mathbf{j}_{ion_{elect}} = \mathbf{j}_{ion_{cath}} \quad \text{at } \Gamma_5 \quad (13)$$

The modelling of additional interfacial electronic resistances at the GDL/MIC or GDL/MEA interfaces arising from the growth of an oxide scale on top of metallic components proceeds in a simplified manner. The geometry is not modified by the growth of the oxide scale and one-dimensional conduction is assumed. This simple approach is restricted here to the case of oxide scales, but could be used for any other additional interfacial resistance.

$$V_{el_{GDL_s}} = V_{el_{MIC_s}} - \mathbf{n} \cdot \mathbf{j}_{el_{MIC_s}} \text{ASR}_{MIC_s} \\ \text{at } \Gamma_s \quad s = r_2, r_6$$

Mass transport equations are solved as well in the electrode, assuming uniform gas compositions in the distribution channels, at a fixed y position. On the cathode side,

$$\nabla \cdot (\nabla x_{O_2}) = - \frac{RT_s}{p_{atm}} \frac{1}{4FD_{O_2}} A_{TPB_{cath}} i_{t_{cath}} \quad \text{in } \mathcal{R}_5 \quad (14)$$

$$\mathbf{n} \cdot (\nabla x_{O_2}) = 0 \quad \text{at } \Gamma_5, \Gamma_{r6} \quad (15)$$

$$x_{O_2_{cath}} = x_{O_2} \quad \text{at } \Gamma_{c6} \quad (16)$$

On the anode side, the dusty-gas model is solved along with the equation of continuity. The empirical kinetic approach of Achenbach et al. [29] for steam-methane reforming is used (see Part I [25]).

$$- \nabla x_i - \frac{x_i}{p_{an}} \nabla p_{an} - x_i \frac{B_{oan}}{\mu g_{an} D_{iM}^e} \nabla p_{an} = \sum_{j=1, j \neq i}^n \frac{x_j \mathbf{N}_i - x_i \mathbf{N}_j}{c_{tan} D_{ij}^e} + \frac{\mathbf{N}_i}{c_{tan} D_{iM}^e} \quad \text{in } \mathcal{R}_3 \quad (17)$$

$$\nabla p_{an} = \frac{\sum_{j=1}^n \frac{\mathbf{N}_j}{D_{jM}^e}}{\frac{1}{RT} + \frac{B_{o_{an}}}{\mu_{g_{an}}} \sum_n \frac{x_i}{D_{iM}^e}} \text{ in } \mathcal{R}_3 \quad (18)$$

$$\nabla \cdot \mathbf{N}_i = \mathfrak{R}_i \text{ in } \mathcal{R}_3 \quad (19)$$

$$\text{at } \Gamma_4, : \begin{cases} \mathbf{n} \cdot \mathbf{N}_{H_2} = -\mathbf{n} \cdot \mathbf{N}_{H_2O} = \frac{j_{tot}}{2F} \\ \mathbf{n} \cdot \mathbf{N}_i = 0, \text{ i}=\text{N}_2, \text{CH}_4, \text{CO}, \text{CO}_2 \end{cases} \quad (20)$$

$$\text{at } \Gamma_{c3}, : \begin{cases} x_{i_{an}} = x_i \\ p_{an} = p^{atm} \end{cases} \quad (21)$$

$$\mathbf{n} \cdot \mathbf{N}_i = 0 \text{ at } \Gamma_{r3} \quad (22)$$

A word of caution is required for the anode side. Mass transport and charge conservation equations are not rigorously coupled by the transfer current, as seen in Eq.19 and Eq.21. This assumption is reasonable, as long as the electrochemically active thickness is small compared with that of the anode support.

The previous boundary conditions are written for the case of an impervious interconnecting material. However, porous GDL are implemented as well. The adaptation of the aforementioned field equations and boundary conditions is straightforward.

The local overpotentials in the electrodes are computed by introducing a reference potential, which shifts the electrode reversible potential on the cathode side to zero and that on the anode side to the Nernst potential [30].

$$\eta_{cath} = V_{el_{cath}} - V_{ion_{cath}} \quad \text{in } \mathcal{R}_5 \quad (23)$$

$$\eta_{an} = V_{el_{an}} - V_{ion_{an}} + E_{Nernst} \quad \text{in } \mathcal{R}_3 \quad (24)$$

Equipotentials are assumed at Γ_1 and Γ_8 and serve to assign operating conditions. This approach is not totally accurate in the case of stacked SRUs, as the periodicity of the current lines is not enforced.

The underlying assumptions of the expressions for the charge transfer currents have been discussed in Part I [25]. The selected expressions are respectively for the cathode:

$$i_{t_{cath}} = i_{o_{cath}}^{ct} \frac{\left(\frac{x_{O_2}}{\tilde{x}_{O_2}}\right)^{3/8}}{1 + \left(\frac{x_{O_2}}{\tilde{x}_{O_2}}\right)^{1/2}} \left[\exp\left(-\frac{1}{2} \frac{F\eta_{cath}}{RT_s}\right) - \exp\left(\frac{3}{2} \frac{F\eta_{cath}}{RT_s}\right) \right] \text{ in } \mathcal{R}_5 \quad (25)$$

$$i_{o_{cath}}^{ct} = T_s k_{o_{cath}} \exp\left[-\frac{E_{a_{cath}}}{R} \left(\frac{1}{T_s} - \frac{1}{T_{ref}}\right)\right] \quad (26)$$

$$\tilde{x}_{O_2} = \tilde{k}_{o_{cath}} \exp\left[-\frac{\tilde{E}_{a_{cath}}}{R} \left(\frac{1}{T_s}\right)\right] \quad (27)$$

and the anode:

$$i_{t_{an}} = i_{o_{an}}^{ct} \frac{\left(\frac{x_{H_2}}{\tilde{x}_{H_2}}\right)^{1/4} x_{H_2O}^{1/4}}{1 + \left(\frac{x_{H_2}}{\tilde{x}_{H_2}}\right)^{1/2}} \left[\exp\left(\frac{1}{2} \frac{F}{RT_s} \eta_{an}^{ct}\right) - \exp\left(-\frac{3}{2} \frac{F}{RT_s} \eta_{an}^{ct}\right) \right] \text{ in } \mathcal{R}_3 \quad (28)$$

$$i_{o_{an}}^{ct} = T_s k_{o_{an}} \exp\left[-\frac{E_{a_{an}}}{R} \left(\frac{1}{T_s} - \frac{1}{T_{ref}}\right)\right] \quad (29)$$

$$\tilde{x}_{H_2} = \tilde{k}_{o_{an}} \exp\left[-\frac{\tilde{E}_{a_{an}}}{R} \left(\frac{1}{T_s}\right)\right] \quad (30)$$

2.2 Degradation processes

2.2.1 Metallic interconnect

The decrease of the operating temperature in IT-SOFC enables the use of cheaper metallic components, which has consequences beyond the SOFC stack, as reliable piping between all units of a whole SOFC system is not trivial. The main advantages of MICs over their ceramic counterparts, typically made of

lanthanum chromites, are lower cost and drastic increase in design possibilities, due to their ductility and higher thermal conductivity [31, 32]. In operation, plastic and creep deformation can induce structural failures [14, 33, 34], but this behaviour might actually delay the direct mixing of fuel and air, compared with brittle ceramic interconnects. These decisive advantages are unfortunately balanced by the lower chemical stability of metallic components in SOFC conditions. The most obvious and visible consequence is corrosion which provokes the growth of an oxide scale of lower electric conductivity than the bulk. Other serious issues include the evaporation of chromium species [9, 35], structural instabilities [36] and the detrimental reaction with the sealing materials, be it compressive gaskets [37] or glass [38, 39].

Preliminary selections [40] have highlighted two main classes of metallic alloys: ferritic and nickel-based chromia-forming alloys. Most of the research for SOFC application has focused on the ferritic alloys, due to their significantly lower cost and the closer match of their coefficient of thermal expansion (CTE) to those of SOFC materials [41, 42]. Typical examples of ensuing commercial products are Crofer22APU or H [32, 41] and ZMG232 [43], the Cr content of which is around 20-25 wt.%. This value ensures the stability of the growing oxide scale by preventing the depletion of Cr in the scale sub-layer [40]. The specific feature of Crofer22 and ZMG232 is the multilayered structure of the oxide scale in both oxidising (air) and reducing (fuel) atmospheres. Indeed, the addition of Mn promotes the development of a thin $(\text{Cr, Mn})_3\text{O}_4$ spinel layer on top of the Cr_2O_3 scale, as Mn^{2+} diffuses faster than Cr^{3+} in Cr_2O_3 . This spinel layer of acceptable electrical conductivity [44–46] reduces the oxide scale growth and the release of Cr species, which detrimentally react with the cathode. The situation is actually more complicated and extensive research has been undertaken to understand the processes to improve the durability of MICs. For instance, differences in the oxidation behaviour appear, whether the MIC is subjected to oxidising or reducing environments [43, 47–50]. Yang et al. [51] have tentatively related the observed growth of anomalous oxides on the air side, when the sample is simultaneously subjected to air and fuel on different faces, so-called dual conditions, to the diffusion of hydrogen through the bulk of the alloy. This observation which would add a constraint on the MIC thickness is not ascertained by other groups [38]. Presence of minor elements, such as Si or Al can provoke the formation of undesirable phases [52]. Additional alloying is required, in turn, to overcome these issues, as costs usually scale with purity. Scanning electron microscope (SEM) observations reveal the presence of an intermediate layer under the oxide scale, where a depletion of some key element occurs [53]. Therefore the durability of the beneficial effects of added elements is questionable. Finally, the area specific resistance (ASR) exhibits a quick drop during the first hours at high temperature, then steadily increases. This behaviour likely reflects the evolution of the composition and micro-structure of the oxide scale during its initial formation [53, 54].

All these observations highlight the critical role of direct and indirect chemical interactions, hence need to consider the improvement of the MIC as component of an interconnection and sealing system.

There is now evidence that any one SOFC-dedicated alloys cannot fulfil all requirements [35, 55], irrespective of the efforts placed on bulk modification. The complementary improvement approach consists in the selective deposition of coatings, depending on the functionality of the areas, i.e. contact with GDL or sealing and atmosphere. A tremendous amount of possibilities is currently explored (e.g. [54, 55]). As a matter of fact, a full environment-dependent characterisation of the oxidation behaviour of bare standard MIC SOFC alloys is not available from the literature, even for the simplest practical approaches, such as Wagner’s law. Furthermore, almost all investigations on coatings are carried out at a single temperature, in order to quickly identify the best solutions. While such experiments can provide insights into the physical processes, which is of course the most important aim, their value in the present context remains limited.

[Figure 3 about here.]

The simulation of the contribution of metallic components to the degradation requires numerous assumptions and oversimplifications. All issues related to GDLs and contacting interlayers is ignored, despite their importance. Compiled data are overall sufficient to calibrate a temperature dependent Wagner law, coupled to an equivalent conductivity of the oxide scale. Here, a coarse distinction between air, hydrogen or methane as fuel, is at best achievable. This is an approach very similar to that described in [23], though the database is now extended. The present simplified approach does not rigorously describe the dynamically evolving, multilayered system that constitutes an oxide scale on top of an coated or uncoated MIC.

Wagner’s oxidation theory yields a parabolic evolution, as it assumes that diffusion of species in the dense oxide scale controls the weight gain during exposure.

$$\frac{\partial h_{\mathcal{D}MICg}^2}{\partial t} = k_{m_g} \exp\left(\frac{E_{a\mathcal{D}MICg}}{RT_s}\right) \quad (31)$$

Most of the data from the literature provides k_g , which is easier to measure continuously than k_m . If the exact composition of the oxide layer(s) is known, which is seldom the case, the conversion to k_m is straightforward:

$$k_{m_g} = \left(\frac{M_{ox_g}}{(3/2)M_{O_2}\rho_{ox_g}}\right)^2 k_{g_g} \quad (32)$$

In the present work, $\rho_{Cr_2O_3}$ is used if required. A classical relation can be used for the overall temperature-dependent conductivity of the whole oxide scale, which enables the calculation of the ASR of the oxide

scale:

$$\sigma_{\text{MIC}_g}^e = k_{o\text{MIC}_g} \exp\left(-\frac{E_{a\text{MIC}_g}}{RT_s}\right) \quad (33)$$

$$\text{ASR}_{\text{MIC}_g} = \frac{h_{\mathcal{D}\text{MIC}_g}}{\sigma_{\text{MIC}_g}^e} \quad (34)$$

Pre-exponential factors and activation energies are estimated from the compiled data using gPROMS [26]. The procedure is identical to that used in Part I [25]. The optimal values of the parameters, used for the simulation of degradation, are listed in Table 1. Figure 3 depicts some collected parabolic growth rates, used for the calculation of activation energies, and pre-exponential factors on the fuel side (ZMG232L). On the air side (Crofer22), pre-exponential factors are computed from available thickness measurements [56]. Predicted ASR are displayed in Figure 4. The two surfaces for Crofer22 in air express the discrepancy in measured thicknesses of the oxide scale [56].

[Figure 4 about here.]

In general, the initial electrical resistance of coated MICs is initially higher than that of uncoated ones, but then remains fairly stable in the viable cases. An evolution relation valid at 1073 K only for $\text{Mn}_{1.5}\text{Co}_{1.5}\text{O}_4$ is used in the present work [56].

[Table 1 about here.]

2.2.2 Electrolyte phase

The causes of the observed decrease in ionic conductivity of YSZ are still controversial. Studies show that the ionic conductivity of compositions with higher amounts of yttrium tends to be more stable during aging. The evidence that neither parabolic nor exponential relations can represent the observed evolution over an extended time period has motivated the first modelling attempts. Vlasov et al. [57] have proposed a two-phase solid electrolyte aging model, based on the evolution of the number of nucleation sites, followed by growth by diffusion of the new phase of lower ionic conductivity. An additional relation has been then used to compute the effective ionic conductivity. While this model reproduces trends, detailed investigations highlighted that its physical basis does not fully reflect the reality.

The most common explanation relies on the possibility of a progressive transformation of the initial cubic phase into the tetragonal one [58–61]. In contrast, Kondoh et al. [15,62] postulated that the ionic conductivity

is affected at comparatively low temperature (1473K) by short-range ordering of oxide ion vacancies around Zr ions, resulting in a relaxation of the anisotropy of the lattice distortion caused by the yttrium dopant. Therefore, in a simplified view, Zr ions progressively trap, though not definitely, oxygen vacancies responsible for the ionic conduction. Measurable consequences include a decrease in ionic conductivity, and an increase of the activation energy. However, the recovery of the properties can occur after annealing at high temperature (approximately 1573K). The explanation of Haering et al. [63] is somewhat similar, accounting for the transformation of defect associates, $[Y'_{Zr}-V_{\ddot{O}}]$ and $[Y'_{Zr}-V_{\ddot{O}}-Y'_{Zr}]$. Aging seems to promote tripoles, which are more stable than dipoles. The reason for this trend is however not identified. Formation of glassy phases from impurities at the grain boundaries is another possible degradation mechanism, but has not been reported, at least at high temperature [15, 61, 62].

Most of the studies have been performed on pure materials in air, which is not the case of the electrolyte and ionic-conducting phases in the electrodes, due to the sintering of the cell. In these conditions, a concentration around 1 wt.% of Ni in YSZ is not unlikely [64]. Yet, Coors et al. [65] have observed for instance a quick drop of the ionic conductivity of NiO-containing YSZ, followed by stabilisation at a significantly lower level than for pure YSZ. Alternatively, Appel et al. [60] have explored Mn-doping to increase the stability of the ionic conductivity. This kind of data remains insufficient in amount for modelling purposes. Therefore, data on pure materials is believed sufficient for a preliminary study.

Data is mainly available for temperatures around 1273K, which is the typical operating temperature of electrolyte-supported cells. Data at lower temperature remains comparatively sparse, though sufficient to propose an empirical relation for the relative decrease of ionic conductivity during aging, valid for $t_o > 0$.

$$\xi_{\mathcal{D}_{elect}} = \frac{\sigma_{ion}^e - \sigma_{ion}^e(t_o)}{\sigma_{ion}^e(t_o)} \quad (35)$$

$$\xi_{\mathcal{D}_{elect}\infty} = k_{o\mathcal{D}_{elect}\infty} \exp \left[-\frac{E_{a\mathcal{D}_{elect}\infty}}{R} \left(\frac{1}{T_s} - \frac{1}{T_{ref}} \right) \right] \quad (36)$$

$$\xi_{\mathcal{D}_{elect}} \frac{\partial \xi_{\mathcal{D}_{elect}}}{\partial t} = \max \left[0, k_{o\mathcal{D}_{elect}} \exp \left[-\frac{E_{a\mathcal{D}_{elect}}}{R} \left(\frac{1}{T_s} - \frac{1}{T_{ref}} \right) \right] \frac{\xi_{\mathcal{D}_{elect}} - \xi_{\mathcal{D}_{elect}\infty}}{\xi_{\mathcal{D}_{elect}}(t_o) - \xi_{\mathcal{D}_{elect}\infty}} \right] \quad (37)$$

The parameters in $\xi_{\mathcal{D}_{elect}\infty}$ serve to fit the final value at a given temperature, while $k_{o\mathcal{D}_{elect}}$ and $E_{a\mathcal{D}_{elect}}$ control the rate of the drop. The parameter estimation capabilities of gPROMS [26] are used to obtain coarse

estimates of $k_{o_{\mathcal{D}_{elect}}}$, $k_{o_{\mathcal{D}_{elect}\infty}}$, $E_{a_{\mathcal{D}_{elect}}}$ and $E_{a_{\mathcal{D}_{elect}\infty}}$ on selected sets of experimental data from the literature (see Figure 5). A particular concern in the choice of Eq.37 is to prevent inconsistent behaviours, when implemented in SRU/stack models. Indeed, recovery [15] should not occur within the typical temperature range of IT-SOFC. Eq.37 is indifferently used to predict the local relative loss in conductivity of the electrolyte and coupled to a percolation model (see Appendix A.2) of electrolyte phases in the composite electrodes.

[Figure 5 about here.]

2.2.3 Anode

On the Ni-YSZ anode side, sulfur poisoning and carbon deposition on the Ni catalyst are known issues occurring in field conditions, where the use of pure hydrogen is not usually of interest. It is believed that impurities from the raw materials of SOFC, especially SiO from either NiO or YSZ starting powders, segregate to the Ni/YSZ interfaces and promote the formation of glassy phases at the interfaces between the constituents [64, 66]. Liu et al. [64] further attempted to discuss degradation in regard of the dependence of the wettability of the glassy phase on the steam content of the anode gas. Both loss and coarsening of nickel observed in SOFC anode [3, 18, 19, 67, 68] are expected to induce a decrease of the TPBL and effective conductivities in the composite anode. The latter process has already been included in button cell models. A modelling approach similar to that of Tanasini et al. [18] is adopted in the present study.

A clarification on the reason for the assignment of contamination and coarsening on either anode or cathode side is needed. On the one hand, the detrimental effects of sulfur or carbon deposition can be hindered to some extent, while chromium evaporation arises from internal sources from the stack or system [10]. On the other hand, even though coarsening of the cathode microstructure has been reported, LSM-YSZ composites seem less sensitive [69]. This has been ascertained during in-house studies [18]. However, the formation of undesirable phase might deplete the LSM of its constituents, hence affect its resistance against particle coarsening [70]. Therefore, implementation of microstructural changes and pollution phenomena are respectively illustrated in the anode and cathode. This choice is arbitrary, not implying that these mechanisms are the most relevant contributions in any case. An adaptation of the modelling approach is required, depending on the foreseen application of the SOFC stack.

The present modelling approach consists in coupling percolation to composite electrode models, to relate the evolution of the TPBL to the growth of nickel particles. This approach suffers some inconsistencies and limitations. The formally required reference state is neglected here, since particles are assumed to be continuously re-arranged at each time. For instance, the insertion in the percolation model of the effect of

nickel loss from a quick estimation based on thermodynamic considerations [68] entails a negligible decrease of TPBL. This does not necessarily reflect the reality, as localised depletion at the active sites can likely cause noticeable degradation. Furthermore, simple percolation models [21, 71] are limited in terms of particle size distribution or shape. The model of Chen et al. [72] is a first step towards more reliable and technologically-useful predictions.

The detrimental effect of a change in shape and size of the nickel particles is not restricted to a reduction of the TPBL. In the case of internal methane reforming, sulfur poisoning and coking limits are also affected [73]. A quantitative and exhaustive knowledge of these phenomena is crucial for the durability of technological SOFC stacks.

The specificity of the growth of nickel particles in SOFC anodes, compared with that in catalysts, is interaction between the nickel particles and the YSZ backbone, as handled in the physical model proposed by Vassen et al. [74]. Quantitative estimation of Ni particle growth in SOFC is time-consuming and specific to each anode [18, 19, 67, 75], which results in a lack of data on the detailed effects of temperature and steam partial pressure. However, the development of an empirical relation can benefit from research on nickel catalysts, where a strong dependence on both temperature and steam partial pressure [73] is well established. Different regimes are usually observed. The proposed underlying processes are either Ostwald ripening or particle migration.

[Figure 6 about here.]

A simultaneous close match to the few compiled data is illusory, as depicted in Figure 6. The proposed relation, which is a simplification of the model of Vassen et al. [74], adapted for the effect of steam in fuel [73], is able to reproduce trends. It fails at very low H_2/H_2O ratios, however, as the dominant mechanisms likely differs, depending on the conditions.

$$r_{gNi}^2 \frac{\partial r_{gNi}}{\partial t} = k_{oD_{an}} \exp \left[-\frac{E_{aD_{an}}}{R} \left(\frac{1}{T_s} - \frac{1}{T_{ref}} \right) \right] \frac{x_{H_2O}}{x_{H_2}^{0.5}} \frac{r_{gNi\infty}^3 - r_{gNi}^3}{r_{gNi\infty}^3 - r_{gNi}(0)^3} \quad (38)$$

Eq.38 is used in a dimensionless form for the parameter estimation, to enable an averaged calibration on the few experimental data. Hence, the maximum size of the nickel particle is a ratio, instead of a real microstructure-dependent parameter. Due to the high uncertainty on the exact influence of the gas composition on the nickel particle coarsening and the comparatively narrow functional thickness of the anode, steam and hydrogen computed at the anode/electrolyte interface are used, i.e. particle coarsening is not distributed through the thickness of the anode. The reduction of TPBL ensuing the coarsening of the

nickel particle is computed by a classical percolation model (see Appendix A.2). Table 1 lists the values of the parameters used for the simulations.

A comment on the implementation of nickel particle coarsening in simplified modelling approaches, based on an interfacial, instead of a distributed description of the electrochemical processes in the anode, is worthwhile. The application of a linear relationship between resistance and TPBL, acknowledged in pattern anode (see Part I), is not necessarily reported at the electrode scale. Costamagna et al. [21] have provided the dependence of the polarisation resistance of a composite electrode on its TPBL for different limiting cases. Our simulations clearly showed that our study case lies in the range of a thick electrode, that is, a dependence to the square-root. ξ_{TPB} (see Part I) has been set correspondingly for the comparison between the one-dimensional and REV models. Finally, a simple assessment of the risks of reoxidation is performed [10, 23, 76].

2.2.4 Cathode

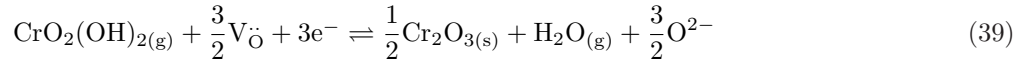
The nature of possible causes of degradation in Ni-YSZ anodes and LSM-YSZ cathodes have similarities. In the present work, emphasis is placed on chromium deposition and formation of LZO and/or SZO at the LSM/YSZ interfaces. The former is an issue to solve in technological IT-SOFC stacks, while the latter represents an intrinsic limitation of IT-SOFC based on LSM-YSZ cathodes.

The prediction of the detrimental effect of chromium contamination in a stack requires the description of the processes involved in (i) the evaporation of chromium species from the oxide scale on top of the metallic components, (ii) subsequent transport by the gas carrier, and (iii) deposition mechanisms at the TPB. The first two phenomena are simplified in the present study to the calculation of the partial pressure of volatile chromium species in equilibrium with the oxide scale on the MIC. The considered volatile chromium species are restricted to $\text{CrO}_2(\text{OH})_{2(\text{g})}$, as SOFC stacks are usually fed with ambient air or compressed air, which still contains some humidity [3]. The use of synthetic air for large or short stacks is uncommon and of little interest for the simulation of field conditions. Discrepancies in thermodynamic data induce errors of orders of magnitude for the calculation of the equilibrium partial pressure of volatile species [35, 77]. However, trends such as the detrimental effect of air humidity [9], which varies during the service of a SOFC stack, are correctly captured.

There has been considerable debate on the nature of the degradation processes leading to chromium contamination. Jiang et al. [78] have explained the trends observed in their deposition experiments by the role of Mn^{2+} ions, generated during polarisation. These researchers have discussed the detrimental effects

of both deposited and volatile Cr species on the ORR, in the view of altered elementary steps [79]. Another possibility is electrochemical reduction to Cr_2O_3 from $\text{CrO}_2(\text{OH})_2$ volatile species at the TPB [80]. A well established parameter, which further complicates the situation, is the choice of an electrolyte and/or ion-conducting phase material [81]. From a technological prospect, the resistance of LSM-SDC composites toward chromium contamination is higher than that of LSM-YSZ, which, in turn, exceeds that of single LSM cathodes [82]. The degradation rate depends on current density and thickness of the functional layer. Qualitatively, scanning (SEM) and transmission (TEM) electron microscopy and wavelength-dispersive X-ray (WDX) investigation [11, 80, 82] highlights different patterns of deposition in cathodes made of a LSM-YSZ composite functional layer and LSM contacting layer, depending on polarisation [8]. Chromium species deposit preferentially in the LSM-YSZ functional layer, close to the active sites, or uniformly, in the current collecting layer, under polarisation or at open-circuit voltage (OCV), respectively.

The detrimental effect of chromium deposition should be rigorously considered in the view of altered elementary steps and pathways in the overall oxygen reduction rate (ORR) [79, 83]. All reviews on studies on ORR [84, 85] reveal disagreements among reported results and suggested explanations. Therefore, the simplest scenario of full blocking is considered here, along with a single electrochemically driven deposition process (reaction 39). The rate of deposition can be expressed in a Butler-Volmer form, the derivation of which is provided in Appendix A.1. The modelling approach pursued here is meant to capture, to some extent, the effect of humidity in the air feed on the cathode side. A word of caution should be taken on the range of applicability of the model. As pointed out by Nielsen et al. [86], another phenomenon related to humidity, the nature of which is not yet clarified, causes a significant degradation of LSM-YSZ cathodes. Similar to chromium contamination, extended periods at open-circuit voltage do not induce a detrimental effect. Furthermore, partial recovery occurs after switching to dry air. The resistance of cathodes based on LSCF contrasts with that made of LSM-YSZ.



$$j_{\mathcal{D}_{cath}} = i_{o_{\mathcal{D}_{cath}}} x_{\text{CrO}_2(\text{OH})_2}^{1/2} x_{\text{H}_2\text{O}}^{1/2} 2 \sinh \left(\frac{1}{2} \frac{F\eta_{cath}}{RT_s} \right) \quad (40)$$

The deposition rate is dependent on the local conditions and assigned to the local overpotential, which varies through the thickness of the cathode. The contribution of the resulting current $j_{\mathcal{D}_{cath}}$ to the total one j_{tot} is very low and neglected in the calculations. The initial TPBL is computed using the same simple percolation

model than for the anode (see Appendix A.2). Considerable simplification is required to further compute the amount of effective TPB blocked. First, the exchange current density must be estimated. Horita et al. [11] provide quantitative data for LSM/GDC, which enables a first estimate of the deposited mass of Cr_2O_3 . The number of atoms deposited can be estimated from Eq.40 and information in Table 2.

$$\mathcal{N}_{at} = t \cdot \frac{\mathcal{N}_a A_{\text{TPB}}}{3F} i_{o_{\mathcal{D}_{cath}}} x_{\text{CrO}_2(\text{OH})_2}^{1/2} x_{\text{H}_2\text{O}}^{1/2} 2 \sinh\left(\frac{1}{2} \frac{F\eta}{RT_s}\right) \quad (41)$$

[Table 2 about here.]

Second, the extension of the TPB remains a question in the clarification of the ORR [85]. We assume a uniform and invariable value of $w_{\text{TPB}} = 150$ nm, after activation, estimated by Jiang et al. [87], even though this quantity is believed to depend on the local conditions. Therefore, all activation processes are neglected in the present study. Third, the thickness of the chromium deposit cannot grow indefinitely. The thickness h_{TPB} observed by Konyshева et al. [8] is around 18-60 nm in the presumably active zone. All these geometrical assumptions are depicted in Figure 7. In the case recovery is not allowed, the time and the thickness position-dependent effective TPB area can be computed by

$$\frac{1}{A_{\text{TPB}\mathcal{D}_{cath}}} \frac{\partial A_{\text{TPB}\mathcal{D}_{cath}}}{\partial t} = - \max\left[0, \frac{1}{2F} \frac{M_{\text{Cr}_2\text{O}_3}}{\rho_{\text{Cr}_2\text{O}_3} h_{\text{TPB}\mathcal{D}_{cath}}} j_{\mathcal{D}_{cath}}\right] \text{ in } \mathcal{R}_5 \quad (42)$$

Unlike the degradation mechanisms discussed in the previous sections, which are not discretised in the z -direction, in particular due to the isothermal nature of the electrochemical model, the dependence on the local overpotential in Eq.42 enforces a thickness-dependent blocking of the TPB. In the analysis of the results (see Section 3), the time to block the active sites at the interface between the cathode and the electrolyte Γ_5 corresponds arbitrarily to the the time at which 5% of $A_{\text{TPB}\mathcal{D}_{cath}}$ remains available at this location.

Undesirable phases such as LZO and/or SZO are known to possibly grow during the sintering of the manufacturing step [88], which have yielded optimised sintering procedures and LSM compositions. A recent study of the LSM/YSZ interface in button cell cathodes by Liu and associates [4, 5] highlights the possibility of such formation during operation, depending on oxygen activity. Quantitative rate relations for the present study could not be deduced from collected experimental data [89, 90]. A comparison between the critical oxygen partial pressure estimated by Liu et al. [5] and the actual one,

$$\eta_{cath} = \frac{RT_s}{4F} \ln \frac{x_{\text{O}_2(g)}}{x_{\text{O}_2(\text{LSM/YSZ})}} \quad (43)$$

can serve as an estimate of the risks, in a similar way to anode reoxidation [10, 23, 76].

[Figure 7 about here.]

3 Results and discussion

3.1 Validity of the one-dimensional approach

The relevance of the one-dimensional simplification for the description of the local electrochemical behaviour in a SRU depends on the GDL solution. An adequate geometry and selection of materials balance the effects of current constriction and depletion of reactants in the active zone of the porous electrodes [22], to maximise the electrochemical performance. Detrimental chemical interactions between the materials and structural instabilities have to be prevented during long-term operation. The GDL system must further fulfil the requirements on pressure drops. A one-dimensional description cannot provide comprehensive guidance in the design of the GDL system, but is currently needed, for computing time reasons, for dynamic simulations of a SRU/stack. Its limitations for the modelling of the local performance and degradation must be identified, to avoid misleading conclusions.

The one dimensional model calibrated in Part I is tested against two typical GDL solutions, the generic geometry of which is depicted in Figure 1. The difference lies in the coverage of the PEN by the GDLs, and the porosity of the latter. The first case considers a dense material in \mathcal{R}_2 and \mathcal{R}_6 covering 25% of the electrode surface Γ_3, Γ_6 . An increase of the coverage detrimentally affects the performance, due to the depletion of oxygen under the ribs, while a decrease alters the distribution of the electronic current [22]. The second case comprises a porous material in \mathcal{R}_2 and \mathcal{R}_6 , of identical properties than the electrodes, apart from a lower tortuosity of 2. The coverage is 50%. Therefore, the electronic conductivities in \mathcal{R}_2 and \mathcal{R}_6 are not corrected for the porosity. Steam-methane reforming and water-gas shift reactions do not occur in the porous anode GDL. A correction term for current constriction based on an analytical solution from Nisançioğlu [91] is implemented in the one-dimensional model.

The one-dimensional electrochemical model for SRU simulations described in Part I does not use a composite electrode model of the anode, for computing time reasons. The value of $k_{o_{an}}$ (Eq.29) is set to ensure a similar anode overpotential at the nominal point, in a one-dimensional description of the approach described in Section 2.1 and in the one-dimensional model calibrated in Part I. The test aims at assessing the suitability of the one-dimensional model for performance modelling and for the correct prediction of the degradation. The context is the simulation of the behaviour of a SRU, not the design of the GDL system.

[Figure 8 about here.]

Figure 8 depicts the local current-voltage (IV) characteristics predicted by the three electrochemical models. The SRU voltage, local temperature and gas composition at the different locations are assigned from computations with a two-dimensional model of the SRU [92] displayed in Figure 1a, coupled to the one-dimensional electrochemical model. The SRU is embedded in a stack fed with partially pre-reformed methane. These conditions are similar to those studied in Part I and summarised in Table 3. Owing to the two lateral fuel manifolds, and the electrochemically inactive introduction zone where the steam-methane reforming reaction takes place in the anode support, the anode gas is almost completely reformed, when it reaches the active area, on the symmetry line. The high air ratio required for the cooling of the stack ensures a fairly uniform oxygen molar fraction all over the active area. The depletion of fuel on the fuel downstream zone C induces a local decrease of the current density (light gray in Figure 8). The strong so-called activation effect at the air outlet, in counter-flow is due to the significant local rise of the temperature, of approximately 130 K during the IV characterisation. The evolution of the distribution of the current density on the symmetry line can be deduced from the three local characteristics. In counter-flow, the combination of high temperature and reactant-rich fuel at the fuel inlet promotes a high current density. In contrast, in co-flow, the trade-off between high temperature (air outlet) and reactant-rich fuel (air inlet) drives the location of the maximum current density. The largest absolute discrepancy between the predictions of the models is at the highest current densities. The one-dimensional model and the REV model with a dense GDL consistently predict the best, respectively lowest performance. The simplification of the anode composite electrode model does not result in an unacceptable loss of accuracy, despite the addition of the temperature dependence of the conductivities of the ionic and electronic phases. The analytical relation for current constriction from Nisançoglu [91] mostly underestimates the loss of performance due to geometry, as it does not correct for neither the effects of gas depletion under the GDL, nor the uneven distribution of the local overpotential.

[Figure 9 about here.]

[Table 3 about here.]

[Figure 10 about here.]

Figure 8 shows that a one-dimensional model can be modified to enable reliable performance and structural simulations of a SRU. The degradation phenomena considered in the present study depend on temperature, gas composition and overpotential. Figure 9 depicts the local and independent evolution of the

relative ASR and overpotential of the anode and cathode at locations A, B, C, indicated in Figure 1, during operation at the nominal point (see Figure 8), the potential of the SRU being kept constant. The evolution of the ASR of the MICs and electrolyte can be observed directly in Figure 4 and Figure 5, and is therefore not shown. In a real SRU, the temperature at each location is not constant, due to the redistribution of the current density. This coupling is not included here. A coated MIC and compressed air ($x_{H_2O_{cath}}=0.001$ [4]) are assumed. The characteristic patterns of the degradation phenomena and the interactions are best seen in the evolution of the relative ASR and overpotential, respectively. The ASR of the anode and electrolyte (not depicted) tend to a final value, after different time, depending on the temperature and H_2 and H_2O molar fractions. The magnitude of the ASR of the electrolyte is similar to that of the anode and follows the same pattern. The aforementioned coupling between temperature and current density in a SRU may somewhat alter this observation, since $r_{g_{Ni\infty}}$ is fixed, whereas the final loss of ionic conductivity of the electrolyte $\xi_{\mathcal{D}_{elect}\infty}$ depends on temperature. At the air inlet, their contribution to the ASR is less affected during operation, due to the low temperature. Both phenomena cannot alone lead to the end of the life of a stack. In contrast, the rate of degradation of the ASR of the cathode monotonically increases with respect to time. The different shapes and characteristic times of the degradation phenomena cause an evolution of their relative contribution to the total losses. As shown in the lower plots of Figure 9, the first significant increases of the ASR of the anode and of the electrolyte (not depicted) induce a quick drop of the current density, inducing a slight decrease of the cathode overpotential, which is more pronounced with the one-dimensional model. The degradation rate of the cathode can be therefore first attenuated, but then dominates. Despite the progressive decrease of the current density, the overpotential of the cathode continues to increase. In contrast, the contributions of the anode and electrolyte monotonically decrease once the maximum value is reached. All simulations depicted in Figure 9 predict the absence of formation of zirconates, since during operation at constant potential, the molar fraction of oxygen at Γ_5 increases during operation as the current density decreases, sufficiently to compensate the increase of the cathode overpotential. The predictions of the REV model with a dense or porous GDL are similar. In comparison, the one-dimensional model slightly underestimates the degradation, but correctly captures the trend. The lack of data for a comprehensive modelling of the degradation phenomena is believed to induce much more severe possible misleading predictions, as discussed further in Section 3.3.

The observation of the distribution of gas species, current density and overpotential computed by the REV model provides insights into the reasons for the acceptable limitations of the one-dimensional description. These fields are shown in Figure 10 after 500 h at location A in Figure 1a. High local electronic current

densities occur in the cathode. The non-uniformity is more pronounced for a dense, than for a porous GDL and higher coverage. In comparison, the profiles of the ionic current density (not shown) and the cathode and anode overpotentials (lowest graphs) at the interfaces between the electrolyte and the electrodes are more even. Yet, in the present modelling approach, the local overpotential, rather than the current density is assumed to predominantly drive the deposition of Cr and risk of formation of LZO/SZO phases in the LSM-YSZ cathode. The model cannot handle the temperature inhomogeneities that may arise from very high local current densities and affect, in turn, the Cr-deposition process and risk of formation of zirconate.

The minimum oxygen molar fraction of approximately 0.1, located under the ribs, be it dense or porous is lower than in the channel, whereas the local overpotential at the electrolyte/cathode interface is slightly higher under the rib. Both trends favour the formation of LZO/SZO, and underscore the need for investigations (see Section 3.3). The distribution of the gas species on the anode side does not strongly depend on the nature of the GDL system. The thickness and higher electronic conductivity of the anode support alleviate the geometrical effects. This uniformity, together with that of the overpotential, explains the limited differences observed in the degradation rates of the anode predicted by the one-dimensional and REV models. The higher molar fraction of methane at the edge of the active area, near the fuel inlet, causes a slightly less even distribution of the gas species in the anode.

3.2 Comparison against experimental data

The available data on long-term operation of short stacks exhibits a large scatter, due to the interplay of the different possible causes of the degradation, which does not allow the consistent calibration of the selection of degradation models included in this study. Ideally, the degradation models should be validated against dedicated experiments, and their behaviour and interaction verified against short stack experiments. Such a procedure is crucial for the relevance of accelerated testing, or to verify if partial recovery of the performance [4, 15], or if unexpected detrimental couplings are possible.

[Figure 11 about here.]

Figure 11 compares data on the degradation of short stacks from de Haart et al. [70, 93] with simulations with the one-dimensional electrochemical model alone, without any specific adjustment of the model parameters. Fuel outlet conditions are used for the calculations, and an uniform current density and temperature are assumed. The LSM-YSZ cathode tested by de Haart et al. [93] has a better performance than that used for the calibration of the model in Part I. The results are therefore presented as the relative loss of

voltage during operation at different current densities and fuel utilisations. De Haart et al. [93] have not succeeded in assigning unambiguously phenomena to each degradation pattern. Therefore, the comparison and explanation for the discrepancies are tentative.

The model, with a steam molar fraction of 0.001 in the cathode gas and coated MIC, reproduces the patterns of the experimental evolution of the current density for all current densities and fuel utilisations, and predicts relative decays that fall within the scatter in the data. A possible reason for the underestimation of the initial decay is the calibration of the loss of ionic conductivity (Eq. 37) on data for pure 8YSZ. The presence of Ni and Mn from the anode, respectively cathode are known to amplify the loss. The model also complies with the weak dependence of the degradation on the fuel utilisation and fuel, either wetted hydrogen or reformed methane. Furthermore, cells with a LSCF cathode tested at 973 K in the same setup, exhibit a less pronounced initial decay, as would be predicted by the model.

Post-test investigations on the aforementioned experiments are available for the LSM-YSZ cathode [70]. These confirm the formation of a Mn,Cr,Cu spinel, copper being used in the contacting layer, and a subsequent coarsening of the cathode microstructure. Unlike the assumption in the model, an apparent blocking of the whole active layer does not completely prevent the ORR. The quantification of Cr deposited in the functional cathode and current collection somewhat contradicts the model assumptions. A plateau is reached, despite the progression of the degradation, and a clear dependence on the current density is not confirmed [94]. Part of the chromium detected in the quantifications comes from the current collecting layers, the deposition process in which is different than in the functional LSM-YSZ cathode [11]. The assumption of a single electrochemical deposition process in the LSM-YSZ cathode, corrected for the simultaneous chemical deposition [8,11], cannot explain and reproduce all the experimental data. The knowledge of the transport and deposition phenomena within the cathode is paramount for correct and meaningful predictions.

The modelling approach proposed in the present study, based on detailed investigations found in the literature correctly reproduces the overall trend of the degradation in anode-supported cell with a LSM-YSZ cathode. The simplifications, due to modelling difficulties or lack of clarification on the processes, hinder a complete agreement with the detailed post-test analysis.

3.3 Effect of operating conditions and cathode thickness

The knowledge of the underlying phenomena of the degradation provides guidance in mitigation strategies. The degradation models developed in the present study do not provide a rigorous basis for improvement of the microstructure, because of the simple percolation model and semi-empirical nature of most of the

contributions. It can however predict, for certain dominant degradation phenomena, consistent dependences on temperature, overpotential, alternatively current density, and gas compositions. This capability allows detecting design and operation-induced accelerated local degradation rates. Before implementation in a SRU model, the behaviour of the electrochemical model, including the degradation phenomena, has to be investigated further.

The severity of the degradation of the anode is determined by $r_{gNi\infty}$. Despite its apparent simple physical meaning, $r_{gNi\infty}$ must be set empirically, due to the lack of knowledge on the nature of the interaction between the Ni and the YSZ networks. It is believed that $r_{gNi\infty}$ depends, at least, on temperature. Notwithstanding the imprecise calibration of Eq.38, the determination of the time over which nickel coarsening contributes to the observed degradation rate can assist the analysis of experimental data. The time to reach $r_{gNi\infty}$ varies from 1000 h to 10000 h, depending on the conditions: high temperature and low hydrogen content promote the coarsening of the nickel, as depicted in Figure 12. The relative definitive increase in the ASR follows the opposite trend. The apparent degradation rate of the ASR, measured over different time periods, is a combination of both and does not depend monotonically on temperature at hydrogen molar fractions around 0.3. Figure 12 can be used during the design and setting of the operating conditions of a stack, to fulfill requirements on the performance, at the end of the target lifetime.

[Figure 12 about here.]

Figure 13a illustrate the progressive blocking of the active sites by the Cr_2O_3 deposit, for a constant cathode overpotential and assuming compressed air ($x_{H_2O}=0.001$ [4]). Simulations for bubbled air ($x_{H_2O}=0.03$, $j=0.5$ Acm⁻², 1073 K) yield a similar behaviour, but much shorter times, around 3500 h, to deactivate interface Γ_5 (Figure 2). We emphasise that the validity of the model is not ensured in the latter conditions, as additional phenomena, the nature of which is not yet clarified [86] affect the performance of LSM-YSZ cathodes. Due to the assumed uniform distribution of $CrO_2(OH)_{2(g)}$ in the cathode, the local overpotential solely drives the deposition process. The extension of the active zone resulting from the calibration on experimental IV characteristics (Part I), around 20 μm is likely slightly overestimated. The contribution to the losses in the inactive layer growing from the interface towards the gas channel, after 12500 h in Figure 13a is ionic conduction in the YSZ network.

[Figure 13 about here.]

Owing to the progressive blocking of the active sites in the cathode due to chromium deposition, straightforward mitigation approaches to test are the increase of the thickness of the cathode, and the increase of

the TPBL by improvements of the microstructure. The study from Konyshva et al. [82] on button cells shows a clear benefit of the increase of the thickness of the functional cathode, which is not confirmed by the short stack test of Menzler et al. [70]. Figure 13 shows the results of simulations, performed in similar conditions to those in the experiments of Menzler et al. [70]: the effect of the thickness and different assumptions for the calculation of the concentration of $\text{CrO}_2(\text{OH})_{2(\text{g})}$ are tested with the one-dimensional model alone, including all degradation phenomena, at 973 K and 0.3 Acm^{-2} , and 1073 K and 0.5 Acm^{-2} . The difference in the investigated thickness range is due to the small overestimation of the extension of the active zone in the model and the difference in performance of the LSM-YSZ cathodes used by Menzler et al. [70] and Part I. The cathode of $20 \mu\text{m}$ exhibits the strongest degradation, which is amplified by its higher overpotential. The effect of the increase of the thickness from $50 \mu\text{m}$ to $100 \mu\text{m}$ is less evident and affected by the assumption on the calculation of $\text{CrO}_2(\text{OH})_{2(\text{g})}$. In the case the oxygen molar fraction in the gas channel is used, the potential of the $50 \mu\text{m}$ cathode remains higher during the whole investigated period, owing to its slightly lower overpotential. If an uneven distribution of $\text{CrO}_2(\text{OH})_{2(\text{g})}$ is computed from the oxygen molar fraction within the cathode, but the related deposition process neglected, the potential of the cell with a $100 \mu\text{m}$ cathode exceeds that of the $50 \mu\text{m}$ after approximately 7000 h at 1073 K and 0.5 Acm^{-2} , due to the lower $\text{CrO}_2(\text{OH})_{2(\text{g})}$ in the active zone. Simulations performed at 973 K exhibit the same trend. The opposite conclusion on the benefit of increasing the thickness on the long-term performance shows the need for model improvements and accurate experimental data. In reality, the presence of a contacting layer that acts as a Cr getter complicates the situation, but alternatively provides possibilities to alleviate the chromium contamination of the functional LSM-YSZ cathode.

Figure 13b provides insights into the interactions between the phenomena implemented on the cathode side. At constant current density, the minimum oxygen molar fraction does not progressively increase, whereas the cathode overpotential becomes dominant as operation proceeds. This promotes the formation of LZO/SZO phases. The critical times are indicated in Figure 13b. In reality, an acceleration of the degradation is expected. Despite the higher current density and thermodynamic considerations, the conditions of higher temperature and current density are favourable. The overpotential predominantly governs the risk of formation of LZO/SZO, which is expected to occur first in the $20 \mu\text{m}$ cathode. The difference in time between the $50 \mu\text{m}$ thick and $100 \mu\text{m}$ thick cathode arises from the slightly lower oxygen molar fraction at the interface Γ_5 , and marginally higher overpotential in the latter.

The deposition of coatings on the MICs mitigates the evaporation rate of chromium species within the SRU. This affects the modelled dependence on temperature of the degradation due to chromium poisoning

of the LSM-YSZ cathode. A first assessment of the benefit provided by MIC coatings consists in calculating $x_{CrO_2(OH)_{2(g)}}$ from either local (in the gas channel) or inlet conditions. The latter case approximates an uncoated gas manifold, which is assumed to deliver compressed air at 973 K. The use of data for the equilibrium partial pressure of $CrO_2(OH)_{2(g)}$ on pure Cr_2O_3 is a coarse worst case, as in reality, bulk alloying of Crofer22 [32], for instance, promotes the formation of a $(Cr, Mn)_3O_4$ spinel on top of the oxide scale. The equilibrium partial pressure of volatile chromium species on the latter materials is significantly lower [77], even though the scatter in the data covers several orders of magnitude [9]. Volatilisation limited by mass transport through the boundary layers further reduces the eventual value in the cathode.

Figure 14 depicts the results without (a) and with (b) a MIC coating, provided by the one-dimensional model alone. Simulations are carried out until all active sites at the interface Γ_5 are blocked, which enforces a comparable extent of the degradation in both cases, as reflected in the identical relative loss of ASR $\Delta ASR/ASR_o$. The final relative increase of the ASR is more severe at lower electrode overpotentials. This is due to the slightly more even distribution of the local overpotential, hence of deposited Cr within the cathode, for lower values. As expected, degradation rates are in contrast less severe at lower overpotential. A comparison of the time to block the active sites at the interface Γ_5 shows the opposite temperature dependences in the case of a coated or not MIC. In the first case, the temperature dependence of Eq.40 which neglects that of the exchange current density $i_{o_{D_{cath}}}$ dominates and induces a decrease of the degradation rate with respect to temperature. In the case of an uncoated MIC, the equilibrium partial pressure of $CrO_2(OH)_{2(g)}$ increases with respect to temperature and promotes the deposition process.

[Figure 14 about here.]

Figure 14 provides insights into the effects of temperature and overpotential on the chromium poisoning of the cathode, but is of limited technological relevance. Figure 15 provides the value and rate of the relative increase of the ASR, after 3000 h of operation, for the case of a coated MIC, to enable a first assessment of the distribution of the degradation in a SOFC stack. As expected from the aforementioned observations, operation at the highest temperature and lowest overpotential yields the lowest degradation. The influence of the temperature for a fixed cathode overpotential originates again from the distribution of the overpotential within the thickness of the cathode, and the temperature-dependence of Eq.40. The implementation of a temperature-dependent exchange current density $i_{o_{D_{cath}}}$ might lead to an opposite conclusion. Repeating the experiment of Horita et al. [11] at different temperatures would allow for calibration.

[Figure 15 about here.]

A functional SOFC stack is subjected to load following, thermal cycles, prolonged idle periods and characterisation, which can, if spatial temperature control [95] is not applied, induce large variations of the local conditions [13]. Figure 16 evaluates the effects of temperature and overpotential after 3000 h of operation or until blocking of all active sites at the interface, with a coated MIC and compressed air. The reference point is the performance of the cathode at 1073 K and an overpotential of 0.1 V. Figure 16 highlights the predominant impact of the overpotential on the severity of the degradation of the cathode. That of the temperature is in comparison limited and opposite, whether similar extents of degradation (complete blocking at Γ_5), or operating time are considered.

[Figure 16 about here.]

Figure 17 compares the range of safe operating conditions, in regard of the formation of LZO/SZO phases in the LSM-YSZ cathode, predicted by the one-dimensional and the REV models, with a dense or porous GDL. The initial state of the cathode, that is without deposited Cr_2O_3 is used for the simulations. Formation of LZO/SZO occurs first at Γ_5 . The depletion of oxygen under the ribs of the GDL system causes a noticeable shift of the limit towards lower overpotentials. The influence of the current density, which modifies the molar fraction of oxygen in the cathode, is not explicitly depicted. It accounts for the stringer limit in the plot with a porous, compared with a dense GDL and the slightly different temperature dependence, to that predicted by the one-dimensional model. The highest safe performance is achieved at high temperature, despite the thermodynamically promoted formation of zirconates, further amplified by the higher current density. A decrease of the oxygen molar fraction to a value of 0.1 which can be found in SRUs, has a noticeable detrimental effect on the allowable operating conditions.

[Figure 17 about here.]

4 Conclusion

The modelling approach presented in this study is based on a selection of phenomena that cause the degradation of the performance of IT, anode-supported SOFC SRUs/stacks. These are MIC corrosion, loss of the ionic conductivity of 8YSZ, nickel particle coarsening in the anode, and chromium contamination and development of LZO/SZO in the LSM-YSZ cathode. This is however not sufficient for a generalised view. For instance, pollution and undesirable chemical reactions are dictated by the choice of the materials, SRU design and quality of the feed gases. A comprehensive modelling of the degradation requires a tremendous amount

of data which must be gathered in view of modelling. Yet, at the current stage of SOFC knowledge, the exact nature of the degradation processes, even the most common, such as particle coarsening or chromium contamination, is not yet fully clarified. The uncertainties accumulate with those highlighted in Part I, on the underlying processes of the oxygen reduction and hydrogen reduction reactions.

The calibration of the degradation models proposed in the present study is tentative and seeks to pinpoint the experimental data required for a reliable simulation of the degradation at the stack level. The case of nickel particle coarsening, the modelling of which is very coarse, illustrates the limitations. The implementation of the degradation phenomena in an electrochemical model of suitable level of refinement provides, at a first sight, the correct dependences on the operating parameters, such as temperature, current density or overpotential. For the simulation of the behaviour of a SRU, the key point is the interaction over the active area, through temperature, current density and gas compositions. The simplest illustration is the temperature-dependent final value of the decrease in ionic conductivity of 8YSZ. The reliability of the model for history-dependent conditions, involving gradual degradation, or partial recovery, could not be tested.

The one-dimensional description of the electrochemical model for the most common MEA/GDL/MIC arrangements is sufficient for the simulation at the SRU scale, in the case the predominance of overpotential, rather than current density, is confirmed. Further adaptations will be certainly needed, as the accuracy of the knowledge on the degradation phenomena increases. The interaction between the degradation phenomena has been investigated in the light of their respective time scales and patterns, both being affected by the operating conditions. The degradation of the electrolyte and anode cannot cause in the model the end of life of a stack. In contrast, the contribution of the cathode progressively dominates and the loss of performance induced by the blocking of the active sites due to the chromium contamination may promote in turn the formation of zirconates. This kind of interaction results in an accelerated degradation rate, which is typically observed in short stack tests.

The model does however not exhibit a complete agreement with refined post-test analysis of the cathode. The assumptions for the calculation of the transport and presence of volatile chromium species, or that of full blocking of the active sites in the cathode, do not contain all the refinements needed to provide relevant guidance for the design of a LSM-YSZ cathode and its current collection layer.

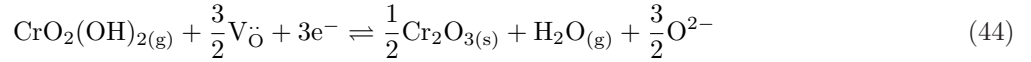
Acknowledgements

This work was funded by the Swiss SOFC Consortium, co-financed by the Swiss Federal Office of Energy (SFOE), contract number 152210 and Swisselectric Research. The author would like to thank warmly Shigehisa Kasahara (UNCTAD) for careful reading of the manuscript. gPROMS, a modelling tool from Process System Enterprise (PSE) has been used under academic licensing.

A Appendix

A.1 Chromium deposition

The derivation of Eq.40 relies on the assumption of a simple electrochemical deposition process,



which yields the rate equation

$$j = 3A_{\text{TPB}}F \left[k_a x_{\text{CrO}_2(\text{OH})_2} \exp\left(\frac{\alpha^a FE}{RT}\right) - k_c x_{\text{H}_2\text{O}} \exp\left(-\frac{\alpha^c FE}{RT}\right) \right] \quad (45)$$

Setting $j = 0$ enables the calculation of the equilibrium potential.

$$\frac{k_c x_{\text{H}_2\text{O}}}{k_a x_{\text{CrO}_2(\text{OH})_2}} = \exp\left(\frac{FE^{eq}}{RT}\right) \quad (46)$$

Insertion in Eq.45 and considering $\eta = E - E^{eq}$ and simplifying $\alpha = 0.5$ yields Eq.40.

$$j = 3A_{\text{TPB}}F(k_a k_c)^{1/2} x_{\text{CrO}_2(\text{OH})_2}^{1/2} x_{\text{H}_2\text{O}}^{1/2} \left[\exp\left(\frac{1}{2} \frac{F\eta}{RT}\right) - \exp\left(-\frac{1}{2} \frac{F\eta}{RT}\right) \right] \quad (47)$$

$$j_{\mathcal{D}_{cath}} = i_{o_{\mathcal{D}_{cath}}} x_{\text{CrO}_2(\text{OH})_2}^{1/2} x_{\text{H}_2\text{O}}^{1/2} 2 \sinh\left(\frac{1}{2} \frac{F\eta}{RT_s}\right) \quad (48)$$

A.2 Percolation model

The percolation theory described by Bouvard et al. [71] is used to estimate the effective conductivities and TPBL in both the composite cathode and anode. The key concept is the the number of contacts a particle

has with adjacent ones, of the same kind, or not. In the case of a two component mixture, the calculation of the solid volume fractions ϕ_i , number fractions n_{F_i} , coordination numbers among particle of the same kind Z_{ii} and probability that a particle belongs to a fully percolating network p_i proceeds as follows:

$$\phi_l + \phi_m = 1 \quad (49)$$

$$n_{F_i} = \frac{\frac{\phi_i}{r_{g_i}^3}}{\frac{\phi_l}{r_{g_l}^3} + \frac{\phi_m}{r_{g_m}^3}}, \quad i = l, m \quad (50)$$

$$Z_i = 3 + r_{g_i}^2 \frac{\bar{Z} - 3}{r_{g_l}^2 n_{F_l} + r_{g_m}^2 n_{F_m}}, \quad i = l, m \quad (51)$$

$$Z_{ii} = n_{F_i} \frac{Z_i Z_i}{\bar{Z}}, \quad i = l, m \quad (52)$$

$$p_i = \left[1 - \left(\frac{4.236 - Z_i}{2.472} \right)^{2.5} \right]^{0.4}, \quad i = l, m \quad (53)$$

Then, the effective conductivities and TPBL (contact angle between particle of 15°) can be assessed [72]:

$$L_{\text{TPB}} = 2\pi \min(r_{g_l} r_{g_m}) \cdot 0.2586 \cdot \frac{(1-n)\phi_l}{\frac{4}{3}\pi r_l^3} \cdot 0.5 \left(1 + \frac{r_l^2}{r_m^2} \right) \bar{Z} \frac{\frac{\phi_m}{r_{g_m}^3}}{\frac{\phi_l}{r_{g_l}^3} + \frac{\phi_m}{r_{g_m}^3}} \cdot p_m p_l \quad (54)$$

$$\rho_i^e = \frac{\rho_{o_i}^e}{(1-n)\phi_i p_i}, \quad i = l, m \quad (55)$$

A detailed discussion of the justifications and limitations of this approach is beyond the scope of this study, as the use of more advanced relations [72] or look-up tables does not alter the modelling approach of the degradation presented here.

References

- [1] S. Primdahl and M. Mogensen. Durability and thermal cycling of Ni/YSZ cermet anodes for solid oxide fuel cells. *Journal of Applied Electrochemistry*, 30(2):247 – 257, 2000.
- [2] S. Koch, P.V. Hendriksen, M. Mogensen, YL Liu, N. Dekker, B. Rietveld, B. de Haart, and F. Tietz. Solid Oxide Fuel Cell Performance under Severe Operating Conditions. *Fuel Cells-From Fundamentals to Systems*, 6(2):130 – 136, 2006.
- [3] A. Hagen, R. Barfod, P.V. Hendriksen, Y.L. Liu, and S. Ramousse. Degradation of anode supported SOFCs as a function of temperature and current load. *Journal of The Electrochemical Society*, 153:A1165 – A1171, 2006.
- [4] A. Hagen, Y. L. Liu, R. Barfod, and P. V. Hendriksen. Assessment of the cathode contribution to the degradation of anode-supported solid oxide fuel cells. *Journal of The Electrochemical Society*, 155(10):B1047 – B1052, 2008.
- [5] Y.L. Liu, A. Hagen, R. Barfod, M. Chen, H.J. Wang, F.W. Poulsen, and P.V. Hendriksen. Microstructural studies on degradation of interface between LSM-YSZ cathode and YSZ electrolyte in SOFCs. *Solid State Ionics*, 180(23-25):1298 – 1304, 2009.
- [6] H. Yokokawa, H. Tu, B. Iwanschitz, and A. Mai. Fundamental mechanisms limiting solid oxide fuel cell durability. *Journal of Power Sources*, 182(2):400 – 412, 2008.
- [7] T. Horita, H. Kishimoto, K. Yamaji, M. E. Brito, Y. Xiong, H. Yokokawa, Y. Hori, and I. Miyachi. Effects of impurities on the degradation and long-term stability for solid oxide fuel cells. *Journal of Power Sources*, 193(1):194 – 198, 2009.
- [8] E. Konyshova, H. Penkalla, E. Wessel, J. Mertens, U. Seeling, L. Singheiser, and K. Hilpert. Chromium poisoning of perovskite cathodes by the ODS alloy $\text{Cr}_5\text{FeY}_2\text{O}_3$ and the high chromium ferritic steel Crofer22APU. *Journal of The Electrochemical Society*, 153(4):A765 – A773, 2006.
- [9] K. Hilpert, D. Das, M. Miller, D. H. Peck, and R. Weiß. Chromium vapor species over solid oxide fuel cell interconnect materials and their potential for degradation processes. *Journal of The Electrochemical Society*, 143(11):3642 – 3647, 1996.
- [10] Z. Wuillemin. *Experimental and modeling investigations on local performance and local degradation in solid oxide fuel cells*. PhD thesis, Lausanne, 2009.

- [11] T. Horita, Y. Xiong, M. Yoshinaga, H. Kishimoto, K. Yamaji, M. E. Brito, and H. Yokokawa. Determination of Chromium Concentration in Solid Oxide Fuel Cell Cathodes: $(\text{La,Sr})\text{MnO}_3$ and $(\text{La,Sr})\text{FeO}_3$. *Electrochemical and Solid-State Letters*, 12(10):B146 – B149, 2009.
- [12] C. Stiller, B. Thorud, O. Bolland, R. Kandepu, and L. Imsland. Control strategy for a solid oxide fuel cell and gas turbine hybrid system. *Journal of Power Sources*, 158(1):303 – 315, 2006.
- [13] A. Nakajo, Z. Wullemin, J. Van herle, and D. Favrat. Simulation of thermal stresses in anode-supported solid oxide fuel cell stacks. Part I: Probability of failure of the cells. *Journal of Power Sources*, 193(1):203 – 215, 2009.
- [14] A. Nakajo, Z. Wullemin, J. Van herle, and D. Favrat. Simulation of thermal stresses in anode-supported solid oxide fuel cell stacks. Part II: Loss of gas-tightness, electrical contact and thermal buckling. *Journal of Power Sources*, 193(1):216 – 226, 2009.
- [15] J. Kondoh, T. Kawashima, S. Kikuchi, Y. Tomii, and Y. Ito. Effect of aging on yttria-stabilized zirconia. 1: A study of its electrochemical properties. *Journal of The Electrochemical Society*, 145(5):1527 – 1536, 1998.
- [16] J. Kondoh, S. Kikuchi, Y. Tomii, and Y. Ito. Effect of aging on yttria-stabilized zirconia. 2: A study of the effect of the microstructures on conductivity. *Journal of The Electrochemical Society*, 145(5):1536 – 1550, 1998.
- [17] J. Kondoh, S. Kikuchi, Y. Tomii, and Y. Ito. Effect of aging on yttria-stabilized zirconia. *Journal of The Electrochemical Society*, 145(5):1550 – 1560, 1998.
- [18] P. Tanasini, M. Cannarozzo, P. Costamagna, A. Faes, J. Van herle, A. Hessler-Wyser, and C. Cominellis. Experimental and Theoretical Investigation of Degradation Mechanisms by Particle Coarsening in SOFC Electrodes. *Fuel Cells*, 9(5):740–752, 2009.
- [19] A. Faes, A. Hessler-Wyser, D. Presvytes, CG Vayenas, and J. Van herle. Nickel-Zirconia Anode Degradation and Triple Phase Boundary Quantification from Microstructural Analysis. *Fuel Cells*, 9(6):841–851, 2009.
- [20] X. J. Chen, S. H. Chan, and K. A. Khor. Simulation of a composite cathode in solid oxide fuel cells. *Electrochimica Acta*, 49(11):1851 – 1861, 2004.

- [21] P. Costamagna, P. Costa, and V. Antonucci. Micro-modelling of solid oxide fuel cell electrodes. *Electrochimica Acta*, 43(3-4):375 – 394, 1998.
- [22] B. Kenney and K. Karan. Engineering of microstructure and design of a planar porous composite SOFC cathode: A numerical analysis. *Solid State Ionics*, 178(3-4):297 – 306, 2007.
- [23] D. Larrain, J. Van herle, and D. Favrat. Simulation of SOFC stack and repeat elements including interconnect degradation and anode reoxidation risk. *Journal of Power Sources*, 161(1):392 – 403, 2006.
- [24] J.I. Gazzarri and O. Kesler. Short-stack modeling of degradation in solid oxide fuel cells: Part I. Contact degradation. *Journal of Power Sources*, 176(1):138 – 154, 2008.
- [25] A. Nakajo, Z. Wuillemin, P. Metzger, S. Diethelm, G. Schiller, Jan Van herle, and Daniel Favrat. Electrochemical model of solid oxide fuel cell for simulation at the stack scale. Part I: Calibration procedure on experimental data. *Manuscript submitted to the Journal of The Electrochemical Society*.
- [26] gPROMS (General Process Modelling and Simulation Tool), v3.2, Process Systems Enterprise Ltd., London.
- [27] D. Larrain, J. Van herle, F. Maréchal, and D. Favrat. Generalized model of planar SOFC repeat element for design optimization. *Journal of Power Sources*, 131(1-2):304 – 312, 2004.
- [28] J. Fleig, H.L. Tuller, and J. Maier. Electrodes and electrolytes in micro-SOFCs: a discussion of geometrical constraints. *Solid State Ionics*, 174(1-4):261 – 270, 2004.
- [29] E. Achenbach and E. Riensche. Methane/steam reforming kinetics for solid oxide fuel cells. *Journal of Power Sources*, 52(2):283 – 288, 1994.
- [30] T. X. Ho, P. Kosinski, Alex C. Hoffmann, and A. Vik. Modeling of transport, chemical and electrochemical phenomena in a cathode-supported SOFC. *Chemical Engineering Science*, 64(12):3000 – 3009, 2009.
- [31] A. Selimovic, M. Kemm, T. Torisson, and M. Assadi. Steady state and transient thermal stress analysis in planar solid oxide fuel cells. *Journal of Power Sources*, 145(2):463 – 469, 2005.
- [32] ThyssenKrupp. Material data sheet no. 4046.
- [33] C.-K. Lin, T.-T. Chen, Y.-P. Chyou, and L.-K. Chiang. Thermal stress analysis of a planar SOFC stack. *Journal of Power Sources*, 164(1):238 – 251, 2007.

- [34] A. Nakajo, F. Mueller, J. Cugnoni, J Brouwer, J. Van herle, and D. Favrat. Mechanical reliability and durability of SOFC stacks. Part I: Modelling of the effect of the operating conditions on the reliability. *Manuscript in preparation*.
- [35] M. Stanislawski, E. Wessel, K. Hilpert, T. Markus, and L. Singheiser. Chromium vaporization from high-temperature alloys. *Journal of The Electrochemical Society*, 154(4):A295–A306, 2007.
- [36] W.N. Liu, X. Sun, E. Stephens, and M.A. Khaleel. Life prediction of coated and uncoated metallic interconnect for solid oxide fuel cell applications. *Journal of Power Sources*, 189(2):1044 – 1050, 2009.
- [37] F. Wiener, M. Bram, H.P. Buchkremer, and D. Sebold. Chemical interaction between Crofer 22 APU and mica-based gaskets under simulated SOFC conditions. *Journal of Materials Science*, 42(8):2643 – 2651, 2007.
- [38] T. Horita, H. Kishimoto, K. Yamaji, Y. Xiong, N. Sakai, M. E. Brito, and H. Yokokawa. Oxide scale formation and stability of Fe – Cr alloy interconnects under dual atmospheres and current flow conditions for SOFCs. *Journal of The Electrochemical Society*, 153(11):A2007 – A2012, 2006.
- [39] P. Batfalsky, V.A.C. Haanappel, J. Malzbender, N.H. Menzler, V. Shemet, I.C. Vinke, and R.W. Steinbrech. Chemical interaction between glass-ceramic sealants and interconnect steels in SOFC stacks. *Journal of Power Sources*, 155(2):128 – 137, 2006.
- [40] Z. Yang, K. S. Weil, D. M. Paxton, and J. W. Stevenson. Selection and evaluation of heat-resistant alloys for SOFC interconnect applications. *Journal of The Electrochemical Society*, 150(9):A1188 – A1201, 2003.
- [41] J. Froitzheim, G.H. Meier, L. Niewolak, P.J. Ennis, H. Hattendorf, L. Singheiser, and W.J. Quadackers. Development of high strength ferritic steel for interconnect application in SOFCs. *Journal of Power Sources*, 178(1):163 – 173, 2008.
- [42] J. W. Fergus. Metallic interconnects for solid oxide fuel cells. *Materials Science and Engineering A*, 397(1-2):271 – 283, 2005.
- [43] T. Horita, Y. Xiong, K. Yamaji, N. Sakai, and H. Yokokawa. Evaluation of Fe-Cr alloys as interconnects for reduced operation temperature SOFCs. *Journal of The Electrochemical Society*, 150(3):A243 – A248, 2003.

- [44] N. Sakai, T. Horita, Y. P. Xiong, K. Yamaji, H. Kishimoto, M. E. Brito, H. Yokokawa, and T. Maruyama. Structure and transport property of manganese-chromium-iron oxide as a main compound in oxide scales of alloy interconnects for SOFCs. *Solid State Ionics*, 176(7-8):681 – 686, 2005.
- [45] N. Sakai, T. Horita, Y. P. Xiong, K. Yamaji, H. Kishimoto, M. E. Brito, H. Yokokawa, and T. Maruyama. Structure and transport property of manganese-chromium-iron oxide as a main compound in oxide scales of alloy interconnects for SOFCs. *Solid State Ionics*, 176(7-8):681 – 686, 2005.
- [46] M. Brandner, M. Bram, J. Froitzheim, H.P. Buchkremer, and D. Stöver. Electrically conductive diffusion barrier layers for metal-supported SOFC. *Solid State Ionics*, 179(27-32):1501 – 1504, 2008.
- [47] T. Brylewski, M. Nanko, T. Maruyama, and K. Przybylski. Application of Fe-16Cr ferritic alloy to interconnector for a solid oxide fuel cell. *Solid State Ionics*, 143(2):131 – 150, 2001.
- [48] T. Horita, K. Yamaji, Y. Xiong, H. Kishimoto, N. Sakai, and H. Yokokawa. Oxide scale formation of Fe-Cr alloys and oxygen diffusion in the scale. *Solid State Ionics*, 175(1-4):157 – 163, 2004.
- [49] T. Horita, Y. Xiong, H. Kishimoto, K. Yamaji, N. Sakai, M. E. Brito, and H. Yokokawa. Oxidation behavior of Fe-Cr- and Ni-Cr-based alloy interconnects in $\text{CH}_4\text{-H}_2\text{O}$ for solid oxide fuel cells. *Journal of The Electrochemical Society*, 152(11):A2193 – A2198, 2005.
- [50] T. Horita, Y. Xiong, H. Kishimoto, K. Yamaji, N. Sakai, and H. Yokokawa. Application of Fe-Cr alloys to solid oxide fuel cells for cost-reduction: Oxidation behavior of alloys in methane fuel. *Journal of Power Sources*, 131(1-2):293 – 298, 2004.
- [51] Z. Yang, M. S. Walker, P. Singh, J. W. Stevenson, and T. Norby. Oxidation behavior of ferritic stainless steels under SOFC interconnect exposure conditions. *Journal of The Electrochemical Society*, 151(12):B669 – B678, 2004.
- [52] T. Horita, K. Yamaji, H. Yokokawa, A. Toji, T. Uehara, K. Ogasawara, H. Kameda, Y. Matsuzaki, and S. Yamashita. Effects of Si and Al concentrations in Fe-Cr alloy on the formation of oxide scales in $\text{H}_2\text{-H}_2\text{O}$. *International Journal of Hydrogen Energy*, 33(21):6308 – 6315, 2008.
- [53] Z. Yang, J. S. Hardy, M. S. Walker, G. Xia, S. P. Simner, and J. W. Stevenson. Structure and conductivity of thermally grown scales on ferritic Fe-Cr-Mn steel for SOFC interconnect applications. *Journal of The Electrochemical Society*, 151(11):A1825 – A1831, 2004.

- [54] Z. Yang, G. Xia, S. P. Simner, and J. W. Stevenson. Thermal growth and performance of manganese cobaltite spinel protection layers on ferritic stainless steel SOFC interconnects. *Journal of The Electrochemical Society*, 152(9):A1896 – A1901, 2005.
- [55] Z. Yang. Recent advances in metallic interconnects for solid oxide fuel cells. *International Materials Reviews*, 53(1):39 – 54, 2008.
- [56] Z. Yang, G. Xia, J.W. Stevenson, and P. Sing. IV. A. 17 SOFC Interconnect Materials Development at PNNL.
- [57] A. N. Vlasov and M. V. Perfiliev. Ageing of ZrO₂-based solid electrolytes. *Solid State Ionics*, 25(4):245 – 253, 1987.
- [58] M. Hattori, Y. Takeda, J. H. Lee, S. Ohara, K. Mukai, T. Fukui, S. Takahashi, Y. Sakaki, and A. Nakanishi. Effect of annealing on the electrical conductivity of the Y₂O₃-ZrO₂ system. *Journal of Power Sources*, 131(1-2):247 – 250, 2004.
- [59] M. Hattori, Y. Takeda, Y. Sakaki, A. Nakanishi, S. Ohara, K. Mukai, J.H. Lee, and T. Fukui. Effect of aging on conductivity of yttria stabilized zirconia. *Journal of Power Sources*, 126(1-2):23 – 27, 2004.
- [60] CC Appel, N. Bonanos, A. Horsewell, and S. Linderoth. Ageing behaviour of zirconia stabilised by yttria and manganese oxide. *Journal of Materials Science*, 36(18):4493 – 4501, 2001.
- [61] B. Butz, P. Kruse, H. Störmer, D. Gerthsen, A. Müller, A. Weber, and E. Ivers-Tiffée. Correlation between microstructure and degradation in conductivity for cubic Y₂O₃-doped ZrO₂. *Solid State Ionics*, 177(37-38):3275 – 3284, 2006.
- [62] J. Kondoh, H. Shiota, S. Kikuchi, Y. Tomii, Y. Ito, and K. Kawachi. Changes in aging behavior and defect structure of Y₂O₃ fully stabilized ZrO₂ by In₂O₃ doping. *Journal of The Electrochemical Society*, 149(8):J59 – J72, 2002.
- [63] C. Haering, A. Roosen, and H. Schichl. Degradation of the electrical conductivity in stabilised zirconia systems: Part I: yttria-stabilised zirconia. *Solid State Ionics*, 176(3-4):253 – 259, 2005.
- [64] YL Liu and C. Jiao. Microstructure degradation of an anode/electrolyte interface in SOFC studied by transmission electron microscopy. *Solid State Ionics*, 176(5-6):435 – 442, 2005.

- [65] W.G. Coors, J.R. O'Brien, and J.T. White. Conductivity degradation of NiO-containing 8YSZ and 10YSZ electrolyte during reduction. *Solid State Ionics*, 180(2-3):246 – 251, 2009.
- [66] K. Vels Jensen, S. Primdahl, I. Chorkendorff, and M. Mogensen. Microstructural and chemical changes at the Ni/YSZ interface. *Solid State Ionics*, 144(3-4):197 – 209, 2001.
- [67] D. Simwonis, F. Tietz, and D. Stöver. Nickel coarsening in annealed Ni/8YSZ anode substrates for solid oxide fuel cells. *Solid State Ionics*, 132(3-4):241 – 251, 2000.
- [68] R. Stübner. *Untersuchungen zu den Eigenschaften der Anode der Festoxid-Brennstoffzelle (SOFC)*. PhD thesis.
- [69] J. H. Choi, J. H. Jang, and S. M. Oh. Microstructure and cathodic performance of $\text{La}_{0.9}\text{Sr}_{0.1}\text{MnO}_3$ /yttria-stabilized zirconia composite electrodes. *Electrochimica Acta*, 46(6):867 – 874, 2001.
- [70] N. H. Menzler, I. Vinke, and H. Lippert. Chromium Poisoning of LSM Cathodes - Results from Stack Testing. *ECS Transactions*, 25(2):2899 – 2908, 2009.
- [71] D. Bouvard and F.F. Lange. Relation between percolation and particle coordination in binary powder mixtures. *Acta Metallurgica et Materialia*, 39(12):3083 – 3090, 1991.
- [72] D. Chen, Z. Lin, H. Zhu, and R. J. Kee. Percolation theory to predict effective properties of solid oxide fuel-cell composite electrodes. *Journal of Power Sources*, 191(2):240 – 252, 2009.
- [73] J. Sehested. Four challenges for nickel steam-reforming catalysts. *Catalysis Today*, 111(1-2):103 – 110, 2006.
- [74] R. Vaßen, D. Simwonis, and D. Stöver. Modelling of the agglomeration of Ni-particles in anodes of solid oxide fuel cells. *Journal of Materials Science*, 36(1):147 – 151, 2001.
- [75] K.T.S. Thydén. *Microstructural degradation of Ni-YSZ anodes for solid oxide fuel cells*. PhD thesis, Technical University of Denmark, Risø National Laboratory for Sustainable Energy, Fuel Cells and Solid State Chemistry Division.
- [76] Z. Wullemmin, N. Autissier, A. Nakajo, M.-T. Luong, J. Van herle, and D. Favrat. Modeling and Study of the Influence of Sealing on a Solid Oxide Fuel Cell. *Journal of Fuel Cell Science and Technology*, 5(1):011016 – 9, 2008.

- [77] G. R. Holcomb and D. E. Alman. The effect of manganese additions on the reactive evaporation of chromium in Ni-Cr alloys. *Scripta Materialia*, 54(10):1821 – 1825, 2006.
- [78] S. P. Jiang, J. P. Zhang, L. Apateanu, and K. Foger. Deposition of chromium species at Sr-doped LaMnO₃ electrodes in solid oxide fuel cells. I. Mechanism and kinetics. *Journal of The Electrochemical Society*, 147(11):4013 – 4022, 2000.
- [79] S. P. Jiang, J. P. Zhang, and K. Foger. Deposition of chromium species at Sr-doped LaMnO₃ electrodes in Solid Oxide Fuel Cells II. Effect on O₂ reduction reaction. *Journal of The Electrochemical Society*, 147(9):3195 – 3205, 2000.
- [80] Y. Matsuzaki and I. Yasuda. Dependence of SOFC cathode degradation by chromium-containing alloy on compositions of electrodes and electrolytes. *Journal of The Electrochemical Society*, 148(2):A126 – A131, 2001.
- [81] J. W. Fergus. Effect of cathode and electrolyte transport properties on chromium poisoning in solid oxide fuel cells. *International Journal of Hydrogen Energy*, 32(16):3664 – 3671, 2007.
- [82] E. Konyshova, J. Mertens, H. Penkalla, L. Singheiser, and K. Hilpert. Chromium poisoning of the porous composite cathode. *Journal of The Electrochemical Society*, 154(12):B1252 – B1264, 2007.
- [83] M. Backhaus-Ricoult. SOFC–A playground for solid state chemistry. *Solid State Sciences*, 10(6):670 – 688, 2008.
- [84] M. J. Jørgensen and M. Mogensen. Impedance of solid oxide fuel cell LSM/YSZ composite cathodes. *Journal of The Electrochemical Society*, 148(5):A433 – A442, 2001.
- [85] S.B. Adler. Factors Governing Oxygen Reduction in Solid Oxide Fuel Cell Cathodes. *Chem. Rev*, 104(10):4791 – 4844, 2004.
- [86] J. Nielsen, A. Hagen, and Y.L. Liu. Effect of cathode gas humidification on performance and durability of Solid Oxide Fuel Cells. *Solid State Ionics*, 181(11-12):517 – 524, 2010.
- [87] S. P. Jiang and W. Wang. Effect of polarization on the interface between (La,Sr)MnO₃ electrode and Y₂O₃ – ZrO₂ electrolyte. *Electrochemical and Solid-State Letters*, 8(2):A115 – A118, 2005.
- [88] A. Mitterdorfer and L. J. Gauckler. La₂Zr₂O₇ formation and oxygen reduction kinetics of the La_{0.85}Sr_{0.15}Mn_yO₃, O₂(g)YSZ system. *Solid State Ionics*, 111(3-4):185 – 218, 1998.

- [89] M. Chen, YL Liu, A. Hagen, PV Hendriksen, and FW Poulsen. LSM-YSZ Reactions in Different Atmospheres. *Fuel Cells*, 9(6):833 – 840, 2009.
- [90] C.C.T. Yang, W.C.J. Wei, and A. Roosen. Reaction Kinetics and Mechanisms between $\text{La}_{0.65}\text{Sr}_{0.3}\text{MnO}_3$ and 8 mol% Yttria-Stabilized Zirconia. *J. Am. Ceram. Soc.*, 87(6):1110 – 1116, 2004.
- [91] K. Nisancioglu. Ohmic losses. *Proceedings of the IEA workshop on mathematical modelling. Charmey*, pages 87 – 98, 1998.
- [92] A. Nakajo, F. Mueller, J. Brouwer, Jan Van herle, and Daniel Favrat. Progressive activation of degradation processes in SOFC stacks. Part II : Modelling of the spatial distribution of the degradation. *Manuscript in preparation*.
- [93] LGJ de Haart, J. Mougín, O. Posdziech, J. Kiviaho, and NH Menzler. Stack Degradation in Dependence of Operation Parameters; the Real-SOFC Sensitivity Analysis. *Fuel Cells*, 9(6):794 – 804, 2009.
- [94] A. Neumann, N. H. Menzler, I. Vinke, and H. Lippert. Systematic Study of Chromium Poisoning of LSM Cathodes - Single Cell Tests. *ECS Transactions*, 25(2):2889 – 2898, 2009.
- [95] M. Fardadi, F. Mueller, and F. Jabbari. Feedback control of solid oxide fuel cell spatial temperature variation. *Journal of Power Sources*, 195(13):4222 – 4233, 2010.
- [96] S.L. Swartz, M. Beachy, and M.M. Seabaugh. Continuous Process for Low-Cost, High-Quality YSZ Powder. Technical report, NexTech Materials, Ltd., 2006.
- [97] N. Balakrishnan, T. Takeuchi, K. Nomura, H. Kageyama, and Y. Takeda. Aging Effect of 8 mol % YSZ Ceramics with Different Microstructures. *Journal of The Electrochemical Society*, 151(8):A1286 – A1291, 2004.
- [98] D. Simwonis. Optimierung der Anoden der Hochtemperatur-Brennstoffzelle durch Korrelation von Herstellungsverfahren, Gefüge und Eigenschaften; Jül-report 3678. *Edited by Forschungszentrum Jülich, Germany*, 1999.

List of Figures

- 1 (a) View of the LENI-EPFL FlameSOFC SRU design. (b) Description of the geometry and typical dimensions modelled in
- 2 Representation of a SOF cell, based on a LSM-YSZ cathode, and denomination of the domains and interfaces. 42
- 3 Parabolic growth rates used for the calculation of the ASR of a MIC subjected to air or fuel atmospheres [41, 47, 48, 50, 52].
- 4 Evolution of the ASR of ferritic MIC computed by Eq.34 subjected to air (Crofer22H/APU) or fuel (ZMG232) side. Parame
- 5 Comparison between evolutions of the ionic conductivity of 8YSZ predicted by Eq.37 (lines) and measured (markers) [15, 58.
- 6 Evolution of the normalised particle size of nickel in Ni-YSZ anodes predicted by Eq.38 (lines) and measured (markers) [19,
- 7 Representation of the assumption for the calculation of the TPB blocked by the deposition of Cr_2O_3 . 47
- 8 Comparison between the local electrochemical behaviour simulated by the one-dimensional model and the REV model, with
- 9 Evolution at locations A,B and C (Figure 1a), in co-flow and counter-flow, of the relative ASR and overpotential of the cath
- 10 Profiles of the norm of the current density in the cathode and GDL (top), oxygen molar fraction (second), steam in the anoc
- 11 Comparison between relative degradation rates measured on short stacks [93] and those predicted by the one-dimensional m
- 12 Initial ASR at an overpotential of 0.05 V, and influence of operating conditions on the degradation of the anode: relative inc
- 13 (a): evolution of the number of active sites in the cathode. 1073 K, $x_{\text{O}_2}=0.21$, $j = 0.5 \text{ Acm}^{-2}$, computation of $\text{CrO}_2(\text{OH})_{2(\text{g})}$
- 14 Effect of temperature and overpotential on the initial ASR and degradation of the cathode: relative increase in ASR, rate of
- 15 Initial ASR of the cathode, and relative increase in ASR and rate of the relative increase in ASR. Simulations of 3000 h with
- 16 Effects of operating conditions on the ASR of the cathode at 1073 K and an assigned overpotential of 0.1 V (point depicted
- 17 Operating conditions to avoid the formation of LZO/SZO insulating phases in the LSM-YSZ cathode, predicted by the one-

Figure 1: (a) View of the LENI-EPFL FlameSOFC SRU design. (b) Description of the geometry and typical dimensions modelled in the REV model, along with denomination of the domains. The domains in \mathcal{R}_{3-5} are detailed in Figure 2.

Figure 2: Representation of a SOF cell, based on a LSM-YSZ cathode, and denomination of the domains and interfaces.

Figure 3: Parabolic growth rates used for the calculation of the ASR of a MIC subjected to air or fuel atmospheres [41, 47, 48, 50, 52].

Figure 4: Evolution of the ASR of ferritic MIC computed by Eq.34 subjected to air (Crofer22H/APU) or fuel (ZMG232) side. Parameters listed in Table 1.

Figure 5: Comparison between evolutions of the ionic conductivity of 8YSZ predicted by Eq.37 (lines) and measured (markers) [15, 58, 60–62, 96, 97]. Fitting performed exclusively on the data of Kondoh et al. [15, 62] (small dots).

Figure 6: Evolution of the normalised particle size of nickel in Ni-YSZ anodes predicted by Eq.38 (lines) and measured (markers) [19, 67, 75, 98].

Figure 7: Representation of the assumption for the calculation of the TPB blocked by the deposition of Cr_2O_3 .

Figure 8: Comparison between the local electrochemical behaviour simulated by the one-dimensional model and the REV model, with a dense or porous GDL, during IV characterisation of the SRU depicted in Figure 1a. CO: co-flow, COU: counter-flow configuration.

Figure 9: Evolution at locations A,B and C (Figure 1a), in co-flow and counter-flow, of the relative ASR and overpotential of the cathode and anode, during operation at the nominal point (Figure 8) at constant SRU potential. The approximate initial temperature and current density are indicated. Color online.

Figure 10: Profiles of the norm of the current density in the cathode and GDL (top), oxygen molar fraction (second), steam in the anode and GDL (third) and local overpotential at the electrode/electrolyte (fourth). The whole GDLs are not depicted for clarity. Conditions correspond to the fuel inlet in counter-flow (A in Figure 1a), after approximately 500 h of operation at the nominal point.

Figure 11: Comparison between relative degradation rates measured on short stacks [93] and those predicted by the one-dimensional model, without any calibration. Color online.

Figure 12: Initial ASR at an overpotential of 0.05 V, and influence of operating conditions on the degradation of the anode: relative increase in ASR, rate of the relative increase in ASR and time to reach $r_{gNi\infty}$.

Figure 13: (a): evolution of the number of active sites in the cathode. 1073 K, $x_{O_2}=0.21$, $j = 0.5 \text{ Acm}^{-2}$, computation of $\text{CrO}_2(\text{OH})_{2(\text{g})}$ at 973 K. (b): effect of the electrode thickness and assumptions for the calculation of $\text{CrO}_2(\text{OH})_{2(\text{g})}$ on the degradation of the cathode. Times indicate start of zirconate formation. One-dimensional model.

Figure 14: Effect of temperature and overpotential on the initial ASR and degradation of the cathode: relative increase in ASR, rate of the relative increase in ASR. Effect of the assumptions for the calculation of $x_{CrO_2(OH)_2(g)}$: gas channel (a) and gas inlet conditions (b). Simulated with the one-dimensional model, until the active sites at the cathode/electrolyte interface Γ_5 are blocked.

Figure 15: Initial ASR of the cathode, and relative increase in ASR and rate of the relative increase in ASR. Simulations of 3000 h with the one-dimensional model.

Figure 16: Effects of operating conditions on the ASR of the cathode at 1073 K and an assigned overpotential of 0.1 V (point depicted in Figure 15), after 3000 h or until the full blocking of the active sites at the cathode/electrolyte interface Γ_5 . One-dimensional model.

Figure 17: Operating conditions to avoid the formation of LZO/SZO insulating phases in the LSM-YSZ cathode, predicted by the one-dimensional model (gray areas), and the REV model, with a dense or porous GDL (lines). The current density computed by the one-dimensional model, for air, is indicated.

List of Tables

1	Input values used for the modelling of degradation.	59
2	Values from [11] used for the estimate of the exchange current density in Eq.40.	60
3	Operating conditions for the SRU simulations.	61

MIC			
	Crofer22 (air)	ZMG232L (H ₂ /H ₂ O)	ZMG232L (CH ₄ /H ₂ O)
k_{m_g} [cm ² h ⁻¹]	1.38e4	0.913	0.406
$E_{a_{\mathcal{D}MIC}}$ [kJ mol ⁻¹]	286.6	202.3	202.3
$k_{o MIC}$ [S cm ⁻¹]	0.458	17.76	1.205
$E_{a_{MIC}}$ [kJ mol ⁻¹]	33.3	72.4	45.34
Electrolyte ^a			
$k_{o_{\mathcal{D}elect\infty}}$	$E_{a_{\mathcal{D}elect\infty}}$ [kJ mol ⁻¹]	$k_{o_{\mathcal{D}elect}}$	$E_{a_{\mathcal{D}elect}}$ [kJ mol ⁻¹]
201.8	61.15	148.7	12.67
Anode ^a			
$k_{o_{\mathcal{D}an}}$	$E_{a_{\mathcal{D}an}}$ [kJ mol ⁻¹]	$r_{gNi\infty}$	
1.05e-3	15.15	1.38	
Cathode			
$i_{o_{\mathcal{D}cath}}$ [A cm ⁻²]	w_{TPB} [nm]	h_{TPB} [nm]	
6.77e-4	150	35	

^a Dimensionless

Table 1: Input values used for the modelling of degradation.

x_{H_2O}	$x_{CrO_2(OH)_2}$	\mathcal{N}_{at}	t [h]	η [V]	A_{TPB} [cm ²]	T [K]
0.01	10^{-8}	$\approx 1.75 \cdot 10^{16}$	300	0.3	$\approx 0.785 \cdot 0.2$	1073

Table 2: Values from [11] used for the estimate of the exchange current density in Eq.40.

Air inlet temperature [K]	973
Fuel inlet temperature [K]	973
Fuel flow [nmlpm cm ⁻²]	3.6
Air ratio	5-7.5 ^a
Inlet molar fractions	
H ₂	0.263
H ₂ O	0.493
CH ₄	0.171
CO	0.029
CO ₂	0.044

^a Value coarsely adjusted to yield a similar maximum temperature of 1100K at FU=0.8, in co-flow, respectively counter-flow

Table 3: Operating conditions for the SRU simulations.

Nomenclature

Latin letters

\bar{Z}	coordination number (6)
\mathcal{N}_{at}	number of atoms
\mathfrak{R}_i	rate of production of species i ($\text{mol m}^{-3} \text{s}^{-1}$)
ASR	area specific resistance ($\Omega \text{ m}^2$)
A_{TPB}	specific area at the triple phase boundary ($\text{m}^2 \text{ m}^{-3}$)
B_o	permeability in porous medium (m^2)
c_t	total molar concentration (mol m^{-3})
D_{ij}^e	effective bulk diffusivity of binary pair in porous medium ($\text{m}^2 \text{ s}^{-1}$)
D_{iM}^e	effective Knudsen diffusivity of species i in porous medium ($\text{m}^2 \text{ s}^{-1}$)
E	electric potential (V)
E_a	activation energy (J mol^{-1})
F	Faraday's constant 96485 (C mol^{-1})
h	thickness (m)
i_o	exchange current density (A m^{-2})
i_t	faraidic transfer current density (A m^{-2})
j	current density (A m^{-2})
K	ratio of rate constants
k	rate constant
k_g	parabolic weight gain rate constant ($\text{kg}^2 \text{ m}^{-4} \text{ s}^{-1}$)
k_m	parabolic rate constant ($\text{m}^2 \text{ s}^{-1}$)
k_o	kinetic constant

L	length (m)
L_{TPB}	TPB length (m m^{-3})
M_i	molecular weight of species i (kg mol^{-1})
n	porosity
N_i	molar flux of species i ($\text{mol m}^{-2} \text{s}^{-1}$)
n_{Fi}	number fraction of particle i for percolation predictions
p	pressure (Pa)
p^{atm}	atmospheric pressure 101325 (Pa)
p_i	percolation probability of particles i
R	universal gas constant 8.314 ($\text{J mol}^{-1} \text{K}^{-1}$)
r_g	grain radius (m)
T	temperature (K)
t	time (s)
T_{ref}	reference temperature 873 (K)
V	potential in ionic or electronic conducting phases (V)
w	width (m)
x_i	mole fraction of species i
Z_i	coordination number of particles i
Z_{ii}	coordination number among particles i

Greek letters

α	symmetry coefficient
η	overpotential (V)
μ_g	viscosity (Pa s)

ϕ	volume fraction of solid phases
ρ	density (kg m^{-3})
ρ^e	effective resistivity ($\Omega \text{ m}$)
σ^e	effective electrical conductivity (S m^{-1})
ξ	correction factor

Indices

∞ final state

\mathcal{D} degradation

Nernst Nernst potential

a anodic

an anode

c cathodic

$cath$ cathode

el electronic

$elect$ electrolyte

g index for gases, either air or fuel

ion ionic

o initial, dense state

ox oxide scale

s index for solid parts, individual components or averaged structure

tot total

Superscripts

ct charge transfer

a anodic
c cathodic
eq equilibrium

Acronyms

ASR area specific resistance
COU Counter-flow configuration
CO Co-flow configuration
DEM discrete element method
DGM dusty gas model
EIS electrochemical impedance spectroscopy
GDC gadolinia-doped ceria
GDL gas diffusion layer
HO hydrogen oxidation
IT intermediate temperature
LSM lanthanum strontium manganite
LZO lanthanum zirconate
MEA membrane electrode assembly
MIC metallic interconnect
Ni-YSZ nickel-YSZ anode in reduced state
OCV open circuit voltage
ORR oxygen reduction reaction
REV representative elementary volume
SEM scanning electron microscopy

SMR steam-methane reforming reaction

SRU standard repeating unit

SZO strontium zirconate

TEM transmission electron microscopy

TPBL triple phase boundary length

TPB triple phase boundary

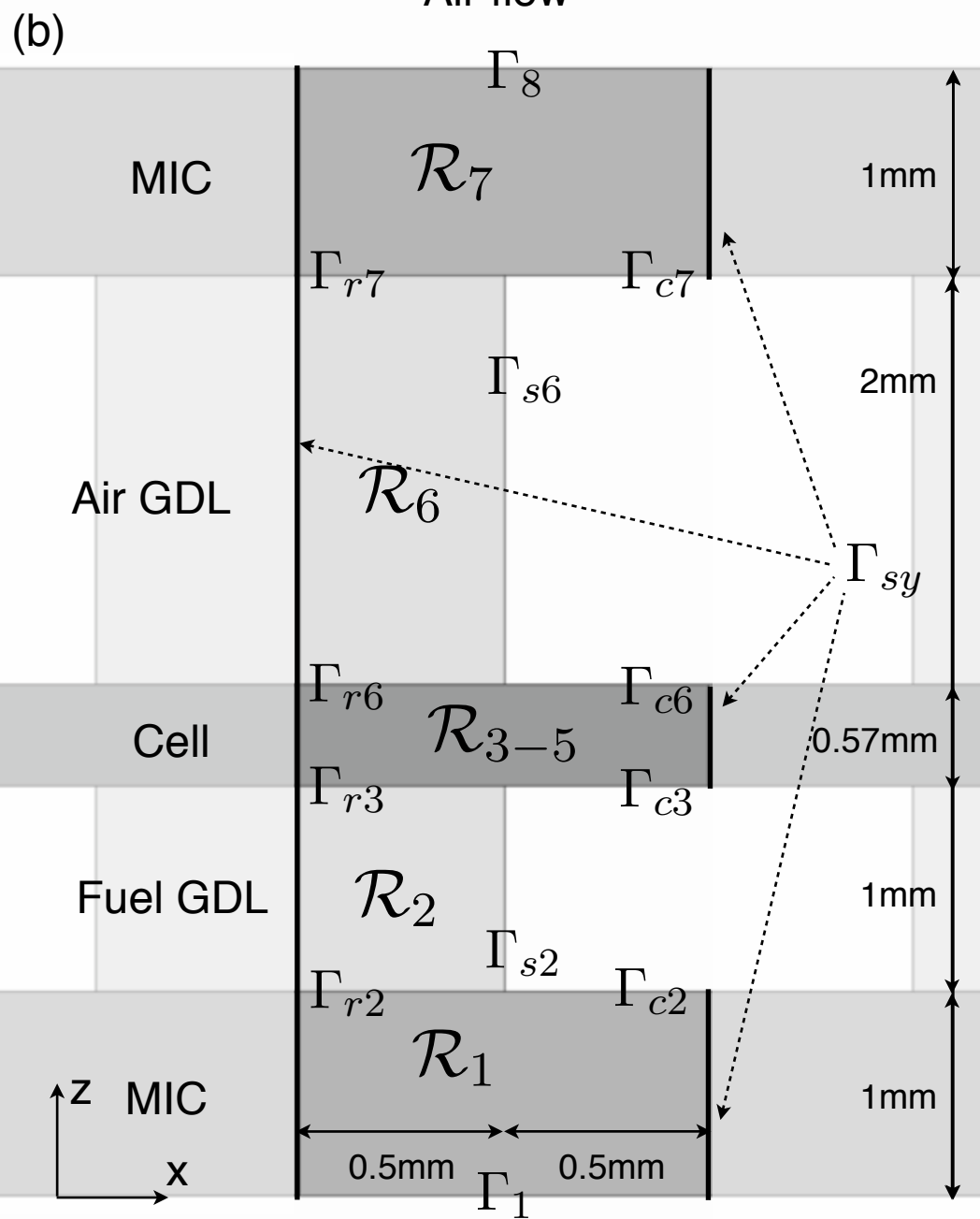
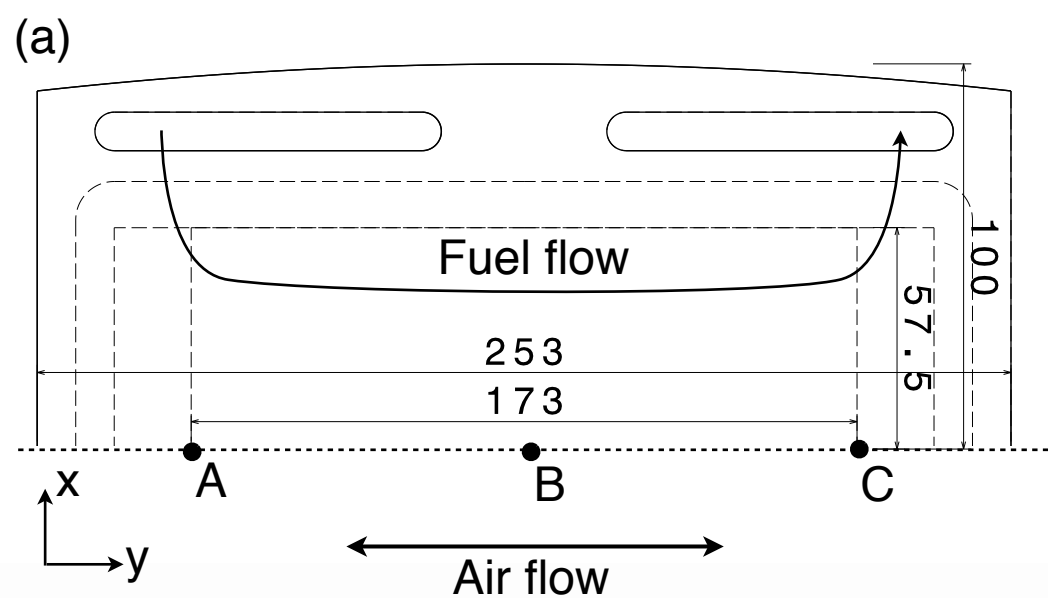
WDX wavelength-dispersive X-ray spectroscopy

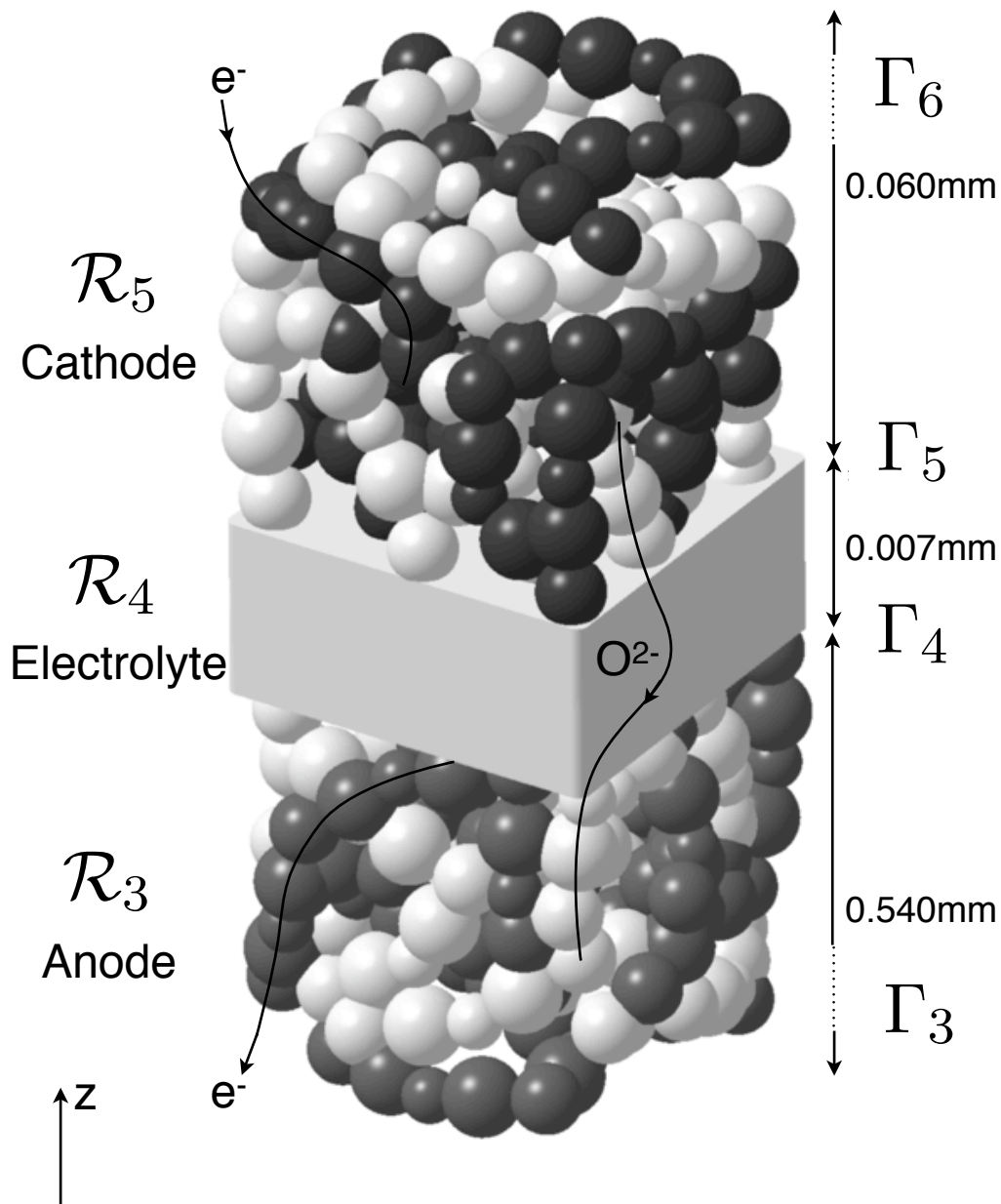
WS water-gas shift reaction

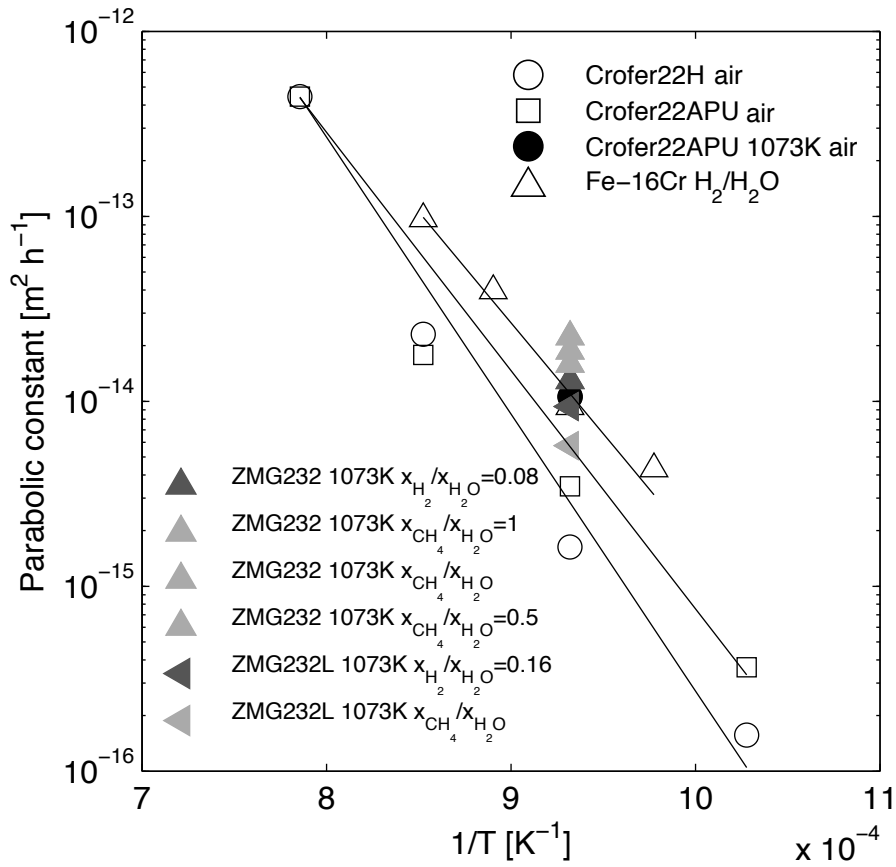
YSZ yttria-stabilised zirconia

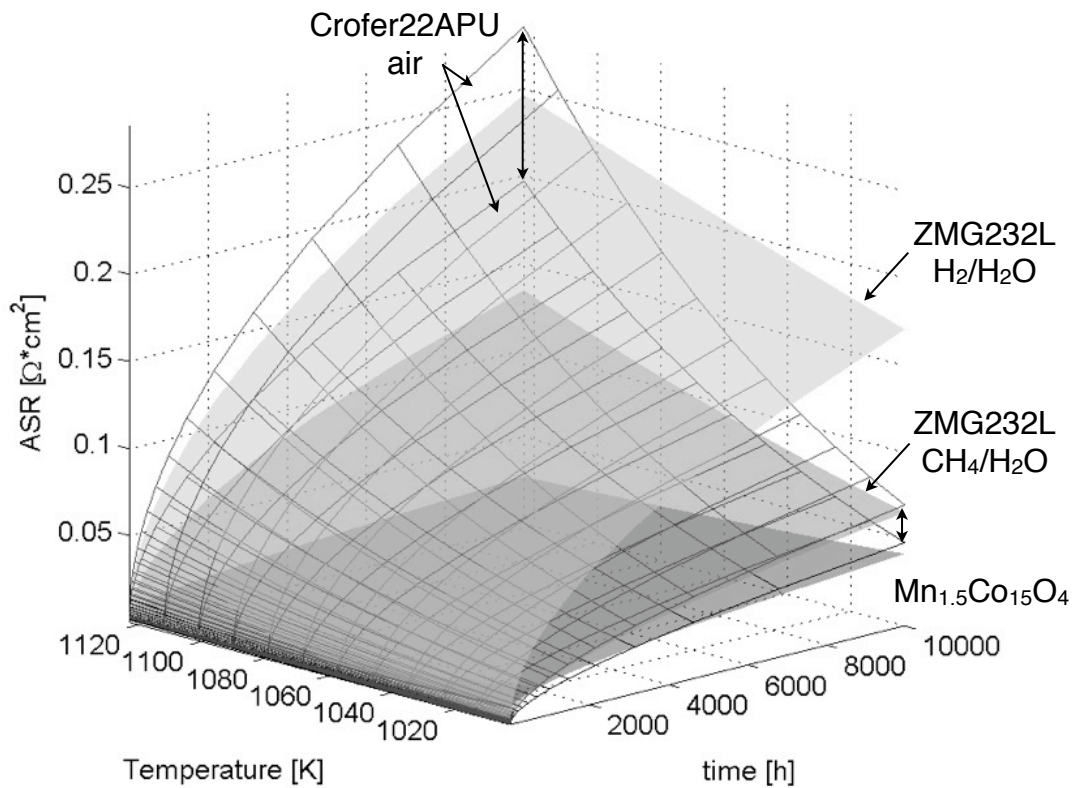
List of Figures

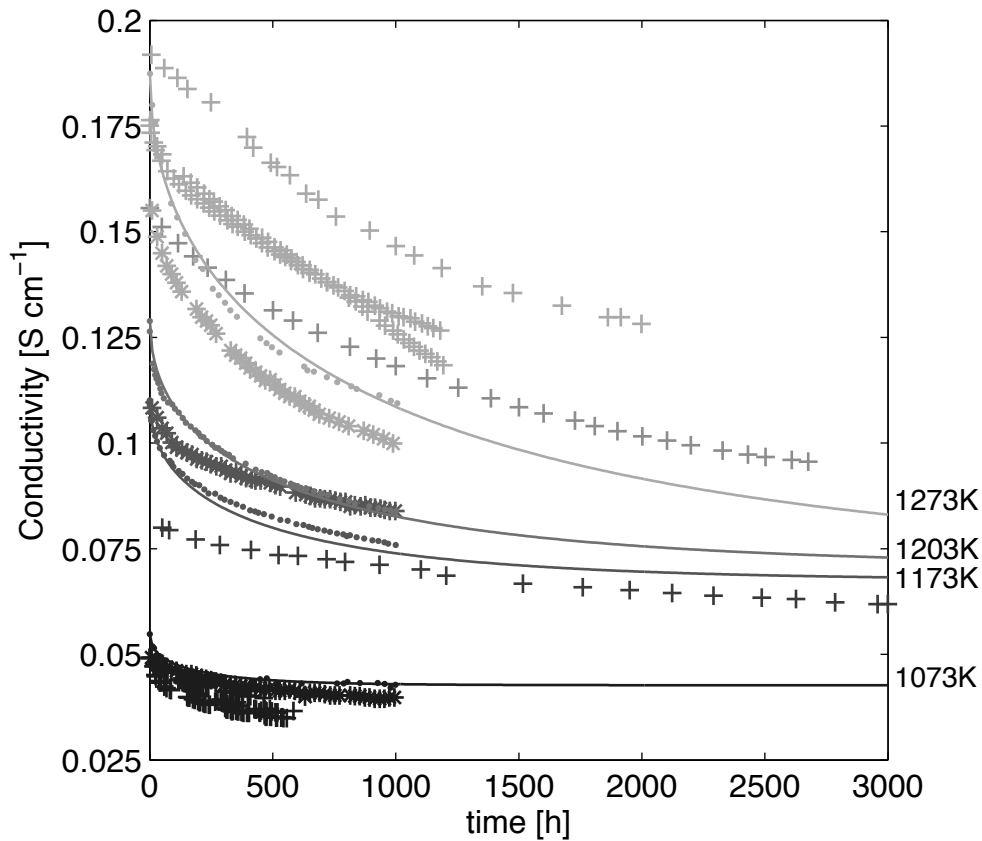
1	(a) View of the LENI-EPFL FlameSOFC SRU design. (b) Description of the geometry and typical dimensions modelled in the REV model, along with denomination of the domains. The domains in \mathcal{R}_{3-5} are detailed in Figure 2.	46
2	Representation of a SOF cell, based on a LSM-YSZ cathode, and denomination of the domains and interfaces.	47
3	Parabolic growth rates used for the calculation of the ASR of a MIC subjected to air or fuel atmospheres [41, 47, 48, 50, 52].	48
4	Evolution of the ASR of ferritic MIC computed by Eq.34 subjected to air (Crofer22H/APU) or fuel (ZMG232) side. Parameters listed in Table 1.	49
5	Comparison between evolutions of the ionic conductivity of 8YSZ predicted by Eq.37 (lines) and measured (markers) [15, 58, 60, 61, 62, 96, 97]. Fitting performed exclusively on the data of Kondoh et al. [15, 62] (small dots).	50
6	Evolution of the normalised particle size of nickel in Ni-YSZ anodes predicted by Eq.38 (lines) and measured (markers) [19, 67, 75, 98].	51
7	Representation of the assumption for the calculation of the TPB blocked by the deposition of Cr_2O_3	52
8	Comparison between the local electrochemical behaviour simulated by the one-dimensional model and the REV model, with a dense or porous GDL, during IV characterisation of the SRU depicted in Figure 1a. CO: co-flow, COU: counter-flow configuration.	53
9	Evolution at locations A,B and C (Figure 1a), in co-flow and counter-flow, of the relative ASR and overpotential of the cathode and anode, during operation at the nominal point (Figure 8) at constant SRU potential. The approximate initial temperature and current density are indicated. Color online.	54
10	Profiles of the norm of the current density in the cathode and GDL (top), oxygen molar fraction (second), steam in the anode and GDL (third) and local overpotential at the electrode/electrolyte (fourth). The whole GDLs are not depicted for clarity. Conditions correspond to the fuel inlet in counter-flow (A in Figure 1a), after approximately 500 h of operation at the nominal point.	55
11	Comparison between relative degradation rates measured on short stacks [93] and those predicted by the one-dimensional model, without any calibration. Color online.	56
12	Initial ASR at an overpotential of 0.05 V, and influence of operating conditions on the degradation of the anode: relative increase in ASR, rate of the relative increase in ASR and time to reach $r_{g\text{Ni}\infty}$	57
13	(a): evolution of the number of active sites in the cathode. 1073 K, $x_{\text{O}_2}=0.21$, $j = 0.5 \text{ Acm}^{-2}$, computation of $\text{CrO}_2(\text{OH})_{2(\text{g})}$ at 973 K. (b): effect of the electrode thickness and assumptions for the calculation of $\text{CrO}_2(\text{OH})_{2(\text{g})}$ on the degradation of the cathode. Times indicate start of zirconate formation. One-dimensional model.	58
14	Effect of temperature and overpotential on the initial ASR and degradation of the cathode: relative increase in ASR, rate of the relative increase in ASR. Effect of the assumptions for the calculation of $x_{\text{CrO}_2(\text{OH})_{2(\text{g})}}$: gas channel (a) and gas inlet conditions (b). Simulated with the one-dimensional model, until the active sites at the cathode/electrolyte interface Γ_5 are blocked.	59
15	Initial ASR of the cathode, and relative increase in ASR and rate of the relative increase in ASR. Simulations of 3000 h with the one-dimensional model.	60
16	Effects of operating conditions on the ASR of the cathode at 1073 K and an assigned overpotential of 0.1 V (point depicted in Figure 15), after 3000 h or until the full blocking of the active sites at the cathode/electrolyte interface Γ_5 . One-dimensional model.	61
17	Operating conditions to avoid the formation of LZ0/SZO insulating phases in the LSM-YSZ cathode, predicted by the one-dimensional model (gray areas), and the REV model, with a dense or porous GDL (lines).The current density computed by the one-dimensional model, for air, is indicated.	62

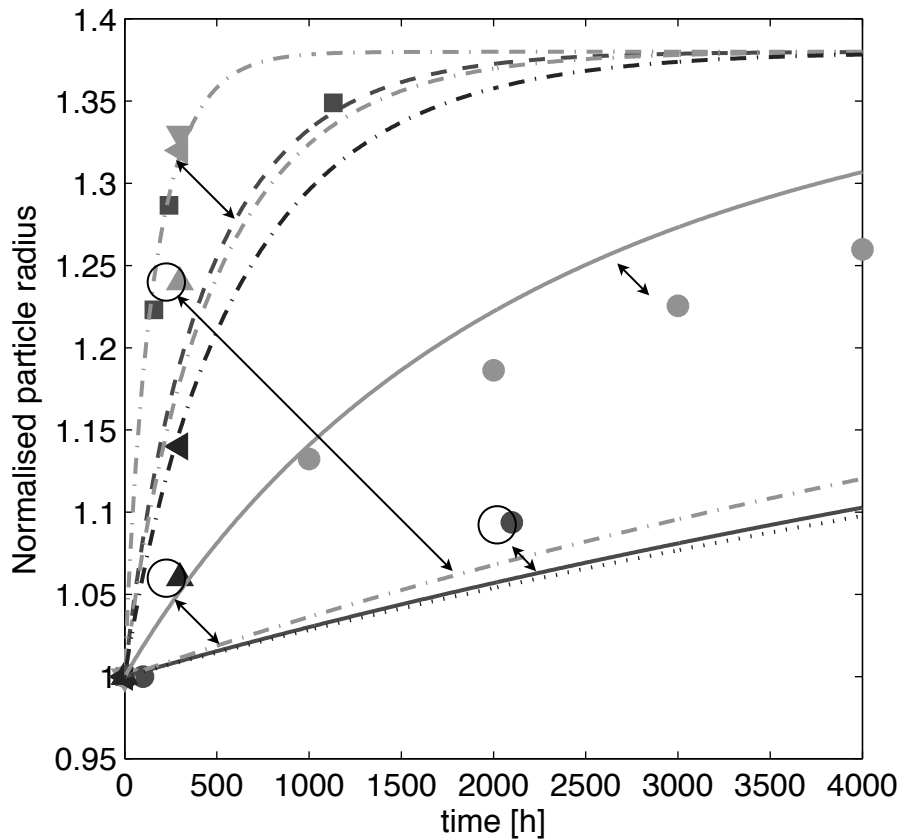




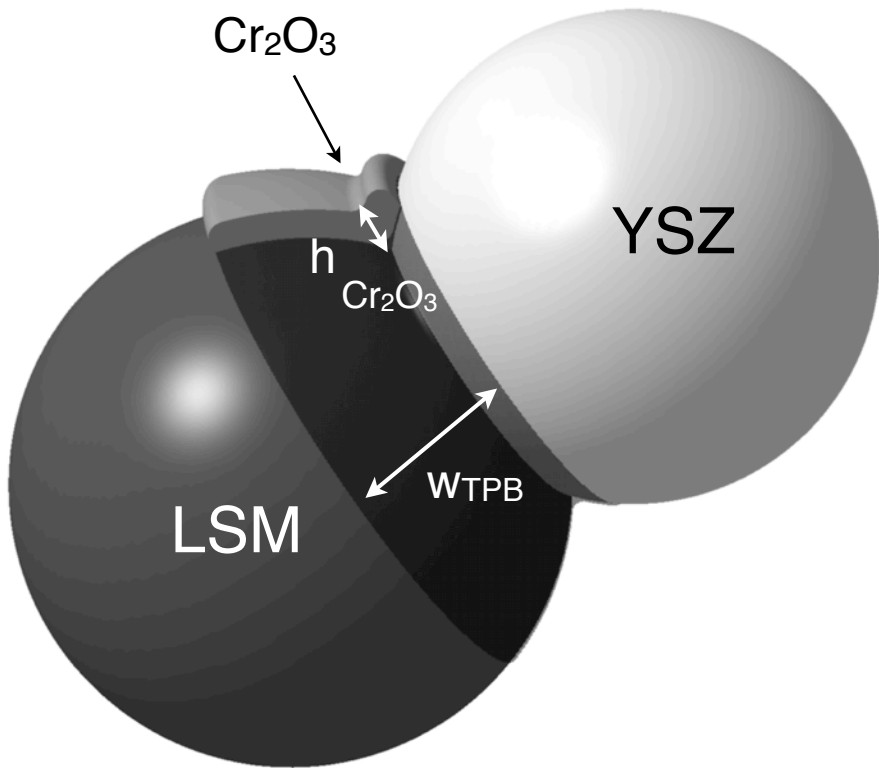


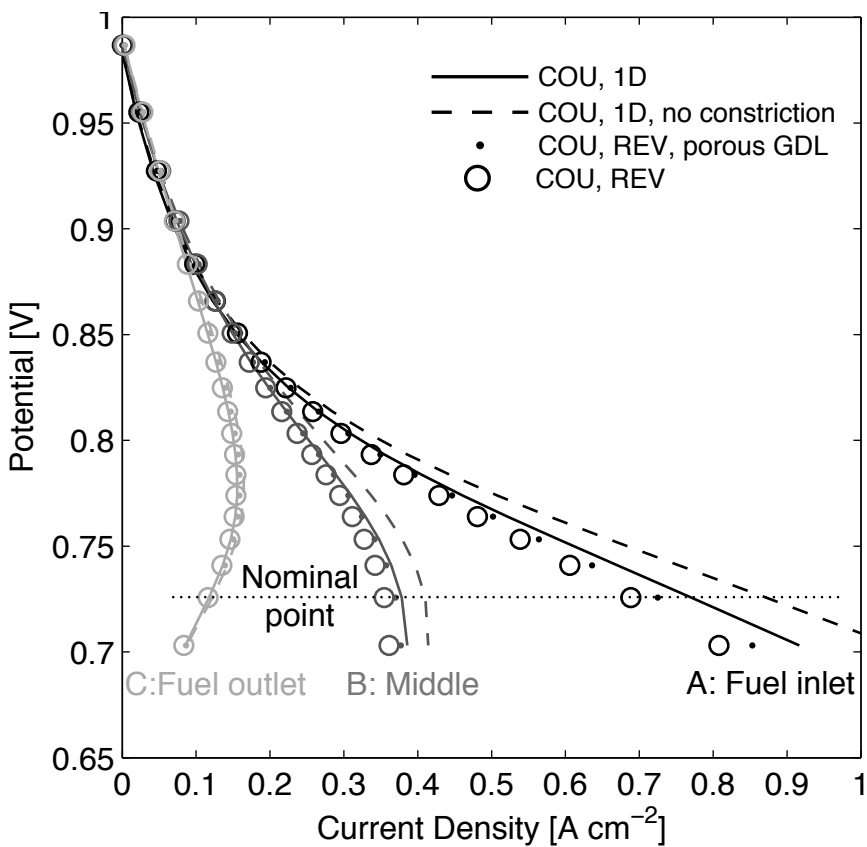
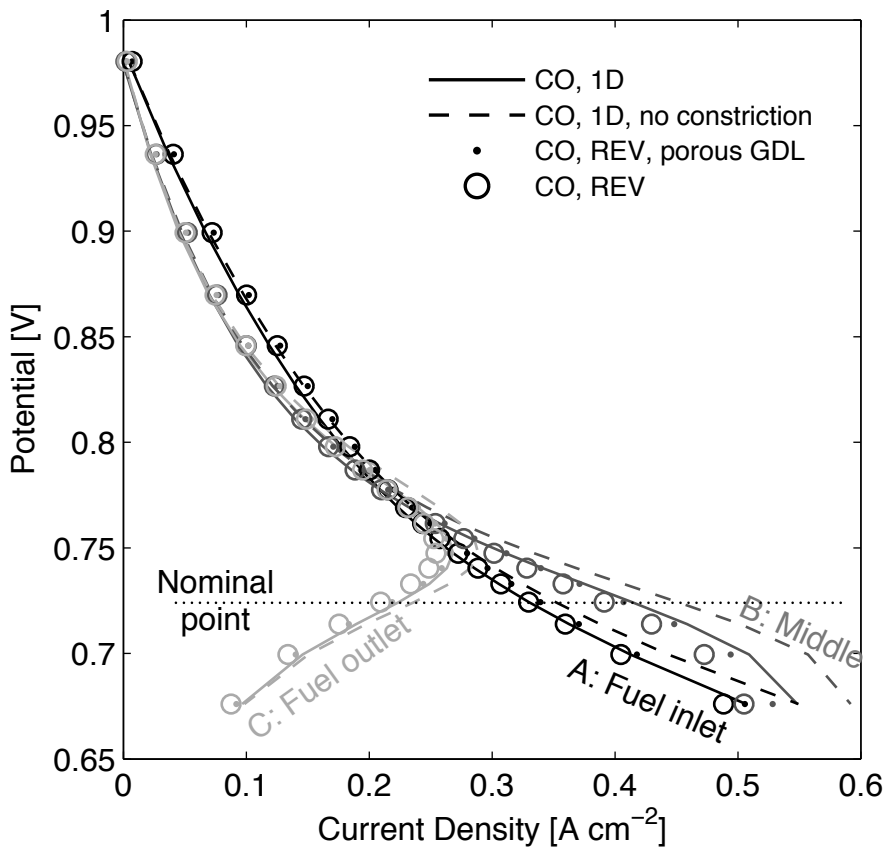


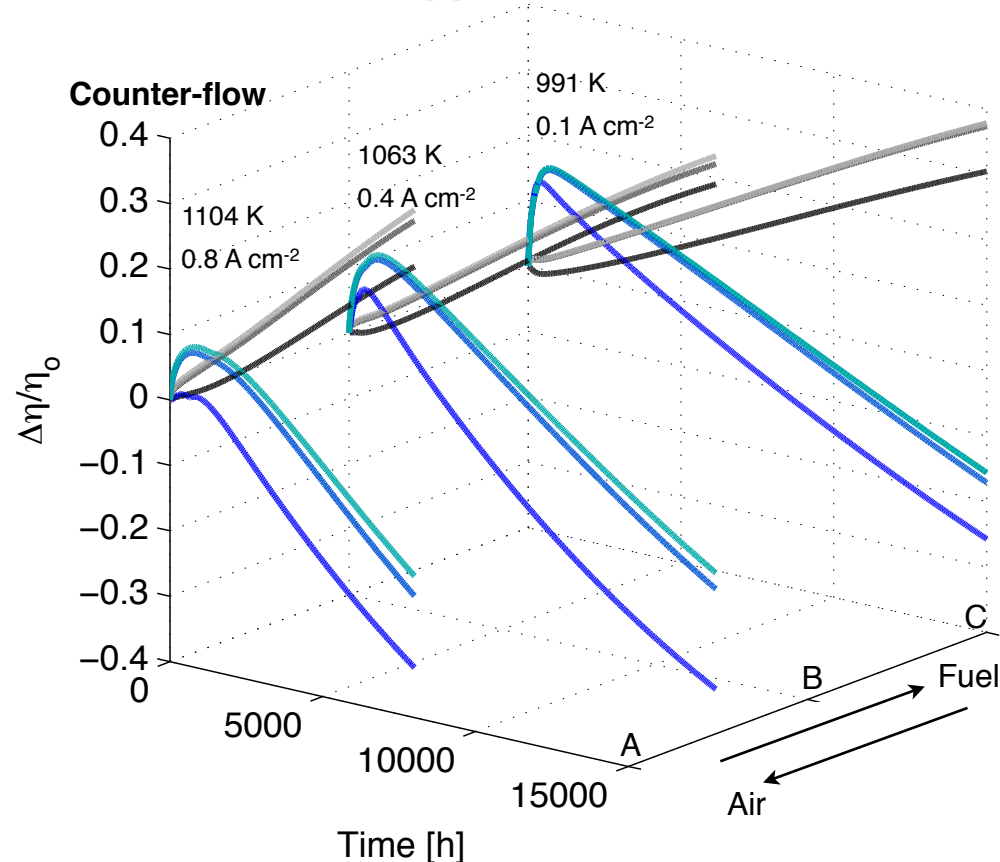
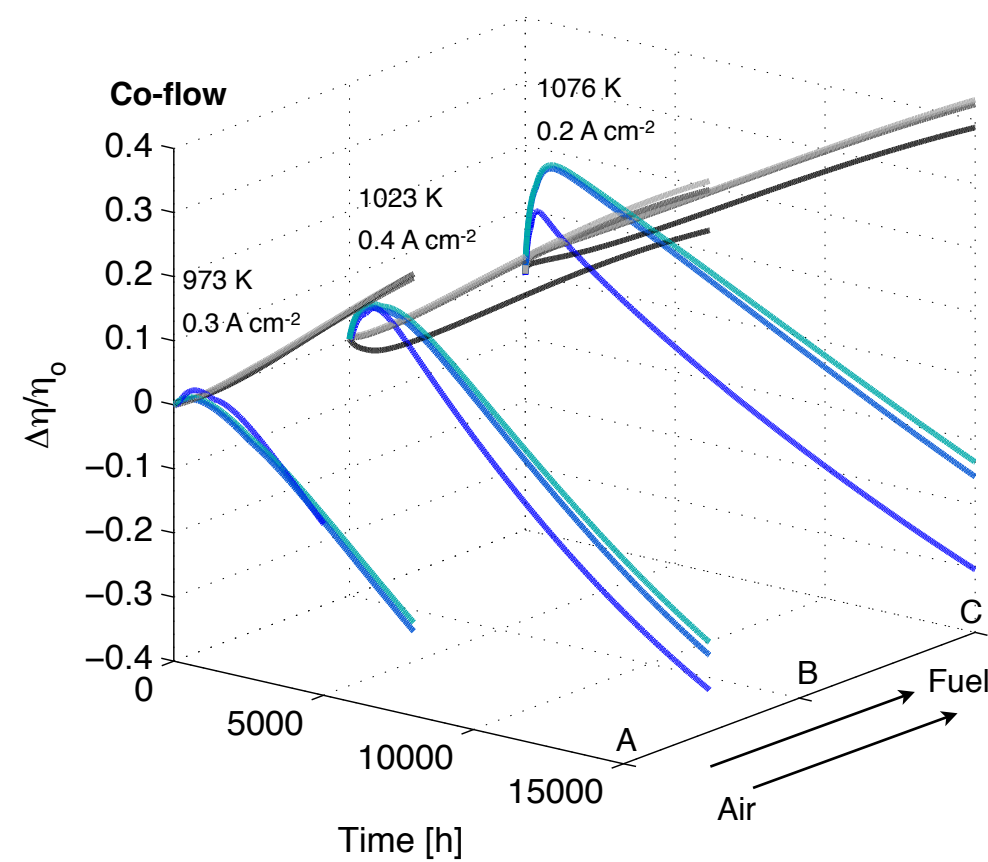
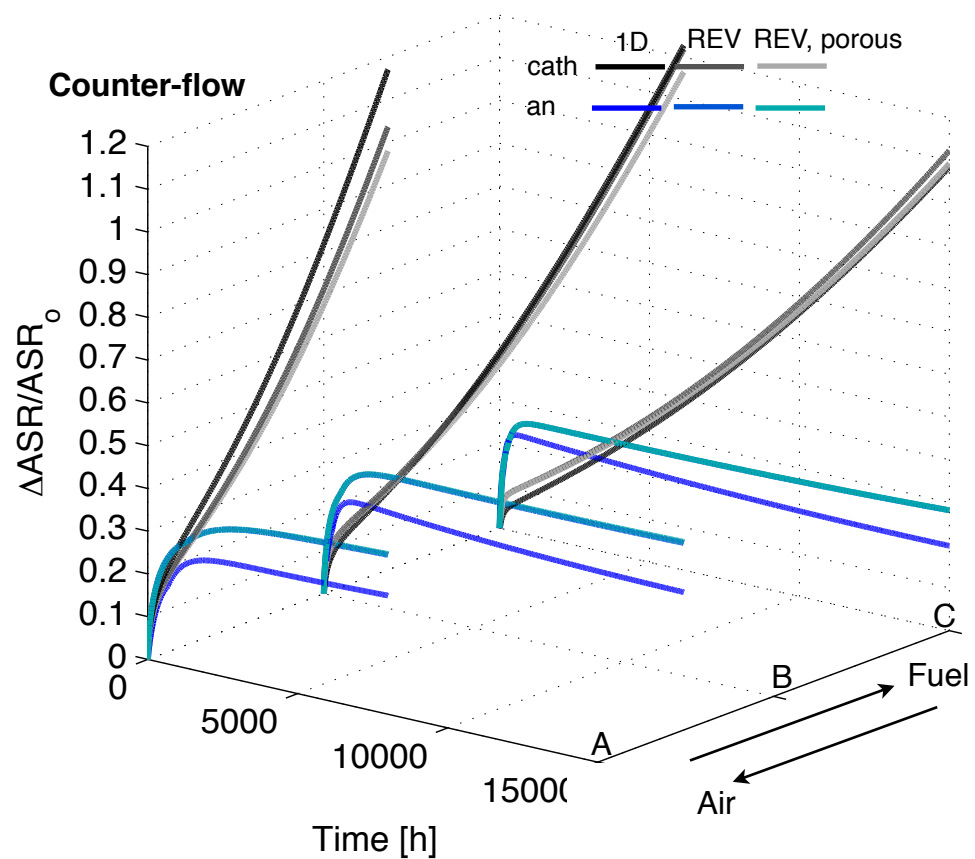
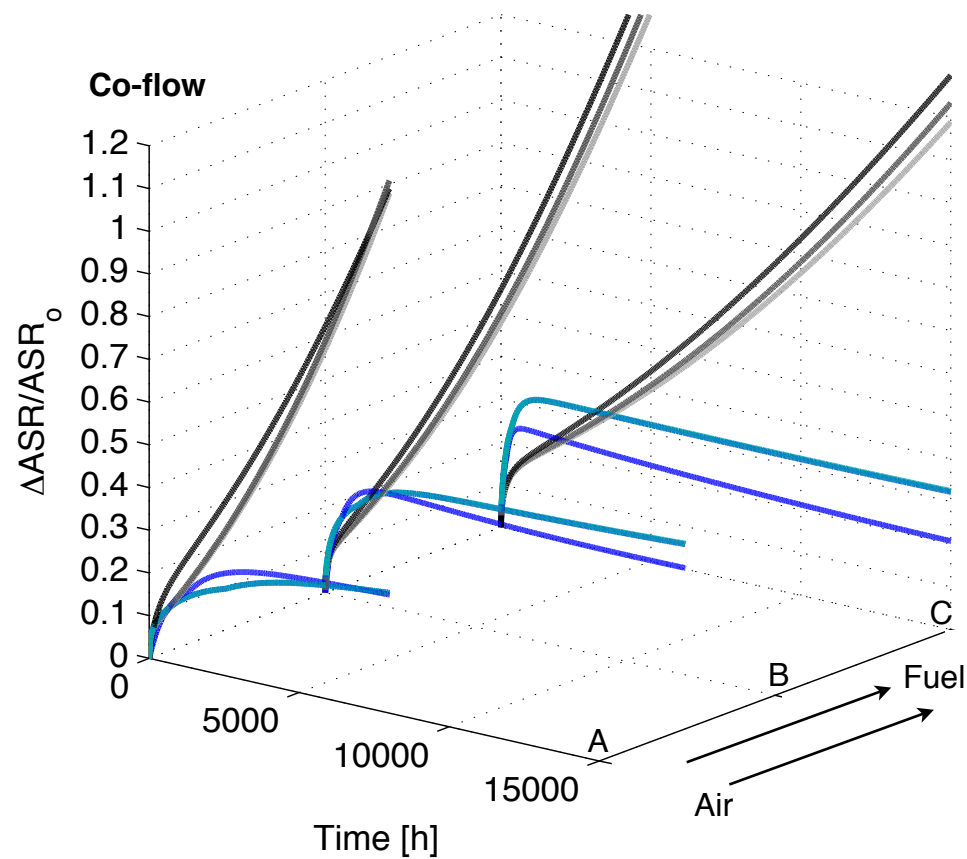


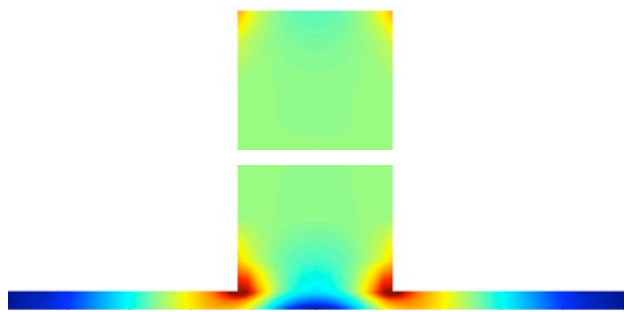
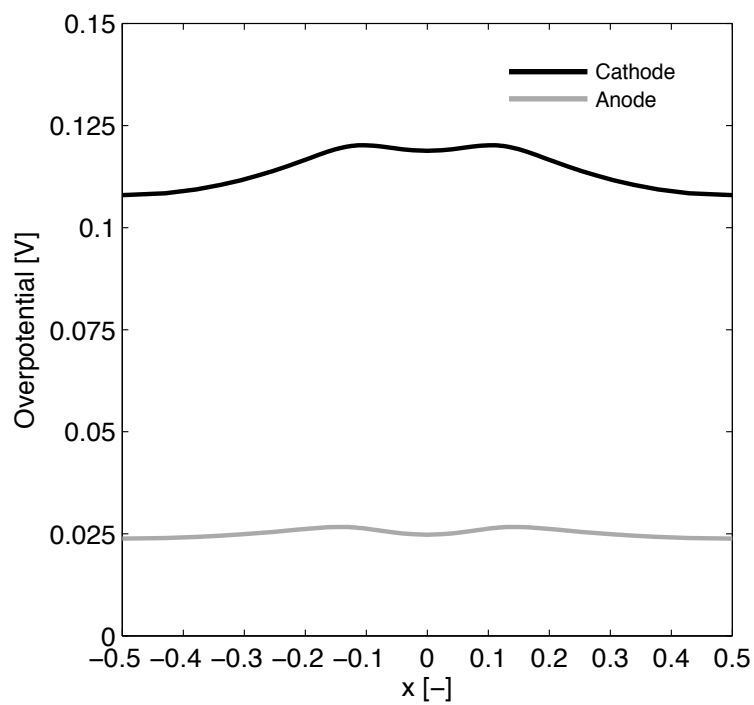
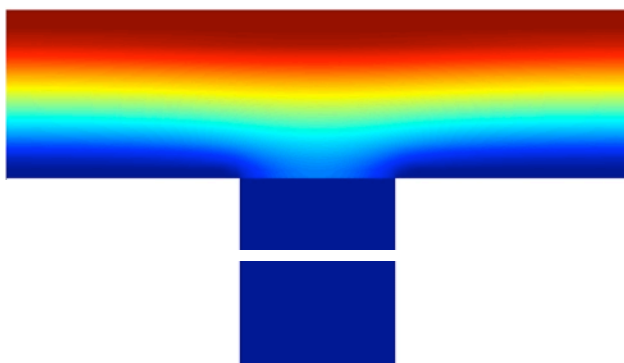
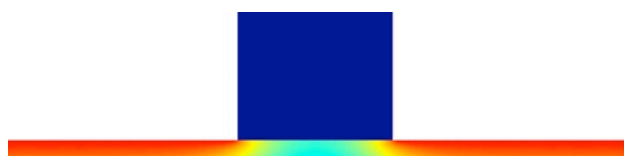
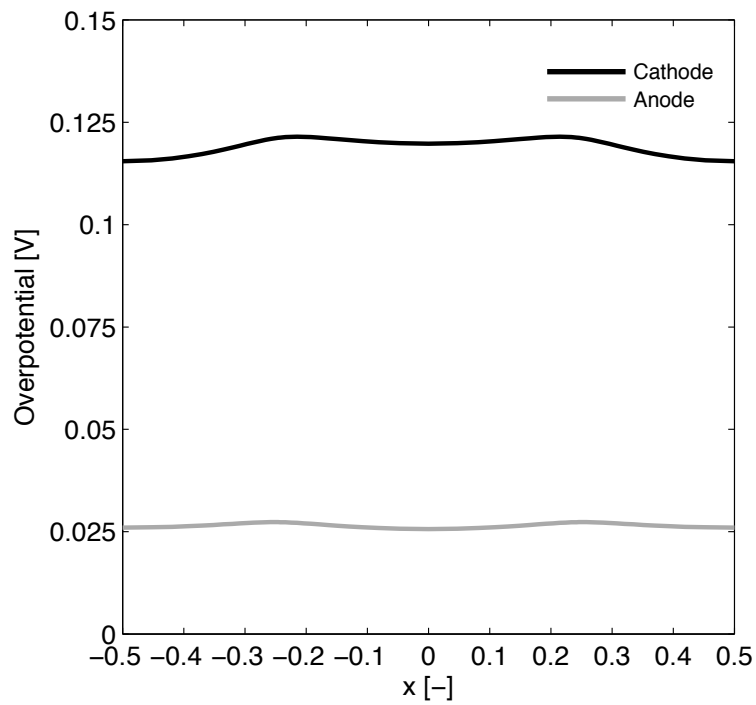
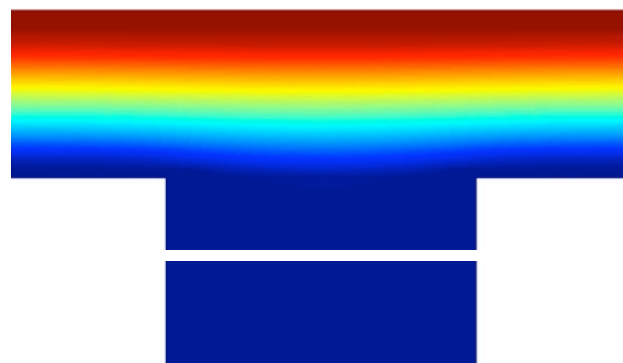
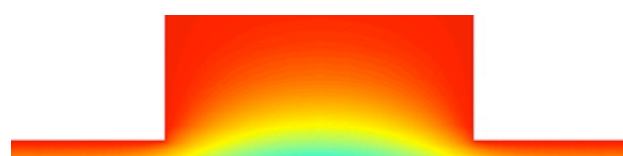
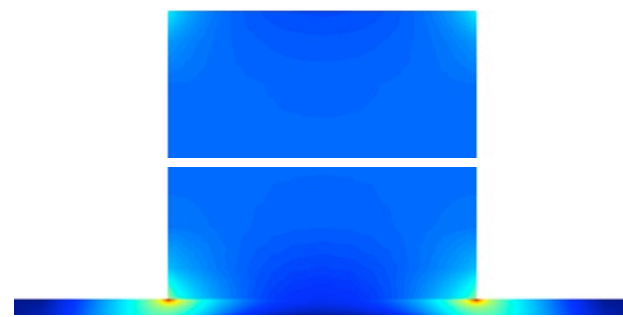
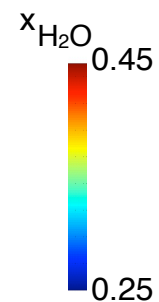
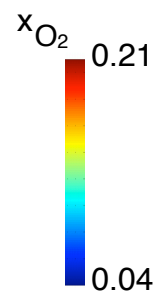
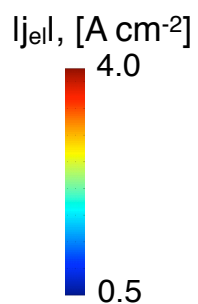


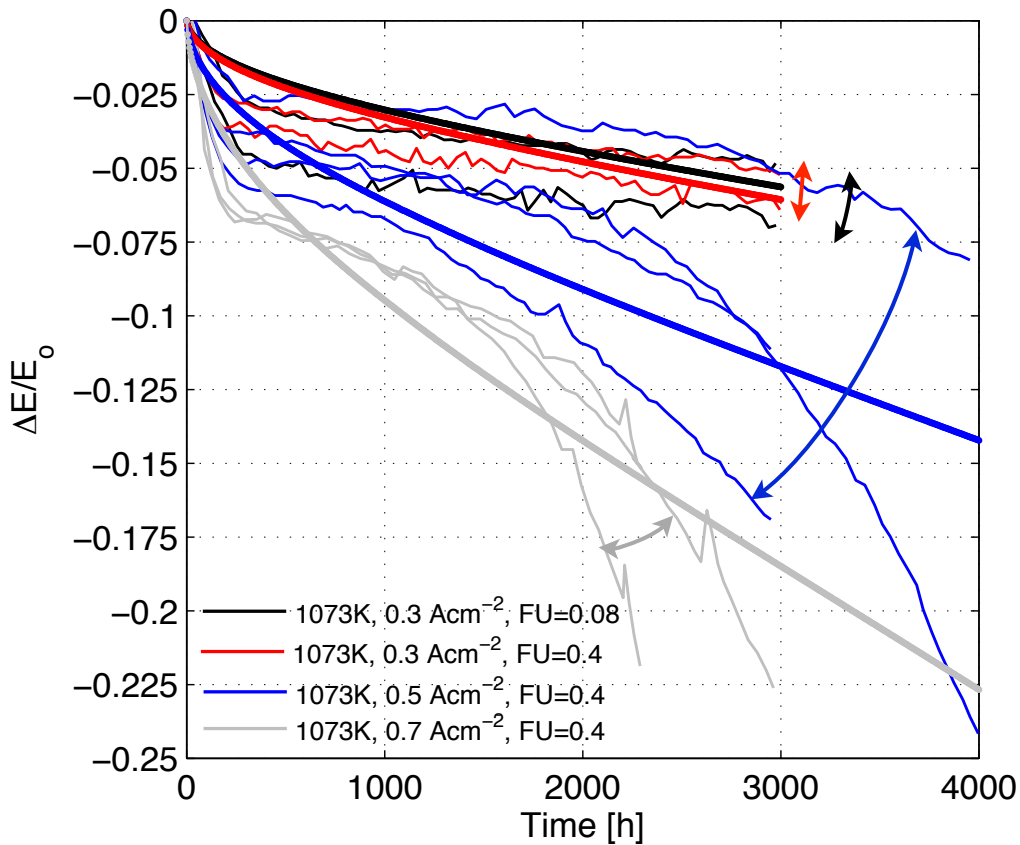
- | | | | |
|---|--|---|--|
| ■ | $x_{\text{H}_2\text{O}}/x_{\text{H}_2}=0.6/0.4$, 1073K [19] | ◄ | $x_{\text{H}_2\text{O}}/x_{\text{H}_2}=0.5/0.5$, 1273K [77] |
| ● | $x_{\text{H}_2\text{O}}/x_{\text{H}_2}=0.03/0.97$, 1073K [78] | ▼ | $x_{\text{H}_2\text{O}}/x_{\text{H}_2}=0.85/0.15$, 1273K [77] |
| ● | $x_{\text{H}_2\text{O}}/x_{\text{H}_2}=0.04/0.04$, 1273K [69] | ▲ | $x_{\text{H}_2\text{O}}/x_{\text{H}_2}=0.03/0.97$, 1023K [77] |
| ▲ | $x_{\text{H}_2\text{O}}/x_{\text{H}_2}=0.03/0.97$, 1273K [77] | ◄ | $x_{\text{H}_2\text{O}}/x_{\text{H}_2}=0.5/0.5$, 1023K [77] |

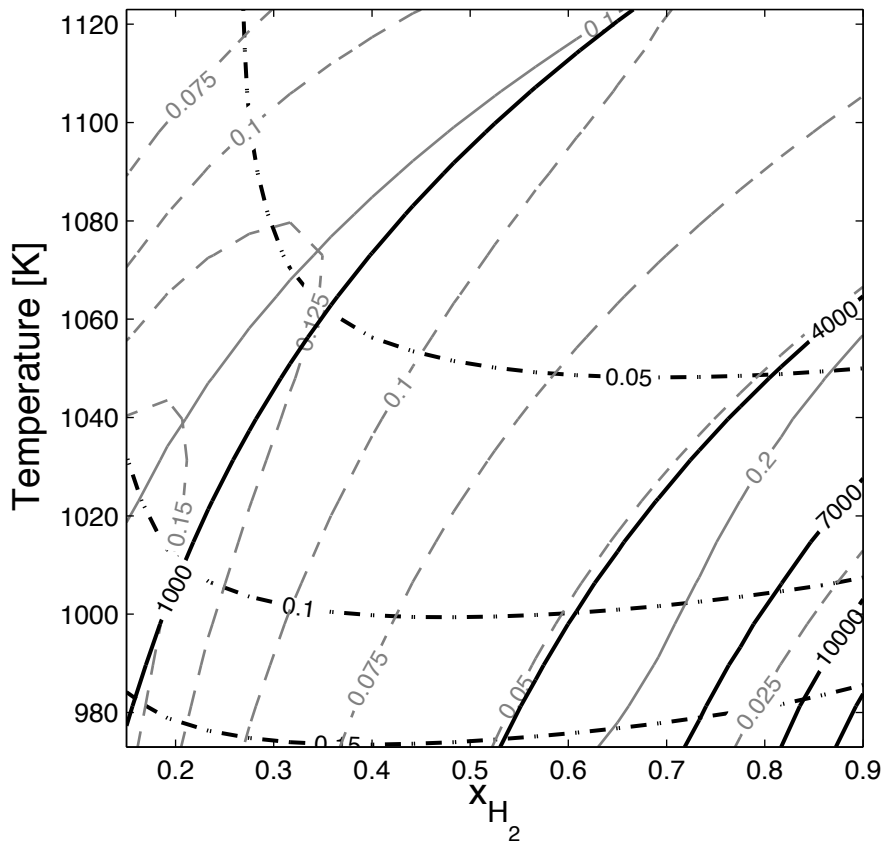








Dense GDL**Cathode****Anode****Porous GDL**



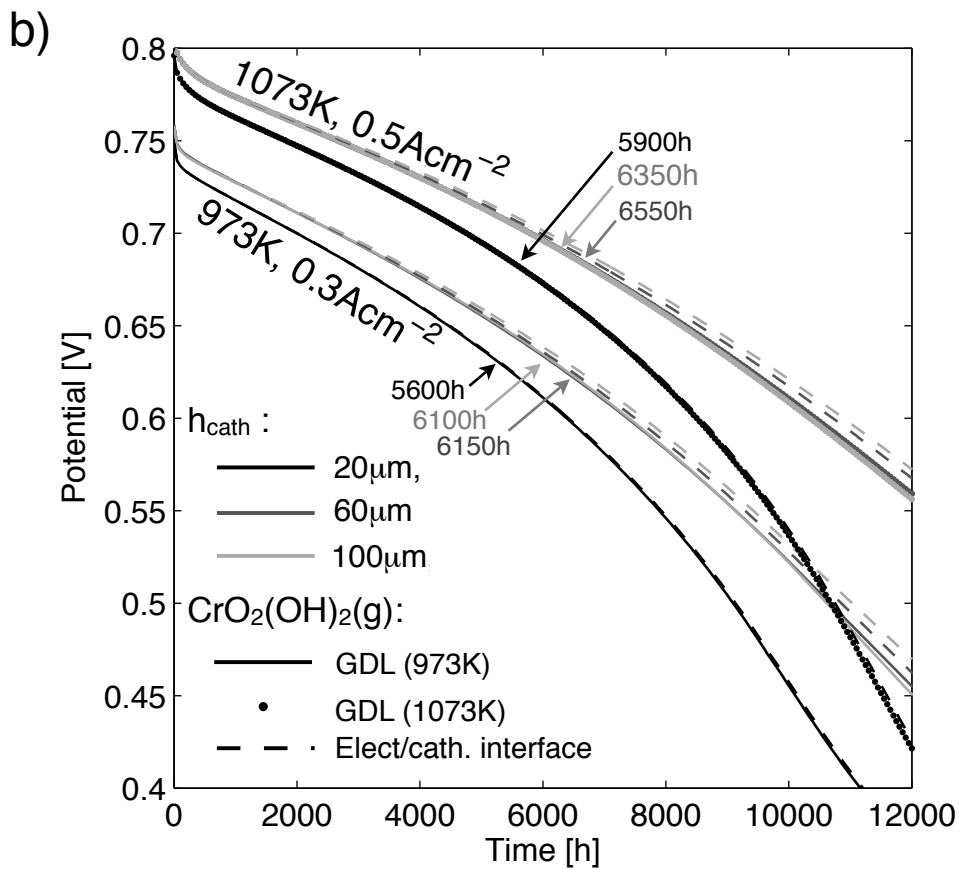
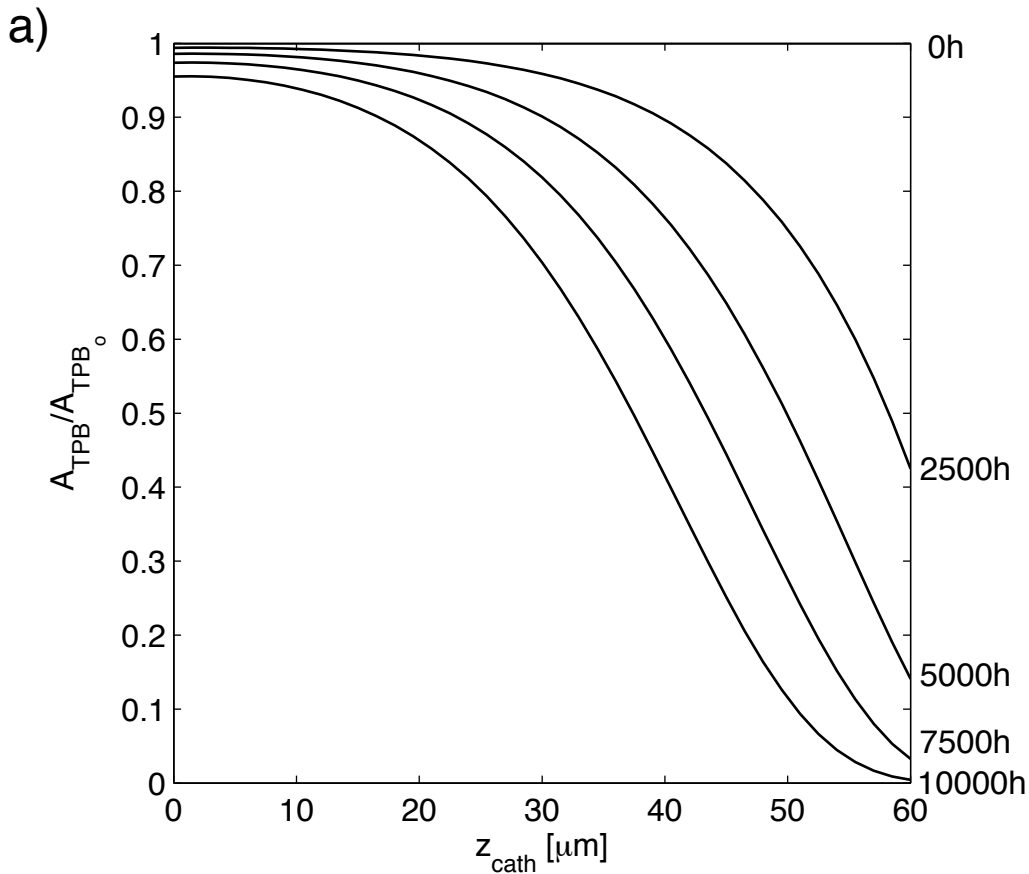


 ASR_0 [$\Omega \text{ cm}^2$]

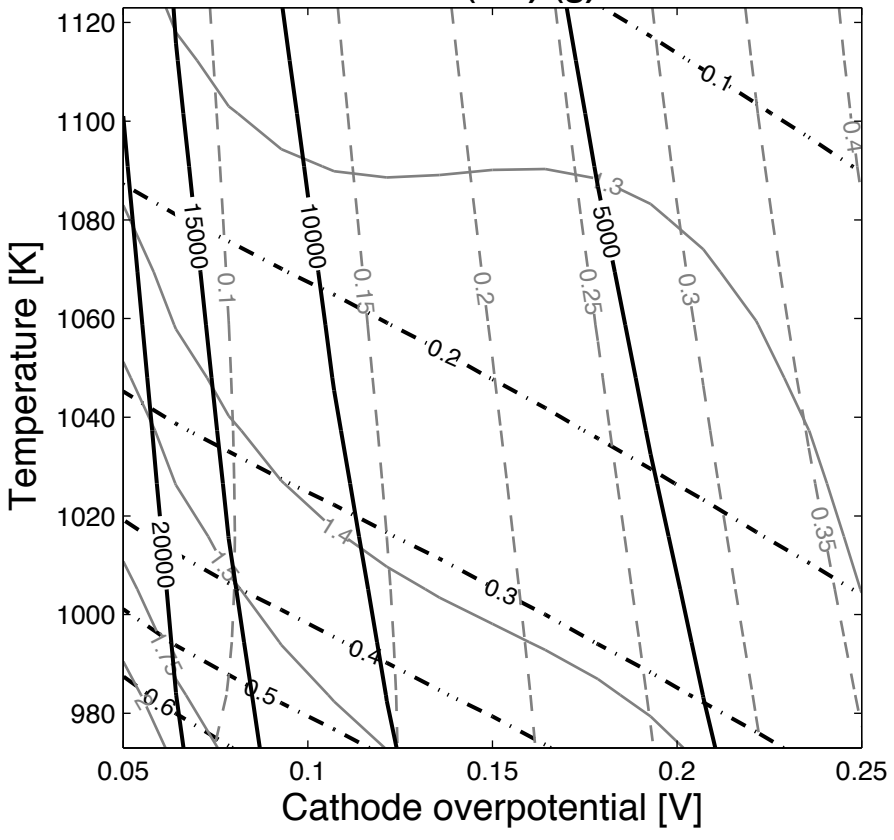
 $\Delta ASR ASR_0^{-1}$

 $\Delta ASR ASR_0^{-1} t^{-1}$ [1000 h^{-1}]

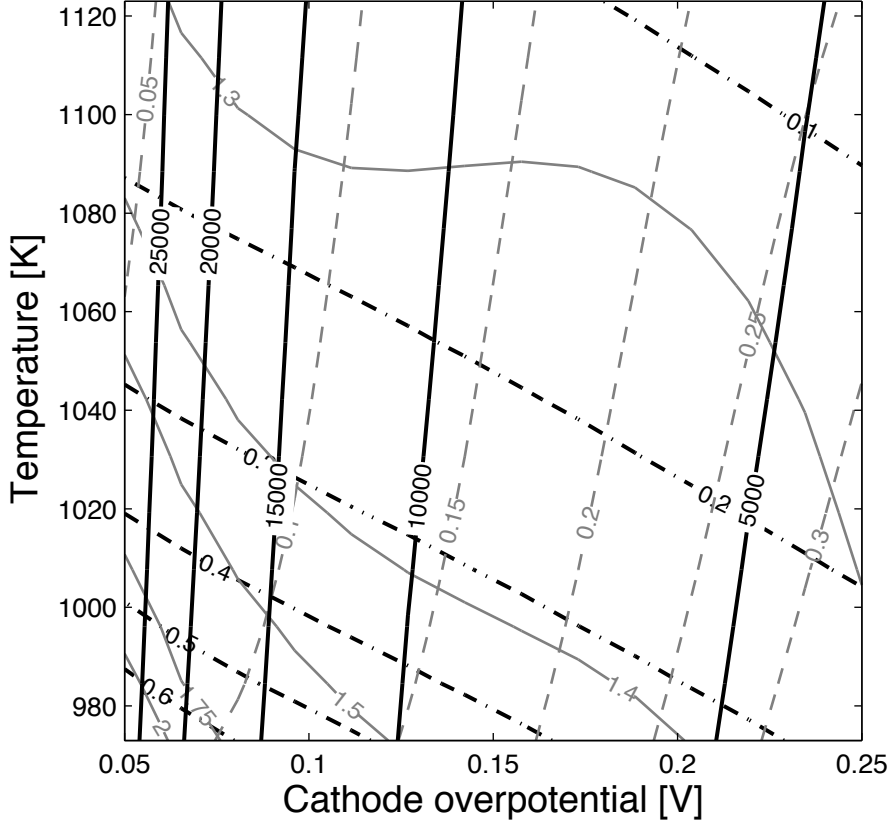
 t_∞ [h]





a) **Uncoated MIC: $\text{CrO}_2(\text{OH})_2(\text{g})$: GDL**



b) **Coated MIC: $\text{CrO}_2(\text{OH})_2(\text{g})$: Inlet (973K)**



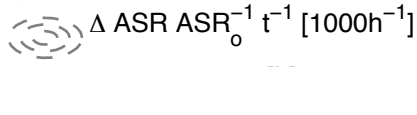
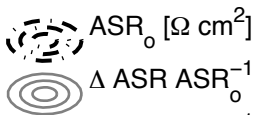
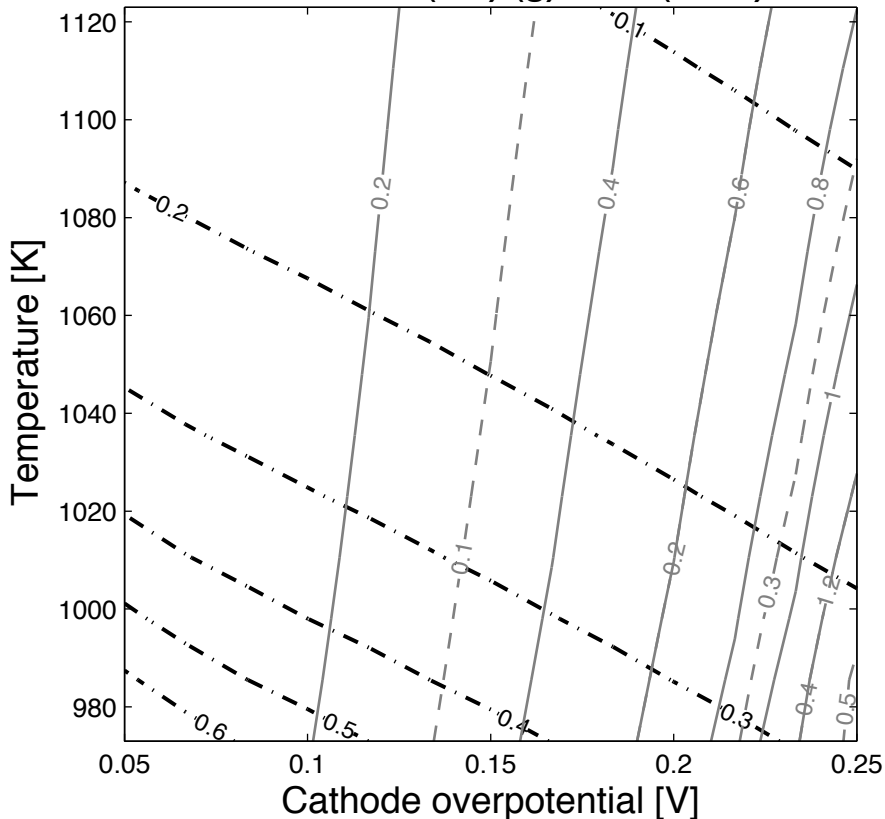
 ASR_0 [$\Omega \text{ cm}^2$]

 $\Delta \text{ASR ASR}_0^{-1}$

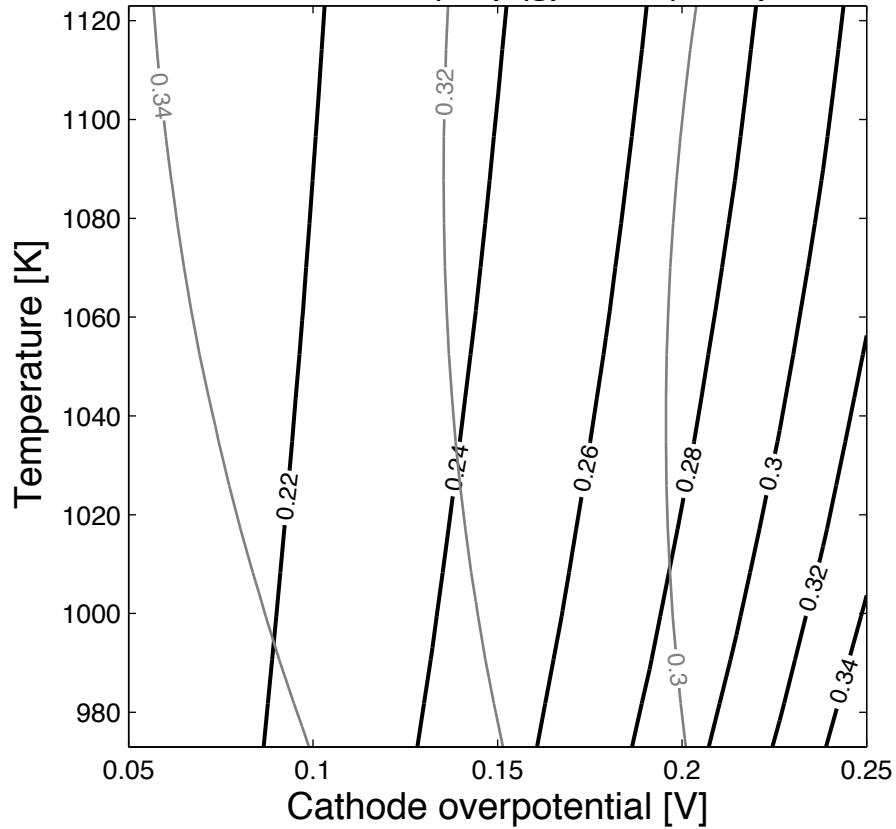
 $\Delta \text{ASR ASR}_0^{-1} \text{ t}^{-1}$ [1000h^{-1}]


 $t_{\text{Blocked interface}}$ [h]


Coated MIC: $\text{CrO}_2(\text{OH})_2(\text{g})$: Inlet (973K)



Coated MIC: $\text{CrO}_2(\text{OH})_2(\text{g})$: Inlet (973K)



 ASR (1073K, $\eta=0.1\text{V}$), 3000h [$\Omega \text{ cm}^2$]

 ASR (1073K, $\eta=0.1\text{V}$), blocked interface [$\Omega \text{ cm}^2$]

